

The *Suzaku* Technical Description

Version: October, 2010

Announcement of Opportunity #6

Institute of Space and Astronautical Science (ISAS/JAXA)
and the
X-ray Astrophysics Laboratory
NASA/Goddard Space Flight Center

Copies of this guide are available in `html`, `postscript` and `pdf` formats.

Contents

1	Introduction	2
2	Changes Since AO-5	5
3	Mission Description	8
3.1	Brief Introduction to <i>Suzaku</i>	8
3.2	Operational Constraints	12
3.2.1	Telemetry Rates	12
3.2.2	Summary	13
3.3	Calibration	14
4	Observation Policies	16
4.1	Data Rights	17
4.2	Target of Opportunity Proposals	18
4.3	Pointing Constraints	19
4.4	Events After Submission	20
5	Writing A Successful <i>Suzaku</i> Proposal	23
5.1	First Checks	23
5.1.1	Viewing	23
5.1.2	Previous Observations	23
5.2	Proposal Ingredients	24
5.3	PIMMS & WebPIMMS	24
5.4	XSPEC Simulations	25

5.4.1	WebSPEC Simulations	25
5.5	Examples	26
5.5.1	Faint Oxygen Emission from the Local Hot Bubble	26
5.5.2	Hard Tails of XRBs	27
5.6	XISSIM	40
5.7	MAKI	41
5.8	RPS	41
5.9	Checklist	42
5.10	Additional Requirements for US Proposers	43
6	X-Ray Telescopes (XRT)	44
6.1	Basic XRT Components	44
6.1.1	Reflectors	46
6.1.2	Pre-Collimator	47
6.1.3	Thermal Shields	48
6.2	In-Flight Performance	49
6.2.1	Focal Positions	49
6.2.2	Optical Axis	49
6.2.3	Effective Area	51
6.2.4	Vignetting	54
6.2.5	Angular Resolution	55
6.2.6	Stray Light	55
7	X-Ray Imaging Spectrometer (XIS)	64
7.1	XIS Overview	64
7.2	CCD Pixels & Coordinates	68
7.3	Pulse Height Determination & Hot Pixel Rejection	68
7.4	On-Board Event Analysis	69
7.5	Data Processing Modes	70
7.5.1	Clock Modes	70
7.5.2	Window & Burst Options	71
7.5.3	Editing Modes	72

7.5.4	Discriminators	77
7.6	Spaced-Row Charge Injection	78
7.6.1	Principle	78
7.6.2	Supported Modes	78
7.6.3	Data Impact	78
7.7	Low Energy Efficiency Degradation	80
7.8	Non-X-Ray Background	83
7.9	XIS Observations	86
7.9.1	Photon Pile-Up	86
7.9.2	Out-Of-Time Events	89
7.9.3	Day Earth Contamination	89
7.9.4	Telemetry Limit	89
7.10	Clock/Editing Mode Selection	91
7.11	In-Flight XIS Calibration	93
7.11.1	Charge Transfer Efficiency & Energy Scale	93
7.11.2	Energy Resolution & Pulse Height Distribution Function (Full Win- dow)	95
7.11.3	Energy Resolution & Pulse Height Distribution Function (Other) . .	99
7.11.4	Quantum Efficiency	100
7.12	Putative Micro-Meteorite Hits	101
7.13	XIS References	104
8	Hard X-Ray Detector (HXD)	105
8.1	GSO/BGO Counter Units	107
8.2	PIN-Si Diodes	107
8.3	HXD Field of View	108
8.4	In-Orbit HXD Background	108
8.5	Background Modeling	111
8.5.1	PIN Background Model	112
8.5.2	GSO Background Model	114
8.5.3	Theoretical Sensitivity	114
8.6	Data Analysis Procedure	115

<i>Technical Description</i>	v
8.7 Wide-Band All-Sky Monitor (WAM)	115
A Acronyms	119
B Important Web/E-Mail Addresses	123

List of Figures

3.1	The 96 minute <i>Suzaku</i> orbit.	9
3.2	[Left] Schematic picture of the bottom of the <i>Suzaku</i> satellite. [Right] A side view of the instrument and telescopes on <i>Suzaku</i>	9
3.3	XIS effective area of one XRT + XIS system, for both the FI and BI chips.(No contamination included.)	10
3.4	The Encircled Energy Function (EEF) showing the fractional energy within a given radius for one quadrant of the XRT-I telescopes on <i>Suzaku</i> at 4.5 and 8.0 keV.	12
3.5	Total effective area of the HXD detectors, PIN and GSO, as a function of energy.	13
5.1	Simulation of an HXD observation of a 10 mCrab source with a Crab-like spectrum. Here, the cornorm of the two background files has been set to 0.	37
5.2	Simulation with the highest estimated background, for both the PIN and the GSO.	38
5.3	Simulation with the lowest estimated background, for both the PIN and the GSO.	40
6.1	Layout of the XRTs on the <i>Suzaku</i> spacecraft.	45
6.2	A <i>Suzaku</i> X-ray telescope.	46
6.3	A thermal shield.	48
6.4	Focal positions on the XISs when the satellite points at MCG–6-30-15 using the XIS aimpoint.	49

6.5	Locations of the optical axis of each XRT-I module in the focal plane determined from the observations of the Crab nebula in 2005 August–September. This figure implies that the image on each XIS detector becomes brightest when a target star is placed at the position of the corresponding cross. The dotted circles are drawn every $30''$ in radius from the XIS-default position (see text).	50
6.6	The source- and background-integration regions overlaid on the Crab images taken with XIS1 at the XIS-default position (left) and the HXD-default position (right) on 2005 September 15–16. The images are elongated in the frame-transfer direction due to the out-of-time events (see text). In order to cancel these events, the background regions with a size of 126 by 1024 pixels each are taken at the left and right ends of the chip for the XIS-default position, and a single region with a size of 252 by 1024 pixels is taken at the side far from the Crab image for the HXD-default position. The remaining source-integration region has a size of 768 by 1024 pixels, or $13'3 \times 17'8$. The background subtraction is carried out after area-size correction.	51
6.7	Power-law fit to the Crab spectra of all four XIS modules taken at the XIS-default position. All the parameters are allowed to vary independently for each XIS module. The fit is carried out in the 1.0–10.0 keV band, excluding the 1.5–2.0 keV interval where large systematic uncertainties associated with the Si K-edge remain. This energy range is retrieved after the fit.	53
6.8	Count rates of the Crab pointings offset in DETX (left) and DETY (right) in the 2–10 keV band. Red and green symbols correspond to the data during 2005 and 2006, respectively. The solid line corresponds to the output of the ray-tracing simulator <code>xissim</code> . The bottom panels show the ratios of the data to the simulator output.	57
6.9	The same as Fig.6.8 but in the 3–6 keV band.	58
6.10	The same as Fig.6.8 but in the 8–10 keV band.	59
6.11	Images of the four XRT-I modules in the focal plane: SS Cyg (left) and simulation (right). All the images are binned to 2×2 pixels and then smoothed with a Gaussian with a sigma of 3 pixels, where the pixel size is $24 \mu\text{m}$. The Fe55 events were removed from the SS Cyg image.	60
6.12	PSF of the four XRT-I images. The lower panels show the ratio between the observed and simulated data.	61
6.13	EEF of the four XRT-I images. The EEF is normalized to unity at the edge of the CCD chip (a square of $17'8$ on the side). The lower panels show the ratio between the observed and simulated data.	62

6.14	Focal plane images formed by stray light. The left and middle panels show simulated images of a monochromatic point-like source of 4.51 keV located at $(-20', 0')$ in (DETX, DETY) for the cases of without and with the pre-collimator, respectively. The radial dark lanes are the shades of the alignment bars. The right panel is the in-flight stray image of the Crab nebula in the 2.5–5.5 keV energy band located at the same off-axis angle. The unit of the color scale of this panel is counts per 16 pixels over the entire exposure time of 8428.8 s. The count rate from the whole image is 0.78 ± 0.01 counts s^{-1} including background. Note that the intensity of the Crab nebula measured with XIS3 at the XIS-default position is 458 ± 3 counts s^{-1} in the same 2.5–5.5 keV band. All the images are binned to 2×2 pixels and then smoothed with a Gaussian with a sigma of 2 pixels, where the pixel size is $24 \mu\text{m}$	63
6.15	Angular responses of the XRT-I at 1.5 (left) and 4.5 keV (right) up to 2° . The effective area is normalized to 1 at the on-axis position. The integration area is corresponding to the detector size of the XISs ($17'8 \times 17'8$). The four solid lines in the plots correspond to different detector IDs. The crosses are the normalized effective area using the Crab pointings.	63
7.1	Photo of an XIS sensor	65
7.2	Schematic view of the XIS system	66
7.3	Time sequence of the data readout.	73
7.4	Information sent to the telemetry is shown for 5×5 , 3×3 , and 2×2 modes.	76
7.5	Definition of the grades in the P-Sum/Timing mode.	76
7.6	Frame mode data with the Spaced-row Charge Injection (SCI).	79
7.7	An empirical model for the on-axis contamination evolution.	81
7.8	Temporal evolution of the radial profile of the contamination thickness.	82
7.9	Spectrum of the Non-X-ray-background (NXB)	83
7.10	ACTY dependence of the NXB.	84
7.11	Cut-off rigidity dependence of the NXB.	85
7.12	Incident vs observed count rates of a point source for the FI sensor.	87
7.13	Time history of the central energy of Mn $K\alpha$ line without the CTE correction	94
7.14	Time history of the CTE-corrected central energy of the Mn $K\alpha$ line.	95
7.15	Time history of the energy resolution of the Mn $K\alpha$ line after the CTE correction.	96

7.16	Time history of the center energy and width of the O VIII $K\alpha$ line after the CTE correction.	97
7.17	Gain uncertainty of 1/4 window option.	99
7.18	^{55}Fe source spectrum for a 2.0 s burst mode observation	100
7.19	Time history of the P-sum mode gain.	101
7.20	Time history of the P-sum mode energy resolution.	102
7.21	Relative flux normalization between different sensors.	103
8.1	The Hard X-ray Detector before installation.	105
8.2	Schematic picture of the HXD instrument, which consists of two types of detectors: the PIN diodes located in the front of the GSO scintillator, and the scintillator itself.	106
8.3	Angular response of a single fine-collimator along the satellite X-axis, obtained from offset observations of the Crab nebula.	109
8.4	[Left] Comparison of average non X-ray background spectra of the PIN, obtained in various epochs. The Crab spectrum, scaled down by two orders of magnitude, is shown as well. [Right] Evolution of average GSO-NXB spectra.	109
8.5	Comparison of the in-orbit detector background of the PIN/GSO as of AO-6, normalized by the individual effective areas, with that of the <i>RXTE</i> -PCA, <i>RXTE</i> -HEXTE, and <i>BeppoSAX</i> -PDS. Dotted lines indicate 1 Crab, 100 mCrab, and 10 mCrab intensities.	110
8.6	[Left] Light curve of the non X-ray background of the PIN, folded with the elapsed time after the SAA passage (<i>top</i>), and the average cut-off rigidity at the corresponding position (<i>bottom</i>). [Right] The same folded light curves for the GSO background, in the 40–90, 260–440, and 440–700 keV energy bands.	111
8.7	Comparison between the data and the NXB model count rate of sky observations with 10 ks integration time in the 15–40 keV band. Observations with no apparent hard X-ray objects in the XIS FOV were selected (see text for details of the data selection).	112
8.8	The same as Figure 8.7, but for observations of E0102-72 (black) and the Cygnus LOOP (red).	113

8.9	Comparison between the measured PIN spectra (black) and the PIN NXB model spectra (red) for observations of objects with no strong hard X-ray contribution. Their fractional residuals are given by purple crosses in the bottom panel of each figure. The blue and green histograms in the top panel indicate the background-subtracted spectrum and the typical CXB spectrum (Boldt 1987), respectively.	116
8.10	Comparison of the GSO spectra between the data (black) and BGD model (red) for observations of objects with no known strong hard X-rays. Their fractional residuals are given by blue crosses.	117
8.11	Calculated detection limits of the HXD, for continuum measurements. The solid lines denote the statistical 3σ limit for a 100 ks exposure, while the dashed lines show the assumed systematic uncertainties of 3% and 1.5% for the PIN- and GSO-NXB modeling, respectively.	118

List of Tables

3.1	Overview of <i>Suzaku</i> capabilities.	11
3.2	Error Budgets of Scientific Instrument Calibrations.	15
4.1	<i>Suzaku</i> time allocated to each group of observers. The ESA time is in parentheses as it is part of the Japanese allotment.	17
6.1	Telescope dimensions and parameters of XRT-I.	45
6.2	Design parameters for the pre-collimator.	48
6.3	Best-fit parameters of the power law model fits to the Crab spectra taken on 2005 September 15–16.	52
6.4	Best-fit parameters of the contemporaneous power-law fits to the Crab spectra taken in 2005 September 15–16.	54
7.1	Effective area and exposure time for different Burst and Window options. .	71
7.2	Supported clock mode and option with the SCI.	79
7.3	Major XIS Background Emission Lines (Tawa et al. 2008).	86
7.4	Total count rate which causes the indicated fraction of pile-up at the annulus of the PSF.	88
7.5	Telemetry allocation (kbit/s).	90
7.6	Typical event size after compression [byte].	90
7.7	Maximum counting rates for avoiding telemetry saturation [counts/s/XIS].	91
7.8	Maximum counting rate for avoiding pile-up.	92
7.9	Relative flux normalization between different sensors.	101

Chapter 1

Introduction

Suzaku is the fifth in the series of Japanese astronomy satellites devoted to observations of celestial X-ray sources, following the highly successful *Hakucho*, *Tenma*, *Ginga* and *ASCA* satellites. Like *ASCA*, *Suzaku* is a joint Japanese-US mission, developed by the Institute of Space and Astronautical Science (part of the Japan Aerospace Exploration Agency, ISAS/JAXA) in collaboration with the National Aeronautics and Space Administration's Goddard Space Flight Center (NASA/GSFC) and many other institutions. *Suzaku* was launched on a Japanese M-V rocket on July 10, 2005 from the JAXA Uchinoura Space Center (USC). Despite initial success, on August 8, 2005 a thermal short between the helium and neon tanks resulted in the liquid helium coolant venting to space, leaving the X-Ray Spectrometer (XRS) inoperable. However, the X-ray Imaging Spectrometer (XIS) and Hard X-ray Detector (HXD) are all working well. As a result, *Suzaku* retains its excellent X-ray sensitivity, with high throughput over a broad-band energy range of 0.2 to 600 keV. *Suzaku*'s broad bandpass, low background, and good CCD resolution makes it a unique tool capable of addressing a variety of outstanding problems in astrophysics.

Guest observing time on *Suzaku* will be awarded on a competitive basis and proposals will be judged on their scientific merits and their relevance to *Suzaku* observing capabilities. The overall purpose of this document is to aid potential users of *Suzaku* in proposing for time during the Guest Observer (GO) phase of the mission. In particular, upon reading this document, the proposer should be able to determine whether or not *Suzaku* is best suited to conduct the investigation in question. This should be demonstrated in the proposal, preferably using simulations of the proposed observations. All proposals should clearly answer the following four questions:

1. Is *Suzaku* capable of the proposed observation?
2. Is it the best available instrument for the investigation?
3. When can *Suzaku* observe a given source?

4. How much exposure time is required to meet the scientific goals?

Chapter 2 lists the principal changes since the last AO. Chapter 3 summarizes the principal characteristics of the detectors on-board *Suzaku*. Chapter 4 covers how the satellite time will be allocated. This includes the data rights and available time for GOs, as well as policies regarding Targets of Opportunity (TOOs). In addition, observational constraints due to the orbit, sun angle, and the pointing accuracy are described. Finally, the proposal process is reviewed, including how to submit a proposal, how they will be evaluated, and how observations will be scheduled, performed, and the results disseminated. US proposers should note especially the NASA requirements regarding the relevance of the proposed science to NASA's mission.

Chapter 5 explains how to write a strong proposal, including a summary of what constraints must be met, and what must be included in the proposal. In most cases, existing X-ray data can be used to estimate the likely *Suzaku* count rates. Simulation tools, including **XSPEC** and **PIMMS**, will assist in this and are covered in detail with examples.

The last three chapters describe the telescopes and instruments on *Suzaku*. Chapter 6 covers the five X-ray Telescopes (XRTs) on *Suzaku*. Chapter 7 reviews the X-ray Imaging Spectrometers (XISs), four CCDs with moderate spectral resolution and a large field of view. Chapter 8 explains the operation of the Hard X-ray Detector (HXD), which extends the high energy bandpass of *Suzaku* to 600 keV.

Disclaimer:

This document was prepared using the best current knowledge of the *Suzaku* satellite by the *Suzaku* teams at ISAS/JAXA and NASA/GSFC as of October 2010. It is possible that information contained in this document may contain inadvertent errors or omissions. We welcome suggestions for corrections or clarifications. Revisions of this document will be available on the *Suzaku* Web sites listed in Appendix B. Users interested in more details can also access the different instrument papers available at the web-site specified below. Please note that these papers have also been published in the special issue number 1, vol. 59 of the Publications of the Astronomical Society of Japan.

1. Spacecraft paper:
<ftp://legacy.gsfc.nasa.gov/suzaku/doc/general/suzakumemo-2006-33.pdf>
2. XRT paper:
<ftp://legacy.gsfc.nasa.gov/suzaku/doc/xrt/suzakumemo-2006-34.pdf>
3. XIS instrument paper:
<ftp://legacy.gsfc.nasa.gov/suzaku/doc/xis/suzakumemo-2006-35.pdf>
4. XIS simulations paper:
<ftp://legacy.gsfc.nasa.gov/suzaku/doc/xis/suzakumemo-2006-39.pdf>

5. HXD instrument paper:
<ftp://legacy.gsfc.nasa.gov/suzaku/doc/hxd/suzakumemo-2006-36.pdf>
6. HXD in-flight performance paper:
<ftp://legacy.gsfc.nasa.gov/suzaku/doc/hxd/suzakumemo-2006-37.pdf>

Chapter 2

Changes Since AO-5

This page summarizes the main changes to the *Suzaku* Technical Description since the last AO and *re-emphasizes* several important issues to consider for the preparation of proposals. Please note that this **should not prevent the user to carefully read the new version of the guide** as most of the numbers for simulations purposes have changed. These changes are not included here because they are part of the "standard" update of the guide.

1. The total time nominally available for observations to the community is again 11902 ks in AO-6 (11902 ks in AO-5 and AO-4, 12038 ks in AO-3, 11722 ks in AO-2). In this AO, 2 Ms will again be assigned for Key Projects (see next item), 5451 ks are assigned to Japanese observations, this includes 909 ks for proposals submitted to ESA as joint Japan-ESA observations, and 3963 ks go to US observations. The remaining 488 ks are foreseen for joint Japan-US investigations.
2. The Key Project proposal category (introduced in AO-4) will be maintained. These are comprehensive observing programs sampling a number of objects of a particular class, or surveying a large region of the sky, in order to take maximal advantage of the unique attributes of *Suzaku* to address important astrophysical problems. See http://heasarc.gsfc.nasa.gov/docs/suzaku/prop_tools/keyp6.html for additional information on this category.
3. Proposing the same targets to both the regular and the Key Project program is generally not allowed. However, ISAS/JAXA (not NASA) allows one such "duplicated proposal" to the regular program if its targets (or exposure time) constitute a subset of those in the parent Key Project proposal. See <http://www.astro.isas.jaxa.jp/suzaku/proposal/ao6/announce/index.html.en> for more information regarding ISAS/JAXA proposals.
4. In the US, the category of Long Programs (introduced in AO-3) will continue to be

maintained, for proposals with total exposure times >300 ks, encouraging, e.g., long exposures of single objects or mapping of diffuse objects. No such formal distinction will be made for proposals submitted to ISAS/JAXA or to ESA. On the other hand ISAS/JAXA proposals that are not Key Projects may not exceed total exposure times of 400 ks.

5. As before, all observations with total exposure times equal to or more than 300 ks are open to the public immediately. This includes Long Programs in the US as well as data from Key Project observations.
6. Since AO-5, individual raster scan observations have to have the same minimum exposure time of 10 ks per pointing as other observations.
7. XIS1 suffered a micro-meteorite hit in December 2009. Following diagnostic measurements showed that the scientific impact is minimal. See sections 7.1 and 7.12 for more information about previous micrometeorite hits and their effects.
8. Two *Suzaku* memos provide information about the jitter of the pointing direction that can affect observations since the end of 2009 (<ftp://legacy.gsfc.nasa.gov/suzaku/doc/general/suzakumemo-2010-05.pdf> and <ftp://legacy.gsfc.nasa.gov/suzaku/doc/general/suzakumemo-2010-06.pdf>). Note that the first one describes an effect – the observed light curves being modulated due to telescope vignetting – that can be mitigated by not using the HXD aim point.
9. The amount of charge injection for the XIS1 may be increased to improve the response in the hard band. Details will be announced by the start of the AO-6 program.
10. Since AO-5, the *Suzaku* project team accepts proposals using the P-sum/timing mode for the XIS, as well as the Normal imaging mode. In the P-sum/Timing mode, photon pile-up scarcely occurs, and a time resolution as fast as 7.8 ms can be achieved, although only a 1-dimensional image can be obtained. Note, however, that the P-sum/Timing mode can be adopted only for the XIS3, and neither the Spaced-row Charge Injection nor a CTI correction can be applied, and hence the energy resolution is significantly worse than in the normal imaging mode. The calibration accuracy is not as good as that for the normal imaging mode, either. Refer to sections 7.5.3 and 7.11.3 for more details on the P-sum/Timing mode. Switching the XIS to the P-sum/timing mode generates a relatively high load for the operation team. Hence, the total time for the P-sum/Timing mode observations is limited to 5% of the 11902 ks of ordinary observation time.
11. XIS recipes for P-sum data reduction and pile-up detection have been released, which are useful for planning observations requiring high time resolution and pile-up mitigation. Please see <http://www.astro.isas.jaxa.jp/suzaku/analysis/xis/>.

12. For feasibility studies of HXD data analyses, proposers should simulate observations with the responses and background files provided, then analyze them by varying the background by typically $\pm 3\%$ for the PIN and $\pm 1.5\%$ for the GSO. This procedure mimics the level of systematic uncertainties in the current HXD background models (see sections 5.5.2 and 8.5).
13. Note that the *Suzaku* project now has an agreement with the *Fermi* project, in addition to the existing one with the *Chandra* project, to make a modest amount of *Suzaku* time available for allocation through their proposal review processes for investigations that take advantage of joint observations. See *Chandra* and *Fermi* calls for proposals for further details.

Chapter 3

Mission Description

This chapter is a brief introduction to the satellite and its instruments and is intended as a simplified guide for the proposer. Reading it thoroughly should provide the reader with the necessary information to understand the capabilities of the instruments at a level sufficient to prepare the feasibility section of a *Suzaku* proposal.

In its first four years of operation, *Suzaku* has accumulated data from calibration, SWG and GO observations. The list of all observations performed is available in the Browse master catalog at the High Energy Astrophysics Science Archive Research Center (HEASARC) at <http://heasarc.gsfc.nasa.gov/cgi-bin/W3Browse/w3browse.pl> and at http://suzaku.gsfc.nasa.gov/docs/suzaku/aehp_time_miss.html.

Suzaku is in many ways similar to *ASCA* in terms of orbit, pointing, and tracking capabilities. *Suzaku* uses the same station (USC) as *ASCA* did for up-link and down-link, although down-link at NASA DSN is not possible with *Suzaku* (see footnote in subsection 3.2.1). As a result, the operational constraints for *Suzaku* are also similar to those of *ASCA*. *Suzaku* is placed in a near-circular orbit with an apogee of 568 km, an inclination of 31.9 degrees, and an orbital period of about 96 minutes. The maximum slew rate of the spacecraft is 6 degrees/min, and settling to the final attitude takes ~ 10 minutes, using the star trackers. The normal mode of operations will have the spacecraft pointing in a single direction for at least 1/4 day (10 ks net exposure time). With this constraint, most targets will be occulted by the Earth for about one third of each orbit, but some objects near the orbital poles can be observed nearly continuously. The observing efficiency of the satellite as measured after four years of operation is about 45%.

3.1 Brief Introduction to *Suzaku*

The scientific payload of *Suzaku* (Fig. 3.2) initially consisted of three distinct co-aligned scientific instruments. There are four X-ray sensitive imaging CCD cameras (X-ray Imag-

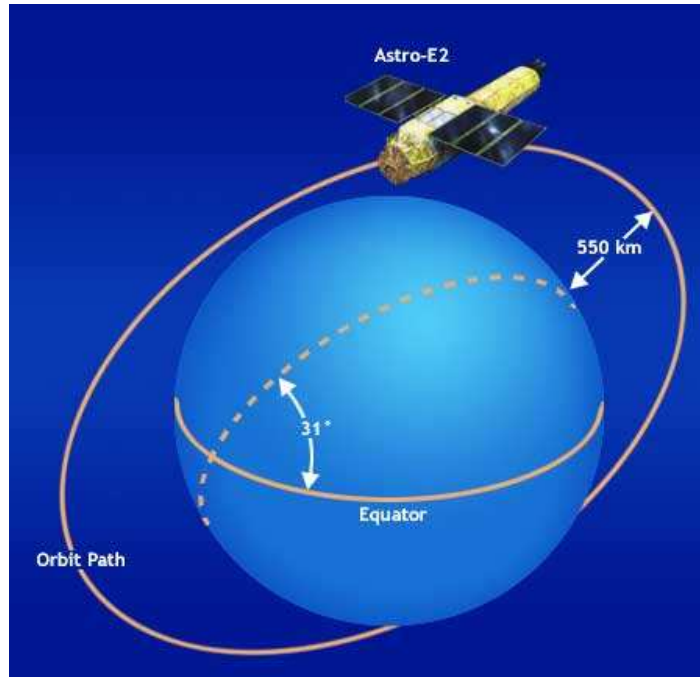


Figure 3.1: The 96 minute *Suzaku* orbit.

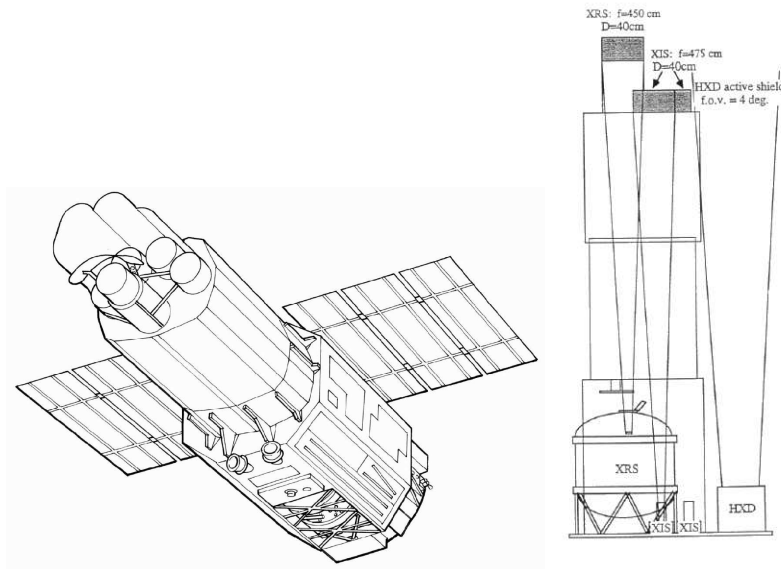


Figure 3.2: [Left] Schematic picture of the bottom of the *Suzaku* satellite. [Right] A side view of the instrument and telescopes on *Suzaku*.

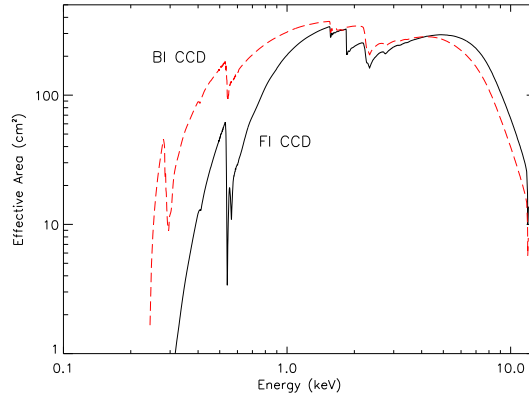


Figure 3.3: XIS effective area of one XRT + XIS system, for both the FI and BI chips.(No contamination included.)

ing Spectrometers, or XISs), three front-illuminated (FI; energy range 0.4–12 keV) and one back-illuminated (BI; energy range 0.2–12 keV), capable of moderate energy resolution. Each XIS is located in the focal plane of a dedicated X-ray telescope. The second instrument is the non-imaging, collimated Hard X-ray Detector (HXD), which extends the bandpass of the observatory to much higher energies with its 10–600 keV pointed bandpass. The X-Ray Spectrometer (XRS) is no longer operational, and will not be discussed further. Interested readers are invited to access the XRS instrument paper at <http://www.astro.isas.jaxa.jp/suzaku/doc/suzakumemo/suzakumemo-2006-38.pdf>.

All of the instruments on *Suzaku* operate simultaneously. Each of the co-aligned XRTs features an X-ray mirror with an angular resolution (expressed as Half-Power Diameter, or HPD) of $\sim 2'$ (Fig. 3.4). Figure 3.3 shows the total effective area of the XIS+XRT, which includes features due to the elemental composition of the XIS and XRT. K-shell absorption edges from oxygen (0.54 keV) and aluminum (1.56 keV) in the blocking filters are present, as well as a number of weak M-shell features between 2–3 keV arising from the gold in the XRT.

The four XISs (Fig. 7.2) are true imagers, with a large field of view ($\sim 18' \times 18'$), and moderate spectral resolution.

The HXD (Fig. 8.1) is a non-imaging instrument with an effective area of $\sim 260 \text{ cm}^2$, featuring a compound-eye configuration and an extremely low background. It dramatically extends the bandpass of the mission with its nominal sensitivity over the 10–600 keV band (Fig. 3.5). The HXD consists of two types of sensors: 2 mm thick silicon PIN diodes sensitive over 10–70 keV, and GSO crystal scintillators placed behind the PIN diodes covering 40–600 keV. The HXD field of view is actively collimated to $4.5^\circ \times 4.5^\circ$ by the well-shaped BGO scintillators, which, in combination with the GSO scintillators, are arranged in the

S/C	Orbit apogee	568 km
	Orbital period	96 minutes
	Observing efficiency	$\sim 45\%$
XRT	Focal length	4.75 m
	Field of view	17' at 1.5 keV 13' at 8 keV
	Plate scale	0.724 arcmin/mm
	Effective area	440 cm ² at 1.5 keV 250 cm ² at 8 keV
	Angular resolution	2' (HPD)
XIS	Field of view	17.8' \times 17.8'
	Bandpass	0.2–12 keV
	Pixel grid	1024 \times 1024
	Pixel size	24 μ m \times 24 μ m
	Energy resolution	~ 130 eV at 6 keV
	Effective area (incl XRT-I)	340 cm ² (FI), 390 cm ² (BI) at 1.5 keV 150 cm ² (FI), 100 cm ² (BI) at 8 keV
HXD	Time resolution	8 s (Normal mode), 7.8 ms (P-Sum mode)
	Field of view	4.5° \times 4.5° ($\gtrsim 100$ keV)
	Field of view	34' \times 34' ($\lesssim 100$ keV)
	Bandpass	10–600 keV
	– PIN	10–70 keV
	– GSO	40–600 keV
	Energy resolution (PIN)	~ 4.0 keV (FWHM)
	Energy resolution (GSO)	$7.6/\sqrt{E_{\text{MeV}}}$ % (FWHM)
	Effective area	~ 160 cm ² at 20 keV, ~ 260 cm ² at 100 keV
HXD-WAM	Time resolution	61 μ s
	Field of view	2 π (non-pointing)
	Bandpass	50 keV–5 MeV
	Effective area	800 cm ² at 100 keV / 400 cm ² at 1 MeV
	Time resolution	31.25 ms for GRB, 1 s for All-Sky-Monitor

Table 3.1: Overview of *Suzaku* capabilities.

so-called phoswich configuration. At energies below ~ 100 keV, an additional passive collimation further reduces the field of view to $34' \times 34'$. The energy resolution is ~ 4.0 keV (FWHM) for the PIN diodes, and $7.6 / \sqrt{E}$ % (FWHM) for the scintillators (where E is energy in MeV). The HXD time resolution for both sensors is 61 μ s. While the HXD is intended mainly to explore the faintest hard X-ray sources, it can also tolerate very bright sources up to ~ 10 Crab. The HXD also performs as an all-sky monitor (the Wide-band

All-sky Monitor (WAM), which can detect GRBs and other sources. Although observers will receive data from the WAM, it cannot be proposed for directly and has special rules regarding data rights; see Chapter 4.

Because the HXD bore-sight axis, with the highest effective area, is about 3.5 arcmin shifted from that of the XISs, *Suzaku* supports two aimpoints, XIS and HXD oriented. Users are requested to select which pointing axis is best for your observations. For the XIS, choosing the XIS aimpoint provides a $\sim 10\%$ larger XIS effective area than the HXD aimpoint. Conversely for the HXD, the HXD aimpoint provides a $\sim 10\%$ larger HXD effective area than the XIS aimpoint. Note that a 10% increase in effective area corresponds to a 20% increase in observing time for background dominated observations. For source dominated observations, the effect is 10%. Please take into account these effects in your observation plan.

3.2 Operational Constraints

3.2.1 Telemetry Rates

Suzaku carries a 6 Gbit data recorder. Data will be down-linked to USC at a rate of 4 Mbps for a total of 2 Gbits per pass, up to 5 times a day. This allows a maximum of 10 Gbits of data to be obtained per day, but fewer passes may be available to *Suzaku* as it will share the use of USC ground station with other ISAS satellites¹. Data can be recorded at 4 different rates: Super-High (524 kbps), High (262 kbps), Medium (131 kbps), and Low (33 kbps).

¹Unlike ASCA, NASA DSN stations will not be used, since a 4 Mbps down-link is not possible at DSN stations.

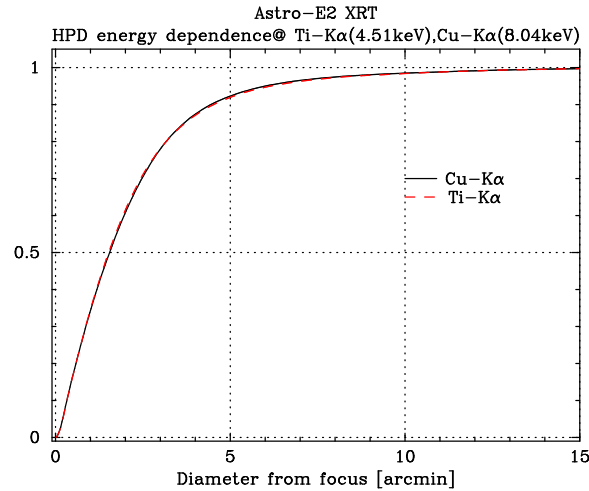


Figure 3.4: The Encircled Energy Function (EEF) showing the fractional energy within a given radius for one quadrant of the XRT-I telescopes on *Suzaku* at 4.5 and 8.0 keV.

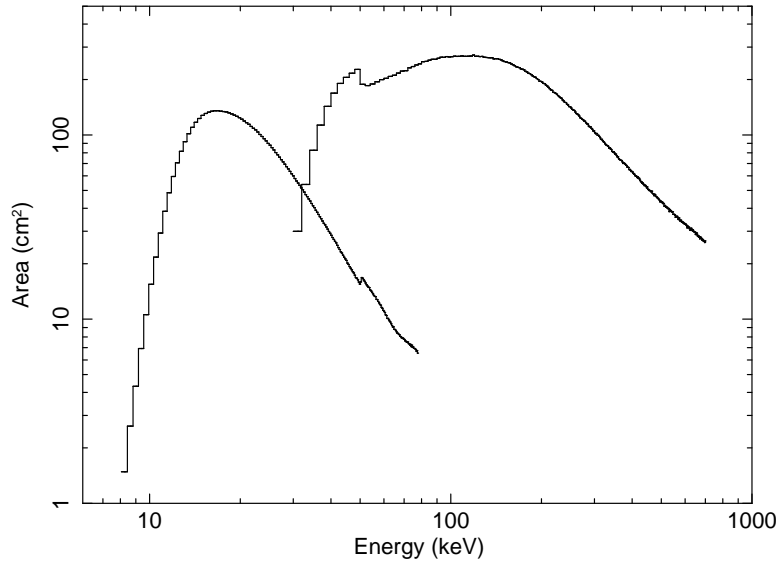


Figure 3.5: Total effective area of the HXD detectors, PIN and GSO, as a function of energy.

The recording rate will be changed frequently throughout an observation, according to a sequence that will be determined by the operations team at ISAS. This is to optimize the selection of the data rates and the usage of the data recorder, taking into account the expected count rates supplied by the proposers. Thus an accurate estimation of the count rates is important for the optimization of the mission operation. **We emphasize that proposers cannot arbitrarily choose the data recording rate.**

On-source data will usually be recorded at High (during contact orbits, during which the satellite passes over USC) or Medium (during remote orbits, without USC passes) data rate. The Low rate will primarily be used for times of Earth occultations and SAA passages, as the background rates in the XIS and HXD exceed their telemetry allocation limit at Low data rate. The telemetry limits for the XIS are presented in Chapter 7. The XIS data mode will be chosen for each data recording rate used to prevent telemetry saturation, based on the count rate supplied by the proposer.

3.2.2 Summary

Suzaku excels for observations such as:

- Studies of diffuse soft X-ray sources with low surface brightness: the low background, soft X-ray sensitivity, and near-Gaussian response of the XIS BI CCD makes such targets an excellent use of *Suzaku*.

- Observations requiring sensitivity both above and below 10 keV, especially measuring the Fe K complex simultaneously with the hard (>10 keV) continuum.
- Rapid variability studies on 10 ms time scales. The best time resolution available on the XIS is ~ 7.8 ms, while the HXD time resolution is $\sim 61 \mu\text{s}$ (see Table 3.1)

Suzaku is less appropriate for:

- Studies requiring primarily high spatial resolution. *Chandra*'s PSF is $\sim 100\times$ smaller than *Suzaku*'s, while the *XMM-Newton* PSF is $\sim 10\times$ smaller.
- Studies requiring primarily high spectral resolution. The gratings on *Chandra* and *XMM-Newton* have significantly higher resolution than the XIS.

3.3 Calibration

Table 3.2 summarizes the calibration items of all scientific instruments, the current status, and their expected and measured accuracy.

These values are the 90% limits, equivalent to 1.6σ . Note that the values listed are those required from the scientific purpose and ultimate goals which are possible to be realized on the basis of the instrument design.

Table 3.2: Error Budgets of Scientific Instrument Calibrations.

	Calibration Item	Oct 2008	Requirement	Goal
XRT-I/XIS	On-axis effective area ^a	~2%	5%	5%
	Vignetting ^a	~10%	5%	2%
	On-axis EEf ^b	~3%	5%	1%
	Off-axis EEf ^c	~3%	20%	2%
	Optical axis position in XIS	~0.5'	<0.2'	<0.2'
	Energy scale ^d	max(0.2%, 5 eV)	0.1%	0.1%
	Energy resolution (FWHM) at 5.9 keV	5% ^e	1%	1%
	Contamination thickness ^f	10 ¹⁸ cm ⁻²	N/A	N/A
	OBF integrity	unbroken	broken/unbroken	broken/unbroken
HXD	Absolute effective area	20%	20%	5%
	Relative effective area	10%	10%	5%
	Vignetting	5%	10%	5%
	Background modeling (PIN) ^g	3 ~ 5%	10%	1%
	Background modeling (GSO) ^g	1.5 ~ 2%	10%	3%
	Absolute timing ^h	300 μ s	300 μ s	100 μ s
	Relative timing ^h	1.9 \times 10 ⁻⁹	10 ⁻⁸	10 ⁻¹⁰
	GRB absolute timing	~2 ms	10 ms	1 ms

a: Valid in the 2-10 keV band. Calibration uncertainty may become larger outside this energy range, especially below 0.3 keV (BI chip) and above 10 keV. We calibrated the effective area using spectral parameters of the Crab emission as those given by Toor & Seward (1974, AJ, 79, 995).

b: For all integration radii from 1'-6'. No error on attitude control is included.

c: As on-axis but for all XIS f.o.v. No calibration is currently scheduled.

d: For the normal mode data. Uncertainties of the energy scale increase when the burst and/or window options are applied.

e: When xisrmfgen is used. Note that an error of 5% in the energy resolution could produce an artificial line width of as large as ~25 eV in sigma at the iron band. Energy resolution with the spaced-row charge injection is under investigation.

f: Uncertainty represented as the carbon-equivalent column density. Valid only at the center of the field of view.

g: Modeling accuracy depends on energy-band and exposure. See Chapter 8.5 for typical examples.

h: The Crab and PSR B1509-58 pulses are clearly detected in the quick look analysis of calibration data.

Chapter 4

Observation Policies

In AO-6, 100% of the observing time available is used for GO observations. The current schedule for the time allocation between Japanese and US PIs is given in Table 4.1. The AO will run for a year starting in April 2011.

In 2009, the new category of Key Project proposals was introduced. Key Projects are defined as comprehensive observing programs sampling a number of objects of a particular class, or surveying a large region of the sky, in order to take maximal advantage of the unique attributes of *Suzaku* to address important astrophysical problems. See http://heasarc.gsfc.nasa.gov/docs/suzaku/prop_tools/keyp6.html for additional information on this new category.

After five years of operation, we know that the actual observing efficiency is about 38 ks per day and we assume 360 days of operations per year. From the total of 13680 ks, we subtract 3% of the available time as observatory time used for satellite maintenance and similar purposes, and 5% for ongoing calibration observations. Finally, 5% are earmarked as Director's Discretionary Time (DDT) for unproposed Target of Opportunity (TOO) proposals (including observations of gamma-ray bursts) and other important observations, granted at the mission director's discretion. Therefore $13680 \times 0.87 = 11902$ ks are nominally available to the community via the proposal selection process.

The project will over-subscribe this total by 40% including category C targets for which the observation is not guaranteed (see Section 4.4 below). If the actual sum of the observatory, calibration, and director's times is less than 12%, additional C targets will be observed.

In this AO, 2 Ms will be assigned for the Key Projects. 5451 ks are assigned to Japanese observations and 3963 ks go to US observations. The remaining 488 ks are set aside for joint Japan-US investigations. When the respective national reviews have selected the same target, the two proposals will be merged if both teams indicated their willingness to collaborate on the RPS form, and the observation will be counted against the Japan-US

Phase	Months Post-Launch	SWG	Japan (ESA)	US	Japan/US	Key Project
AO-6	69-80	0	5451 (909)	3963	488	2000

Table 4.1: *Suzaku* time allocated to each group of observers. The ESA time is in parentheses as it is part of the Japanese allotment.

time. If such mergers do not take up 488 ks, the remainder will be divided between separate Japanese and US investigations. Additionally, within the "Japanese" allocation, 909 ks are reserved for proposals submitted to ESA as joint Japan-ESA observations. Proposals from non-US, non-ESA countries will be accepted within the Japanese time up to the ESA portion.

The nationality of the PI's institution determines which agency should receive the proposal. That is, researchers at US institutions must submit their proposals to NASA and those at institutions in ESA member countries must submit theirs to ESA (regardless of their actual nationality). As an exception, ESA PIs who wish to participate in Key Projects should submit their proposals to ISAS/JAXA. While the ISAS/JAXA proposal process is primarily aimed at researchers resident in Japan, proposals from researchers in other (non-US, non-ESA) countries will also be considered. In addition, Co-Is from any country may be part of any proposal.

In the US, the category of "Long Program" (introduced in AO-3) will be maintained, for proposals with a total exposure time >300 ks. No such formal distinction will be made for proposals submitted to ISAS/JAXA or to ESA. On the other hand ISAS/JAXA proposals that are not Key Projects may not exceed total exposure times of 400 ks. Note, that certain proposals could be classified as either a Long Program or a Key Project in the US, but that the Key Project proposal category is more broadly defined (see definition and link given at the beginning of this chapter).

Proposing the same targets to both the regular and the Key Project program is generally not allowed. However, ISAS/JAXA (but not NASA) will allow one such "duplicated proposal" to the regular program if its targets (or exposure time) constitute a subset of those in the parent Key Project proposal. See

<http://www.astro.isas.jaxa.jp/suzaku/proposal/ao6/announce/index.html.en> for more information regarding ISAS/JAXA proposals.

4.1 Data Rights

The data rights policy for *Suzaku* is similar to previous missions. The normal exclusive period for GO data is one year, **except for Key Project Observations, for proposals with exposure time >300 ksec ("Long Program" proposals in the US) and DDT**

data which are made public immediately.

Accepted targets will be classified into three categories. Priority A targets including Key Project observations will be preferentially observed during the AO-6 period (April 2011 to March 2012). Priority B targets will be scheduled in this period as much as possible, but may be carried over to the next cycle. Priority C targets will be used as fillers when there are gaps in the schedule. For the total available time T , we currently plan to accept $0.6T$, $0.3T$, and $0.5T$ as As plus Key Projects, Bs, and Cs (for a total over-subscription by 40%).

During AO-5, category A and B targets will be considered complete if 90% (for A targets) or 70% (for B targets) of the proposed time is obtained on the source. In general, supplementary observations will be performed for A or B targets that do not meet the completion criteria, although it may not always be possible in case of time critical observations.

During the GO phase, data from calibration and TOOs requested outside the proposal process (see below) will not be considered proprietary.

4.2 Target of Opportunity Proposals

TOO proposals are allowed for *Suzaku* through the normal proposal process, although they must be highly ranked (see below) to be accepted. Proposals with TOOs should not be mixed with non-TOO targets, except in Key Project proposals where a mixture of TOO and non-TOO targets are allowed. TOO proposals are allowed for short-lived events in known objects the timing of which is uncertain. These should only include unpredictable phenomena in a specific target (e.g., SS Cyg in outburst), not a generic target (e.g., the next Galactic supernova). The trigger criteria **must** be explicit and quantifiable, and stated in detail in the proposal text; a brief summary should appear in the “Remarks” section of the target form. In addition, TOO proposals **must provide an estimated probability of a successful trigger** during the AO period. It is **the PI’s responsibility** to notify the *Suzaku* project when the criteria are met. **Generic TOOs without a specific target (such as “a nearby supernova”) will not be accepted. In the same spirit, the number of targets in TOO proposals should not exceed 5.** Gamma-ray bursts or any genuinely unpredictable events may be observed outside the proposal process, as part of the 5% DDT. Data from such observations will not have a proprietary period.

To request such unproposed TOO observations, please send an e-mail to: `suzaku_managers` <at> `astro.isas.jaxa.jp` using the format specified in <http://www.astro.isas.jaxa.jp/suzaku/planning/gtoo/>.

4.3 Pointing Constraints

The Solar panels on the *Suzaku* satellite are fixed. This places a restriction on the pointing direction with respect to the satellite-Sun line: the Sun angle constraint is normally 65–110 degrees. This means that at any given time of the year, only a swath of the sky 45 degrees wide is accessible for astronomical observations, and thus most celestial sources are available for observations for about 50 days every 6 months. If a specific observing date or a coordinated observation with other missions is required, the proposer must first determine if the observation is possible. This can be done using the “Viewing” tool on the *Suzaku* proposal web-site (see Appendix B).

Long (>1 day) observations are the norm for *Suzaku*. A large number of short observations is an inefficient use of the satellite because of the unusable time during slews and attitude settling. The pointing is expected to be accurate to 0.3 arcmin and can be reconstructed to better than 0.2 arcmin, except during the initial settling period of up to 10 minutes. Moreover, there is a limit on the number of slews that can be uploaded to *Suzaku*. For these reasons, a minimum exposure time of 10 ks has been set for all proposed observations.

Contiguous observations, i.e., observations not disrupted by the observation of another target, are generally guaranteed up to exposures of not more than 100 ks. This limitation is due to moon light constraints for the star trackers’ field of view, conflicts with other time critical observations, and other operational/planning difficulties. While the operation team does accept requests for uninterrupted observations longer than the 100 ks, these are conducted on a best-effort basis.

Even during shorter pointed observations, there will typically be interruptions due to the location of *Suzaku* in a low Earth orbit: Normally, a target will be occulted by the Earth for ~30 minutes every satellite orbit. In addition, *Suzaku* will pass through the South Atlantic Anomaly (SAA) during parts of 5 or 6 orbits every day. Due to the harsh radiation environment of the SAA, scientific observation is not possible during SAA passages. There are other variations in the particle background, depending primarily on the Cut-Off Rigidity (COR)¹. The optimal criteria to reduce times of high background while maximizing the science return are still being determined from SWG observations, please check the *Suzaku* web-sites (see Appendix B) for the most up-to-date suggestions.

There are also orbital constraints on the orientation of the projection of the XIS CCDs on the sky. Since the *Suzaku* XIS arrays are square, with calibration sources in different corners, selecting a specific roll angle is rarely significant. However, if a specific roll angle is scientifically advantageous, the proposer must first determine if it is allowed. This can be done using the MAKI tool described in Section 5.7. Then the required roll range can be

¹*Suzaku* is protected from solar and cosmic-ray particles by the geomagnetic field. The COR is an indicator of the minimum momentum required for a particle to reach a specific location, given the average geomagnetic field configuration.

entered on the RPS proposal form. For objects close to the ecliptic poles it is possible to arrange for any XIS orientation by scheduling observations at a specific time, but for those located close to the ecliptic, the XIS will project on the sky in a nearly fixed orientation. **Note that any roll constraint will make a proposal time critical.**

It is possible to specify the time of observations (time critical, or TC, observations) in order to observe during specific phases or for simultaneous observations. Monitoring observations (repeated observations with a specified interval) or roll-angle constrained observations are also considered time critical, and must be so flagged on the proposal form. Those interested in submitting TC or TOO observations as part of a Key Project proposal should contact the *Suzaku* team at `suzaku_managers <at> astro.isas.jaxa.jp` beforehand to ensure their feasibility. The total accepted time of the TC and TOO proposals is less than 15% of the total observation, and proposers should justify their requirements carefully.

Overall the proposers are strongly urged to provide accurate information. All information that is indispensable for operation planning should be provided on the electronic forms. The PIs are advised to utilize the “Remarks” area if they have detailed requests which cannot be expressed with the check boxes/pull-down menus.

4.4 Events After Submission

After the *Suzaku* proposal deadline, there will be three independent proposal reviews for the US, Japan, and ESA proposals. Each review will create a target list from the proposed observations, ranking the accepted targets as category A, B, or C. Only category A and B targets are guaranteed to be observed. As stated above, TOOs and time critical observations are only accepted within 15% of the total time. Category C targets will be observed as time permits, and will not be carried over into the next AO if not observed in this AO. An international merging committee will collate the three target lists and produce a single, unified list. Overlaps between US and Japanese targets will be resolved, either by merging the investigations (if both parties are willing) or by choosing one. In the latter process, the priority given by the national reviews, as well as the lengths of the accepted observations, will be considered. The final target list will be $\sim 40\%$ oversubscribed. Category A and Key Project targets will have 60% of the available time, category B 30%, and category C 50%. US-based investigators may propose for funding once notified that their target has been accepted. This process is described in the ROSES-2010 document. Further details of this process will be made available on the NASA *Suzaku* GOF web-site listed in Appendix B.

Even though observations are scheduled to acquire roughly the approved exposure time and although this is usually achieved with *Suzaku*, occasional losses of usable observation time are inevitable. As mentioned above, Category A observations will be deemed complete when they have received at least 90% of the approved time. Note that this will be judged based on the good time intervals of the cleaned XIS event files after the standard screening.

Dead times (including those due to the use of the burst option) are not taken into account. Also, the standard screening for the HXD is more strict, so the effective exposure for the HXD is often smaller than that of the XIS by 20% or more. Additional observations will be scheduled automatically for those non-time-critical targets the observations of which are considered incomplete by the project scientist at ISAS. In the case of time-critical observations which are incomplete or unusable, it will be the PI's responsibility to determine the best course of action.

Each PI will be assigned a contact scientist, either at ISAS or the NASA *Suzaku* GOF, who will work with the PI to assure the maximum science return. This will include double-checking coordinates, count rates and finalizing configurations (nominal pointing, XIS modes, ...). It is important to note that once an observation has been scheduled, any delay in responding to questions from the contact scientist may result in targets being removed from the schedule. We do not have a mechanism to approve coordinated observations with *Suzaku* and another observatory through a single proposal. It is the PI's responsibility to secure observing time with other observatories, when simultaneous observations are desirable. **Please note that the *Suzaku* component of such a proposal may be approved contingent on the success of other proposals.** Special scheduling requests and TOO's will be accommodated on a best effort basis. For simultaneous observations, the mission scheduler at ISAS, in consultation with the contact scientist, will contact the PI in advance for detailed scheduling information, and will often work directly with schedulers of other missions. During the AO-1–AO-5 observing periods, the *Suzaku* scheduling team made every effort to accommodate requests of coordinated/simultaneous observations with other facilities and we expect that it will continue to do so during AO-6.

Once the observation has been completed, the data will be promptly run through the processing pipeline and put into both the US and Japanese archives, initially in encrypted form. The PI will be sent the decryption key along with instructions on how to download and decrypt the data. The only exception to the one year exclusive period for GO data, concerns the HXD Wide-band All-sky Monitor (WAM) data (see Chapter 8). The WAM is primarily used for anticoincidence shielding in the HXD, but it can also be used as an all-sky monitor, detecting solar flares, gamma-ray bursts, and other bright X-ray sources (e.g., Cyg X-1). All data from the WAM will be monitored by the HXD team, which will alert the GRB community to any detected bursts. In addition, the HXD team will make analysis results from WAM, such as light curves and fluences, available to the public as soon as possible. These may be used to put limits on GRBs or other events triggered by other satellites or observatories. However, the PI will receive the complete WAM data from their observation and will share data rights with the *Suzaku* team for the normal 1 year proprietary period. This unusual arrangement is due to the time-critical and non-source-specific nature of the WAM data.

With the exception of the code that converts raw binary telemetry into FITS format files, all *Suzaku* software is written as FTOOLS and distributed through the *Suzaku* team

at ISAS/JAXA and the NASA/GSFC HEASARC. This includes the tools used in the processing. All calibration files are distributed through the HEASARC `caldb` (calibration database) system. This enables users to apply any calibration updates themselves. The *Suzaku* team at ISAS and the NASA *Suzaku* GOF provide additional FTOOLS that may be necessary or desirable for analyzing *Suzaku* data. The use of other software packages will only be supported at a lower priority level.

Chapter 5

Writing A Successful *Suzaku* Proposal

Each *Suzaku* proposal must include at a minimum the source coordinates, exposure time, instrument configuration and expected count rates, and any observing constraints within the four page limit. The review panels will base their decision primarily upon the justification of the proposed science to be done with the data. This chapter describes how to prepare a strong proposal, including the various software tools available to assist the proposer.

5.1 First Checks

5.1.1 Viewing

One of the first tasks in preparing a proposal is determining when and for how long a target can be observed as there is very little use to simulate a source that cannot be observed. This can be easily done with **Viewing**, a simple web-based interactive tool (see Appendix B) that can determine visibility for many different satellites. To use **Viewing**, simply enter the target name or coordinates, and select the satellite. **Viewing** will return all the available dates when that target is observable.

5.1.2 Previous Observations

Another initial check to be performed before starting sophisticated simulations is to ensure that the target has not yet been extensively observed by *Suzaku*, e.g., using **Browse**. Users should also check the observations log located at http://suzaku.gsfc.nasa.gov/docs/suzaku/aehp_time_miss.html as some of the tar-

gets (category C) may have been accepted but not observed.

5.2 Proposal Ingredients

While it is conceivable that one would wish to study a previously unknown X-ray source with *Suzaku*, a more likely scenario would involve a spectroscopic study of an object with known X-ray flux. A viable proposal should state the scientific objective of the observation and show that *Suzaku* can achieve this objective. Observations that require one or more of *Suzaku*'s unique capabilities would be especially strong candidates.

Every *Suzaku* proposal must have an estimate of the expected source count rates from the proposed target for all detectors. This rate is used both by the reviewers to evaluate the viability of the proposal and the operations team to evaluate any safety concerns. The simplest tool to use in estimating the expected XIS or HXD count rate is PIMMS. This tool is freely available as a stand-alone tool or on the web as WebPIMMS (see Appendix B). The next level of detail is provided via simulations using XSPEC, and such simulations should provide significant insight into the expected spectrum obtained from a proposed observation. A brief guide to XSPEC simulations is given in section 5.4. In many cases, this should be sufficient for a point source. There are also tools available to simulate imaging data, which may be useful for an extended source or a particularly bright source. In particular, the most powerful tool is `xissim`, which can use a FITS format image with an assumed spectral shape of the source to estimate the distribution of events in all elements of the XIS detectors.

5.3 PIMMS & WebPIMMS

PIMMS is an interactive, menu-driven program, which has an extensive HELP facility. It is also available as the web-based tool WebPIMMS. In either case, users specify the flux and spectral model with its parameters, and PIMMS/WebPIMMS returns the predicted count rate. PIMMS/WebPIMMS can be used for a variety of other instruments, so if, for instance, the count rate and spectrum of a given source observed with the *ROSAT* PSPC is known, PIMMS/WebPIMMS can estimate the expected count rates for *Suzaku*'s instruments. The limitations of the input source must be considered carefully. For example, *ROSAT* had no significant response to X-rays above ~ 2.4 keV, and so is not useful when estimating the HXD GSO count rate.

5.4 XSPEC Simulations

Perhaps the easiest tool for simulating X-ray spectra is the **XSPEC** program (a part of the **XANADU** software package), which is designed to run on a variety of computer platforms and operating systems and is freely distributed on the NASA GSFC HEASARC web-site (see Appendix B). The simulation of an XIS observation requires the current instrument redistribution matrix (the so-called RMF file) and the energy-dependent effective area of the instrument (the so-called ARF file), while the simulation of an HXD observation requires the current instrument response (the so-called RSP file). These files are available on the Web or via anonymous FTP (see Appendix B).

The procedure for simulations is relatively simple: if the **XSPEC** program is installed, one should start **XSPEC**, making sure that the proper RMF, ARF, and RSP files are accessible. Within **XSPEC**, one should specify the spectral model, such as hot thermal plasma or the like (via the *model* command). Specifying the model will drive **XSPEC** to query for the model parameters (such as the temperature and abundances for an **APEC** collisional plasma model), as well as its normalization. The key command to create a simulated spectrum is the *fakeit* command, which will query for the RMF and ARF files, when simulating XIS, or for an RSP file, in the HXD case. The *fakeit* command will also request the data filename and the length of the observation to be simulated. One can then use the resulting spectrum within **XSPEC** to determine the sensitivity of the simulated data file to changes in the model parameters. Users should adjust the normalization of their input models to reflect the actual count rate or flux (absorbed or unabsorbed) of their source.

5.4.1 WebSPEC Simulations

Some of the features of **XSPEC** are also available as a web-based tool on the HEASARC web-site (see Appendix B). **WebSPEC** calls **XSPEC** behind the scenes, so the description above applies here as well.

After selecting the instrument, **WebSPEC** allows the user to choose the spectral model, such as an absorbed collisional plasma or a power-law spectrum with an absorption component. The next page will then query for the model parameters (such as the temperature and abundances for an **APEC** collisional plasma model), as well as its normalization. In addition, it queries for the simulation parameters, i.e., the exposure, upper and lower energies, and the number of bins to use in the spectral plot. **WebSPEC** will then create a simulated spectrum after clicking the “Show me the Spectrum” button, using the *fakeit* command. This folds the specified model through the instrument response and effective area, calculating the observed count rate and fluxes as well. **WebSPEC** will then allow one to download the postscript file of the spectrum, change the model parameters, or re-plot the data.

5.5 Examples

In order to show how to estimate the proper exposure, we include some simple examples of XIS and HXD observations that illustrate the process.

5.5.1 Faint Oxygen Emission from the Local Hot Bubble

The Local Hot Bubble is the proposed origin for at least some of the 1/4 keV emission seen in the *ROSAT* All-Sky Survey at all latitudes. Although *Suzaku* has some sensitivity at 1/4 keV, a more profitable approach to finding this emission is to detect the OVII emission that should accompany it. In this case we need to calculate the expected count rate from the OVII and compare it to the expected background.

We first need the expected flux, based on published papers or the PI's model. In this case, we expect the surface brightness to be $0.34 \text{ ph/cm}^2/\text{s/sr}$, based on a number of papers. Since the XIS field of view is $18' \times 18'$, this value corresponds to a total surface brightness in one XIS of $9.3 \times 10^{-6} \text{ ph/cm}^2/\text{s}$. The next question is the effective area of the XIS instruments at the line energy. OVII is in fact a complex of lines, centered around 0.57 keV. Examining the effective area plots for the XIS in Chapter 3, we see that the effective area at 0.57 keV in the BI CCD is $\sim 140 \text{ cm}^2$; for the FI CCDs it is $\sim 90 \text{ cm}^2$. The curves shown on Fig. 3.3 do not include the contamination effect. The computation below is only given as an example. Please note that the more current effective area curves for the FI and BI CCDs can also be found by loading their responses into XSPEC and using the `plot efficiency` command. *Warning:* The XIS RMF response matrices are **not** normalized, and thus must be combined with the ARF files to determine the total effective area. With the expected flux and the effective area, we can now determine the expected count rate in the BI and FI CCDs to be 1.3 and 0.87 counts/ks. This is obviously a extremely low count rate and so the expected background is very important. The resolution of the XIS is quite good, as shown in Chapter 7, at 0.57 keV a bin of width 60 eV will contain most of the emission. The XIS background rate (see section 7.8) at this energy is only 0.05 counts/s/keV in both the FI and BI detectors, so we can expect a background of 3 counts/ks. In both the FI and BI detectors the line will be below the background, but this does not intrinsically hinder detection. As will be seen below, in the HXD this is the norm rather than the exception. One aid for this observation is that the OVII line is relatively isolated in this energy range, with the exception of the nearby OVIII line. Assume we wish to detect the OVII feature with 3σ significance. The total count rate in the XIS-S1 (the BI CCD) in our energy band will be 4.3 counts/ks, with 3 counts/ks of background. In an N ks observation, we will measure the signal to be $1.3 \times N \pm \sqrt{4.3 \times N}$. To achieve a 3σ result, then, we need $1.3 \times N / \sqrt{4.3 \times N} > 3$, or $N > 23 \text{ ks}$.

5.5.2 Hard Tails of XRBs

Another common observation will be to search for faint hard X-ray tails from sources such as X-ray binaries. We describe here how to simulate such an observation, including the all-important HXD background systematics, which will dominate all such observations.

The first step is to download the latest versions of the background template files and the response files from the web-site listed in Appendix B. The HXD web-site will also describe the current best value for the systematic error in background estimation. For this AO, proposers should carefully read Chapter 8 and evaluate the systematic errors for the PIN and the GSO backgrounds in the energy band of interest, and at the exposure level chosen. For example, for a 100 ks exposure, the value for the PIN in the 15–40 keV band and the GSO in the 50–100 keV band can be estimated to be $\sim 3\%$ and $\sim 1.5\%$, respectively. Since the energy bands are important in this case, the associated errors should first be estimated and then used in the procedure described below. In addition, the proposer should also check if contaminating sources exist in the FOV of the HXD, using existing hard X-ray source catalogs from satellites such as *RXTE*-ASM, *INTEGRAL*, and *Swift*, before beginning this process.

We set up XSPEC for simulating by reading the background template files as both data and background along with the response files:

```
XSPEC12>data ae_hxd_pinbkg_20101012.pha ae_hxd_gsobkg_20101012.pha
```

```
2 spectra in use
```

```
Spectral Data File: ae_hxd_pinbkg_20101012.pha Spectrum 1
Net count rate (cts/s) for Spectrum:1 4.735e-01 +/- 3.973e-04
Assigned to Data Group 1 and Plot Group 1
Noticed Channels: 1-256
Telescope: SUZAKU Instrument: HXD Channel Type: PI_PIN
Exposure Time: 3e+06 sec
No response loaded.
```

```
Spectral Data File: ae_hxd_gsobkg_20101012.pha Spectrum 2
Net count rate (cts/s) for Spectrum:2 4.397e+01 +/- 3.829e-03
Assigned to Data Group 1 and Plot Group 2
Noticed Channels: 1-512
Telescope: SUZAKU Instrument: HXD Channel Type: PI_SLOW
Exposure Time: 3e+06 sec
No response loaded.
```

```
***Warning! One or more spectra are missing responses,
```

```

and are not suitable for fit.
XSPEC12>back ae_hxd_pinbkg_20101012.pha ae_hxd_gsobkg_20101012.pha
Net count rate (cts/s) for Spectrum:1 0.000e+00 +/- 5.619e-04 (0.0 % total)
Net count rate (cts/s) for Spectrum:2 0.000e+00 +/- 5.414e-03 (0.0 % total)
***Warning! One or more spectra are missing responses,
and are not suitable for fit.
XSPEC12>resp ae_hxd_pinhxnome9_20100731.rsp ae_hxd_gsohxnom_20100524.rsp
Response successfully loaded.
Response successfully loaded.

```

We first create background spectra with the correct statistics, by simulating an observation with no source flux using the `fakeit` command. In the case of the PIN, the simulated background exposure is a factor 10 higher than the exposure of the source observation to be simulated (here 10^6 s), following the prescription for PIN data analysis. In the case of the GSO the simulated background exposure is equal to the exposure of the source observation (here 10^5 s).

```

XSPEC12>model powerlaw

Input parameter value, delta, min, bot, top, and max values for ...
           1           0.01           -3           -2           9           10
1:powerlaw:PhoIndex>1
           1           0.01           0           0           1e+24           1e+24
2:powerlaw:norm>0

=====
Model powerlaw<1> Source No.: 1   Active/On
Model Model Component  Parameter  Unit      Value
par  comp
  1    1   powerlaw   PhoIndex      1.00000    +/-  0.0
  2    1   powerlaw   norm            0.0      +/-  0.0
-----

Chi-Squared =           0.0 using 768 PHA bins.
Reduced chi-squared =           0.0 for    766 degrees of freedom
Null hypothesis probability = 1.000000e+00

***Warning: Chi-square may not be valid due to bins with zero variance
           in spectrum number(s): 1 2

Current data and model not fit yet.

```

```
XSPEC12>fakeit
Use counting statistics in creating fake data? (y):
Input optional fake file prefix:
Fake data file name (ae_hxd_pinbkg_20101012.fak): pin_10mCrab_1Ms.bkg
Exposure time, correction norm (3.00000e+06, 1.00000): 1000000
Fake data file name (ae_hxd_gsobkg_20101012.fak): gso_10mCrab_100ks.bkg
Exposure time, correction norm (3.00000e+06, 1.00000): 100000
```

No ARF will be applied to fake spectrum #1 source #1

No ARF will be applied to fake spectrum #2 source #1

2 spectra in use

```
Chi-Squared =          609.94 using 768 PHA bins.
Reduced chi-squared =          0.79627 for      766 degrees of freedom
Null hypothesis probability =  9.999906e-01
```

```
***Warning: Chi-square may not be valid due to bins with zero variance
            in spectrum number(s): 1 2
```

Current data and model not fit yet.

Now we assume a spectrum for our source; here, we use a Crab-like spectrum (Toor & Seward 1974 AJ, 79, 995) with a photon index of 2.1, a hydrogen column density N_H of $3 \times 10^{21} \text{ cm}^{-2}$, and 10m Crab flux. This can be set up in XSPEC via the following commands (note that while the response files are still present from the previous step, the simulated background files from the previous step should be loaded as background files, and the data files do not matter):

```
XSPEC12>back pin_10mCrab_1Ms.bkg gso_10mCrab_100ks.bkg
Net count rate (cts/s) for Spectrum:1 1.808e-17 +/- 9.720e-04 (0.0 % total)
Net count rate (cts/s) for Spectrum:2 -4.069e-15 +/- 2.966e-02 (-0.0 % total)
```

```
Chi-Squared =          3e-26 using 768 PHA bins.
Reduced chi-squared =          4e-29 for      766 degrees of freedom
Null hypothesis probability =  1.000000e+00
```

```
***Warning: Chi-square may not be valid due to bins with zero variance
            in spectrum number(s): 1 2
```

```

Current data and model not fit yet.
XSPEC12>model phabs*powerlaw

Input parameter value, delta, min, bot, top, and max values for ...
      1      0.001      0      0      100000      1e+06
1:phabs:nH>0.3
      1      0.01      -3      -2      9      10
2:powerlaw:PhoIndex>2.1
      1      0.01      0      0      1e+24      1e+24
3:powerlaw:norm>0.097

=====
Model phabs<1>*powerlaw<2> Source No.: 1   Active/On
Model Model Component  Parameter  Unit      Value
par  comp
  1    1   phabs       nH          10^22    0.300000    +/-  0.0
  2    2   powerlaw    PhoIndex      2.10000    +/-  0.0
  3    2   powerlaw    norm          9.70000E-02 +/-  0.0
-----

Chi-Squared =      218733.5 using 768 PHA bins.
Reduced chi-squared =      285.9261 for      765 degrees of freedom
Null hypothesis probability =    0.000000e+00

***Warning: Chi-square may not be valid due to bins with zero variance
           in spectrum number(s): 1 2

Current data and model not fit yet.

```

Now we can create fake PIN and GSO data for the planned observation using the `fakeit` command. The result will be simulated spectral files which include the instrumental background, effective area, and resolution:

```

XSPEC12>fakeit
Use counting statistics in creating fake data? (y):
Input optional fake file prefix:
Fake data file name (pin_10mCrab_1Ms.fak):  pin_10mCrab_100ks.fak
Exposure time, correction norm (1.00000e+06, 1.00000): 100000
Fake data file name (gso_10mCrab_100ks.fak): gso_10mCrab_100ks.fak
Exposure time, correction norm (100000., 1.00000): 100000

```

No ARF will be applied to fake spectrum #1 source #1

No ARF will be applied to fake spectrum #2 source #1

2 spectra in use

Chi-Squared = 1037.38 using 768 PHA bins.

Reduced chi-squared = 1.35605 for 765 degrees of freedom

Null hypothesis probability = 1.569217e-10

***Warning: Chi-square may not be valid due to bins with zero variance
in spectrum number(s): 1 2

Current data and model not fit yet.

At this point we have created simulated spectral files for an observation of a 10 mCrab XRB, pin_10mCrab_100ks.fak and gso_10mCrab_100ks.fak. In order to achieve the statistics of an actual observations, these files have to be rebinned to the spectral binning of the regularly created GSO background files. A grouping file which can be used with the FT00L grppha is available from <http://heasarc.gsfc.nasa.gov/docs/suzaku/analysis/gsobgd64bins.dat>:

grppha gso_10mCrab_100ks.fak gso_10mCrab_100ks_bin.fak

MANDATORY KEYWORDS/VALUES

EXTNAME	- SPECTRUM	Name of this BINTABLE
TELESCOP	- SUZAKU	Mission/Satellite name
INSTRUME	- HXD	Instrument/Detector
FILTER	-	Instrument filter in use
EXPOSURE	- 1.00000E+05	Integration time (in secs) of PHA data
AREASCAL	- 1.0000	Area scaling factor
BACKSCAL	- 1.0000	Background scaling factor
BACKFILE	- gso_10mCrab_100ks_bkg.fak	
CORRSCAL	- -1.0000	Correlation scaling factor
CORRFILE	- NONE	Associated correlation file
RESPFILE	- ae_hxd_gsohxnom_20100524.rsp	
ANCRFILE	- NONE	Associated ancillary response file
POISSERR	- TRUE	Whether Poissonian errors apply

CHANTYPE	- PI_SLOW	Whether channels have been corrected
TLMIN1	- 0	First legal Detector channel
DETHANS	- 512	No. of legal detector channels
NCHAN	- 512	No. of detector channels in dataset
PHAVERSN	- 1.1.0	OGIP FITS version number
STAT_ERR	- FALSE	Statistical Error
SYS_ERR	- FALSE	Fractional Systematic Error
QUALITY	- TRUE	Quality Flag
GROUPING	- TRUE	Grouping Flag

```

-----
-----
GRPPHA[] group gsobgd64bins.dat
GRPPHA[] exit
... written the PHA data Extension
..... exiting, changes written to file : gso_10mCrab_100ks_bin.fak
** grppha 3.0.1 completed successfully

```

The same grouping has to be applied to the GSO background spectrum:

```
grppha gso_10mCrab_100ks.bkg gso_10mCrab_100ks_bin.bkg
```

```

-----
MANDATORY KEYWORDS/VALUES
-----
-----

```

EXTNAME	- SPECTRUM	Name of this BINTABLE
TELESCOP	- SUZAKU	Mission/Satellite name
INSTRUME	- HXD	Instrument/Detector
FILTER	-	Instrument filter in use
EXPOSURE	- 1.00000E+05	Integration time (in secs) of PHA data
AREASCAL	- 1.0000	Area scaling factor
BACKSCAL	- 1.0000	Background scaling factor
BACKFILE	- gso_10mCrab_100ks_bkg.bkg	
CORRSCAL	- -1.0000	Correlation scaling factor
CORRFILE	- NONE	Associated correlation file
RESPFILE	- ae_hxd_gsohxnom_20100524.rsp	
ANCRFILE	- NONE	Associated ancillary response file
POISSERR	- TRUE	Whether Poissonian errors apply
CHANTYPE	- PI_SLOW	Whether channels have been corrected
TLMIN1	- 0	First legal Detector channel
DETHANS	- 512	No. of legal detector channels

NCHAN	- 512	No. of detector channels in dataset
PHAVERSN	- 1.1.0	OGIP FITS version number
STAT_ERR	- FALSE	Statistical Error
SYS_ERR	- FALSE	Fractional Systematic Error
QUALITY	- TRUE	Quality Flag
GROUPING	- TRUE	Grouping Flag

```

-----
GRPPHA[group gsobgd64bins.dat] group gsobgd64bins.dat
GRPPHA[exit] exit
... written the PHA data Extension
..... exiting, changes written to file : gso_10mCrab_100ks_bin.bkg
** grppha 3.0.1 completed successfully

```

In the next step we fit these datasets with the Crab-like model defined above. We will use three different background assumptions – low, medium, and high – which vary by as much as 3% and 1.5% for the PIN and the GSO, respectively. This takes into account the fact that the “true” background will likely vary within these limits. We load the simulated source files (rebinned for the GSO). The simulated background files from the first `fakeit` step (rebinned for the GSO) – `pin_10mCrab_1Ms.bkg` and `gso_10mCrab_100ks_bin.bkg` –, are loaded as background files as well as as correction files (“corfiles”), the latter allowing for an easy way to vary the total background within XSPEC.

```
XSPEC12>data pin_10mCrab_100ks.fak gso_10mCrab_100ks_bin.fak
```

```
2 spectra in use
```

```
Spectral Data File: pin_10mCrab_100ks.fak Spectrum 1
```

```
Net count rate (cts/s) for Spectrum:1 4.218e-01 +/- 3.067e-03 (47.2 % total)
```

```
Assigned to Data Group 1 and Plot Group 1
```

```
Noticed Channels: 1-256
```

```
Telescope: SUZAKU Instrument: HXD Channel Type: PI_PIN
```

```
Exposure Time: 1e+05 sec
```

```
Using Background File pin_10mCrab_100ks_bkg.fak
```

```
Background Exposure Time: 1e+06 sec
```

```
Using Response (RMF) File ae_hxd_pinhxnome9_20100731.rsp for Source 1
```

```
Spectral Data File: gso_10mCrab_100ks_bin.fak Spectrum 2
```

```
Net count rate (cts/s) for Spectrum:2 3.820e-01 +/- 2.972e-02 (0.9 % total)
```

```
Assigned to Data Group 1 and Plot Group 2
```

```
Noticed Channels: 1-64
```

```
Telescope: SUZAKU Instrument: HXD Channel Type: PI_SLOW
```



```

Exposure Time: 1e+05 sec
Using Background File          gso_10mCrab_100ks_bkg.fak
Background Exposure Time: 1e+05 sec
Using Response (RMF) File      ae_hxd_gsohxnom_20100524.rsp for Source 1
XSPEC12>back pin_10mCrab_1Ms.bkg gso_10mCrab_100ks_bin.bkg
Net count rate (cts/s) for Spectrum:1  4.212e-01 +/- 3.067e-03 (47.1 % total)
Net count rate (cts/s) for Spectrum:2  3.576e-01 +/- 2.972e-02 (0.8 % total)
XSPEC12>corfile pin_10mCrab_1Ms.bkg gso_10mCrab_100ks_bin.bkg
Net count rate (cts/s) for Spectrum:1  8.936e-01 +/- 3.067e-03 (65.4 % total)
After correction of -4.724e-01 (using cornorm -1.000)
Net correction flux: 0.472407

```

```

Net count rate (cts/s) for Spectrum:2  4.435e+01 +/- 2.972e-02 (50.2 % total)
After correction of -4.399e+01 (using cornorm -1.000)
Net correction flux: 43.9884
XSPEC12>model phabs*powerlaw

```

```

Input parameter value, delta, min, bot, top, and max values for ...
          1          0.001          0          0          100000          1e+06
1:phabs:nH>0.3
          1          0.01          -3          -2           9           10
2:powerlaw:PhoIndex>2.1
          1          0.01           0           0          1e+24          1e+24
3:powerlaw:norm>0.097

```

```

=====
Model phabs<1>*powerlaw<2> Source No.: 1   Active/On
Model Model Component  Parameter  Unit      Value
par  comp
  1    1    phabs      nH          10^22    0.300000    +/- 0.0
  2    2    powerlaw   PhoIndex    2.10000    +/- 0.0
  3    2    powerlaw   norm          9.70000E-02 +/- 0.0
-----

```

```

Chi-Squared = 2.213221e+06 using 320 PHA bins.
Reduced chi-squared = 6981.768 for 317 degrees of freedom
Null hypothesis probability = 0.000000e+00

```

```

***Warning: Chi-square may not be valid due to bins with zero variance
            in spectrum number(s): 1 2

```

Current data and model not fit yet.

We now experiment with different background levels, set by the value of “cornorm”. A value of 0 gives the “normal” background, for example, 0.03 increases it by 3%, and -0.015 decreases it by 1.5%.

```
XSPEC12>cornorm 1-2 0.0
```

```
Spectrum 1 correction norm set to 0
```

```
Spectrum 2 correction norm set to 0
```

```
Chi-Squared =          640.10 using 320 PHA bins.
```

```
Reduced chi-squared =          2.0192 for      317 degrees of freedom
```

```
Null hypothesis probability =    5.004763e-24
```

```
***Warning: Chi-square may not be valid due to bins with zero variance
           in spectrum number(s): 1 2
```

Current data and model not fit yet.

```
XSPEC12>ignore 1:**-12. 70.-** 2:**-42. 600.-**
```

```
32 channels (1-32) ignored in spectrum #      1
```

```
70 channels (187-256) ignored in spectrum #      1
```

```
1 channels (1) ignored in spectrum #      2
```

```
12 channels (53-64) ignored in spectrum #      2
```

```
Chi-Squared =          177.32 using 205 PHA bins.
```

```
Reduced chi-squared =          0.87780 for      202 degrees of freedom
```

```
Null hypothesis probability =    8.940665e-01
```

Current data and model not fit yet.

```
XSPEC12>fit
```

Chi-Squared	Lvl	Par #	1	2	3
171.806	0	1.57021	2.15463	0.115145	

```
=====
```

Variances and Principal Axes

	1	2	3
5.8742E-07	-0.0003	-0.3164	0.9486
6.6987E+01	-1.0000	-0.0056	-0.0022
7.0114E-04	-0.0060	0.9486	0.3164

```
-----
```

```
=====
```

Covariance Matrix

1	2	3
6.698e+01	3.722e-01	1.463e-01
3.722e-01	2.699e-03	1.023e-03
1.463e-01	1.023e-03	3.904e-04

```
=====
Model phabs<1>*powerlaw<2> Source No.: 1 Active/On
Model Model Component Parameter Unit Value
par comp
  1 1 phabs nH 10^22 1.57021 +/- 8.18442
  2 2 powerlaw PhoIndex 2.15463 +/- 5.19538E-02
  3 2 powerlaw norm 0.115145 +/- 1.97593E-02
=====
```

```
Chi-Squared = 171.81 using 205 PHA bins.
Reduced chi-squared = 0.85053 for 202 degrees of freedom
Null hypothesis probability = 9.395170e-01
XSPEC12>cpd /xs
XSPEC12>setplot energy
XSPEC12>plot ldata res
```

This result is shown in Fig. 5.1.

Now we check whether the same source signal would be detectable with a high background, i.e., a 3% and 1.5% higher background for the PIN and the GSO, respectively.

```
XSPEC12>cornorm 1 0.03 2 0.015
Spectrum 1 correction norm set to 0.03
Spectrum 2 correction norm set to 0.015

Chi-Squared = 616.64 using 205 PHA bins.
Reduced chi-squared = 3.0527 for 202 degrees of freedom
Null hypothesis probability = 1.577152e-43
Current data and model not fit yet.
XSPEC12>fit
```

Chi-Squared	Lvl	Par #	1	2	3
569.365	-2	0.770493	2.21249	0.128282	
551.431	-2	4.42397	2.25458	0.147629	
540.304	-2	9.69687	2.29054	0.166809	

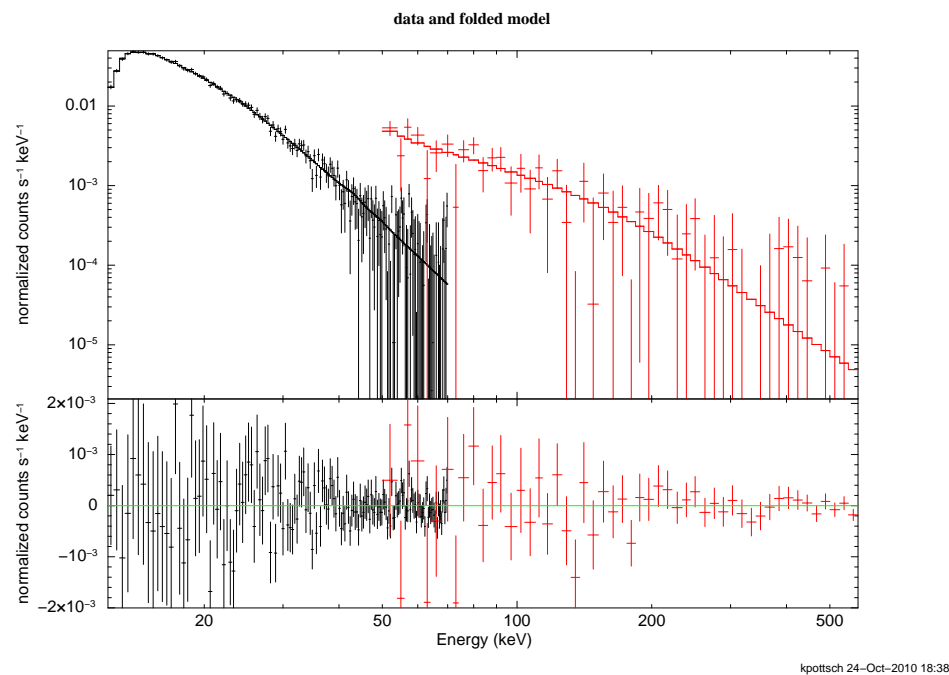


Figure 5.1: Simulation of an HXD observation of a 10 mCrab source with a Crab-like spectrum. Here, the cornorm of the two background files has been set to 0.

<more trials here>				
495.913	-4	61.6134	2.65435	0.558082
495.894	-5	61.4681	2.65265	0.555672
495.894	-3	61.4876	2.65285	0.556031
=====				
Variances and Principal Axes				
	1	2	3	
4.5755E-06	-0.0008	-0.8487	0.5288	
1.1320E+02	-0.9999	-0.0062	-0.0115	
3.2719E-03	-0.0130	0.5288	0.8487	

=====				
Covariance Matrix				
	1	2	3	
1.132e+02	7.006e-01	1.301e+00		
7.006e-01	5.255e-03	9.519e-03		
1.301e+00	9.519e-03	1.731e-02		

```
=====
```

Model phabs<1>*powerlaw<2> Source No.: 1				Active/On	
Model	Model	Component	Parameter	Unit	Value
par	comp				
1	1	phabs	nH	10^22	61.4876 +/- 10.6385
2	2	powerlaw	PhoIndex		2.65285 +/- 7.24926E-02
3	2	powerlaw	norm		0.556031 +/- 0.131566

```
-----
```

Chi-Squared = 495.89 using 205 PHA bins.
 Reduced chi-squared = 2.4549 for 202 degrees of freedom
 Null hypothesis probability = 1.014304e-26
 XSPEC12>plot ldata res

This result is shown in Fig.5.2, and it clear from the figure that in this case the signal is undetectable in the GSO band.

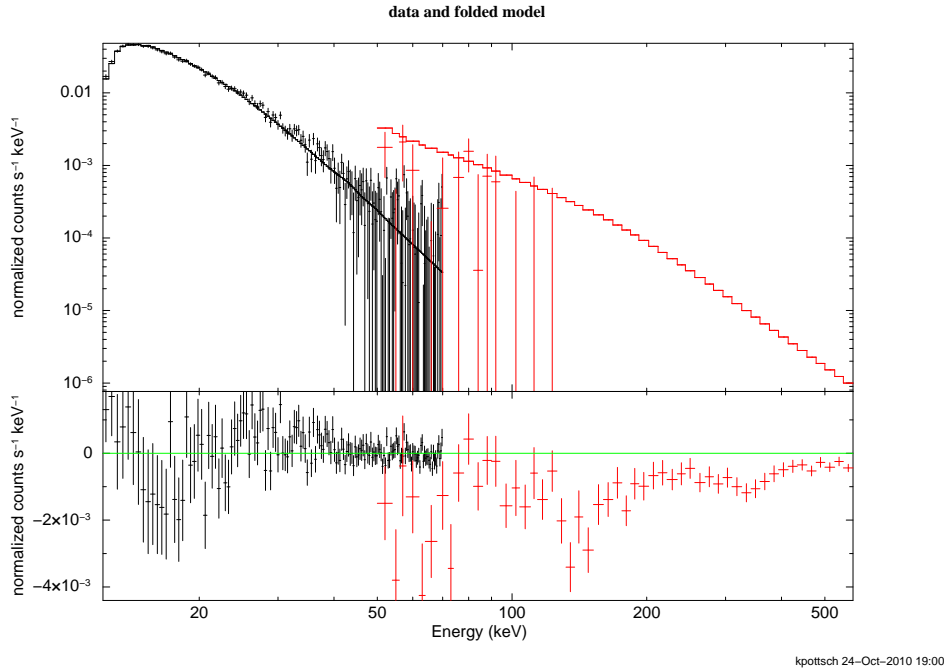


Figure 5.2: Simulation with the highest estimated background, for both the PIN and the GSO.

Finally, we check the source signal using low backgrounds.

XSPEC12>cornorm 1 -0.03 2 -0.015

Spectrum 1 correction norm set to -0.03

Spectrum 2 correction norm set to -0.015

Chi-Squared = 575.81 using 205 PHA bins.

Reduced chi-squared = 2.8505 for 202 degrees of freedom

Null hypothesis probability = 1.270850e-37

Current data and model not fit yet.

XSPEC12>fit

Chi-Squared	Lvl	Par #	1	2	3
514.733	-2	0.0377778	2.05063	0.0865812	
506.924	-1	0.00340908	2.04333	0.0857076	
505.098	-1	0.00113855	2.03811	0.0844117	
<more trials here>					
484.378	-5	0	1.92555	0.0610654	
484.377	-6	0	1.92498	0.0609661	
484.377	3	0	1.92498	0.0609661	

=====
Variances and Principal Axes

	1	2	3
1.6436E-07	-0.0001	-0.1764	0.9843
2.1211E+02	-1.0000	-0.0024	-0.0005
4.7979E-04	-0.0024	0.9843	0.1764

=====
Covariance Matrix

1	2	3
2.121e+02	4.990e-01	1.066e-01
4.990e-01	1.639e-03	3.341e-04
1.066e-01	3.341e-04	6.865e-05

=====
Model phabs<1>*powerlaw<2> Source No.: 1 Active/On
Model Model Component Parameter Unit Value
par comp

1	1	phabs	nH	10 ²²	0.0	+/-	14.5640
2	2	powerlaw	PhoIndex		1.92498	+/-	4.04839E-02
3	2	powerlaw	norm		6.09661E-02	+/-	8.28568E-03

```

Chi-Squared =          484.38 using 205 PHA bins.
Reduced chi-squared =          2.3979 for    202 degrees of freedom
Null hypothesis probability =    3.114375e-25

```

The result is shown in 5.3 where now the GSO spectrum is largely above to model.

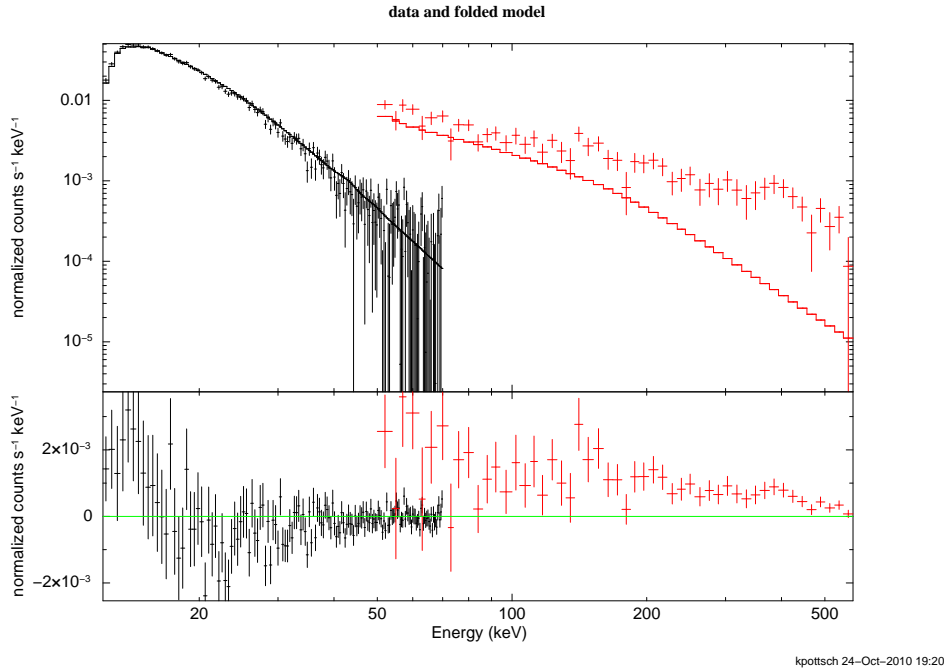


Figure 5.3: Simulation with the lowest estimated background, for both the PIN and the GSO.

By comparing the different fit results from these different runs, the overall uncertainties expected for the slope and normalization can be estimated.

5.6 XISSIM

`xissim` is a *Suzaku* XIS event simulator, based on the tool `xrssim`. It reads a FITS format photon list file, traces photon paths in the telescope (via ray-tracing), and outputs a simulated XIS event file. The XRT thermal shield transmission and the XIS detection efficiency are taken into account if requested. Each record of the photon list file describes the celestial positions, arrival time, and energy of the input photon. The `mkphlist` FT00L can create such photon list files from FITS images (e.g., *ROSAT* HRI or *Chandra* images)

and spectral models (which may be created in `XSPEC`). The `xissim` output event file may be analyzed just like observational data, using standard analysis tools such as `xselect`. `xissim` is part of the latest version of the `FTOOLS`.

5.7 MAKI

MAKI is another web-based interactive tool (see Appendix B) that can determine the orientation of the XIS CCDs on the sky as a function of the observation epoch within the visibility window of the target. For *Suzaku*, the orientation of the solar panels with respect to the spacecraft is fixed, and at the same time, the range of the angles between the vector normal to the solar panels and the vector pointing to the Sun is restricted, which in turn restricts the roll angle of the spacecraft.

When using the tool, general instructions are available via the “Help” button. In order to check the visibility and available roll angles for a target, first load an image. This can be done with either an existing FITS image, or by entering the RA and DEC of the source and clicking the “New Graph” button. This creates an image on which the *Suzaku* XIS field of view (FOV) will be shown.

The “Mission and Roll Selector” (in the upper right of the display) allows different instruments from different missions to be selected. Then the FOV will appear on your image. This can be rotated using the “Roll angle” slider bar.

5.8 RPS

The Remote Proposal Submission (RPS) tool must be used to enter the basic proposal data into the ISAS/JAXA, HEASARC, or ESA database. Proposers should make sure they use the appropriate RPS, since there are multiple reviews. See Appendix B for the list of RPS web-sites and addresses. Two versions of RPS are available: a character-oriented version, where the user submits all the required information via e-mail, or a web-oriented version.

One aspect of RPS that is not immediately obvious is how to specify time-constrained observations. For instance, a need for such an observation may arise for a study of a spectrum of a binary system at a particular orbital phase. If some particular aspect of the observation cannot be clearly specified in the RPS form, the user should detail it in the “comments” field of the RPS form and/or contact either the *Suzaku* team at ISAS/JAXA or the NASA *Suzaku* GOF before submitting.

5.9 Checklist

A successful *Suzaku* proposal, from a technical point of view, must include the following elements:

Coordinates: The PI is responsible for supplying the correct J2000 coordinates. For extended sources, specify single FOVs (coordinates for the center of XIS or the HXD) or rastering parameters (a schematic drawing overlaid on images would be the least ambiguous; equivalent textual descriptions are acceptable).

XIS count rate and exposure time: Explain how they were calculated (for a highly variable source, an added explanation — such as “excluding any bursts” — would be helpful).

HXD count rate and exposure time: If the source is not expected to be a hard X-ray source, this can be set to 0.0 since only the source counts are to be included.

Aimpoint – XIS or HXD : The HXD and XIS aimpoints differ by 3'.5. To get the full effective area for a given instrument, the instrument-specific aimpoint must be chosen (the HXD aimpoint is at (DETX,DETY)=(-3'.5, 0) on the XIS image). The reduction in effective area for the non-selected instrument is $\sim 10\%$.

Observing constraints, if any: These include monitoring, coordinated, phase-dependent, and roll-dependent observations; TOO's are allowed, but the triggering criteria and the probability of triggering must be spelled out in text, and summarized in target remarks.

Note that Guest Observers are welcome to propose for targets already approved for in previous AOs (see the Announcement of Opportunity). However, in the interest of maximizing the scientific return from *Suzaku*, the proposal must explain why the already-approved observation(s) does/do not meet their scientific objectives. Valid reasons include a much longer exposure time, incompatible time constraints, or different positions within an extended source.

We also note that the XISs are subject to count rate limitations, because of possible multiple events in an XIS pixel within one frame (see section 7.9.1). This is much less of a problem than with the ACIS aboard *Chandra*, as *Chandra*'s mirror focuses the X-ray flux onto a CCD area that is orders of magnitude smaller. The rule of thumb is that the XIS can tolerate a point source with a count rate up to ~ 40 cps per CCD with essentially no loss of counts or resolution. For brighter sources, these limitations can be reduced via a variety of XIS modes, such as the use of a sub-array of the XIS, as discussed in section 7.5.

Finally, it is important to remember that because the HXD is a non-imaging detector, contaminating sources in the field of view can significantly affect your results. The HXD

field of view is defined by a collimator with a square opening. The FWHM of the field of view is $34'.4 \times 34'.4$ below ~ 100 keV and $4'.6 \times 4'.6$ above ~ 100 keV. Considering that twice the FWHM value is required to completely eliminate the contamination in a collimator-type detector, and the source may happen to be located at the diagonal of the square, nearby bright sources within a radius of $50'$ and $6'.5$ from the aim point can contaminate the data in the energy band below and above ~ 100 keV, respectively. If you specify the roll-angle to avoid the source, the limit will be reduced to $\sim 35'$ and $\sim 4'.6$, respectively. It is the proposer's responsibility to show that any source with a flux level comparable to or brighter than that of the target of interest does not exist within these ranges. The proposer can, e.g., check this by using the hard X-ray source catalogs from such satellites as *RXTE*-ASM, *INTEGRAL*, and *Swift*, among others.

5.10 Additional Requirements for US Proposers

There are two additional NASA-specific proposal rules that must be followed by US-based proposers:

1. Proposals to NASA must be submitted through **ARK/RPS**. The user interface of **ARK/RPS** is similar to that of the "classic" **RPS** except that the PI must first create an **ARK** account and/or join the *SuzakuRPS* group. Having done so, the *SuzakuRPS* form can be accessed via **ARK/RPS**.
2. The estimated level of effort (in FTEs) of any NASA civil servants among the team (PI or Co-Is) must be entered into the **ARK/RPS** form. Enter 0 if no NASA civil servant is part of the team.

Chapter 6

X-Ray Telescopes (XRT)

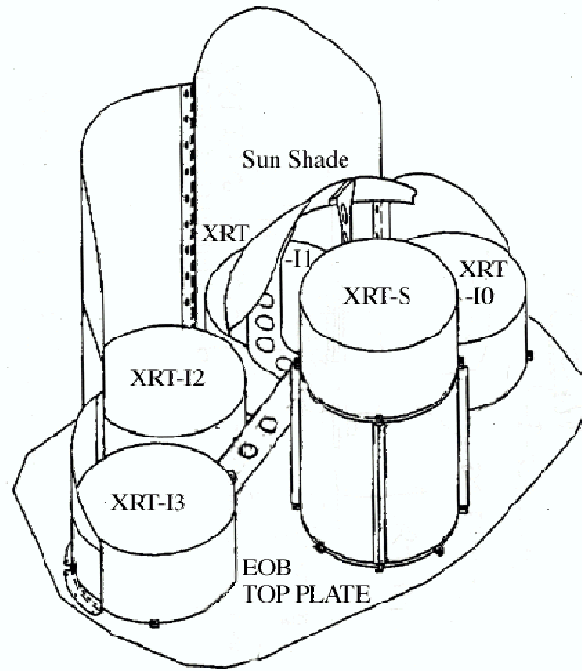
Suzaku has five light-weight thin-foil X-Ray Telescopes (XRTs). The XRTs have been developed jointly by NASA/GSFC, Nagoya University, Tokyo Metropolitan University, and ISAS/JAXA. These are grazing-incidence reflective optics consisting of compactly nested, thin conical elements. Because of the reflectors' small thickness, they permit high density nesting and thus provide large collecting efficiency with a moderate imaging capability in the energy range of 0.2–12 keV, all accomplished in telescope units under 20 kg each.

Four XRTs on-board *Suzaku* are used for the XIS (XRT-I), and the remaining XRT is for the XRS (XRT-S). XRT-S is no longer functional. The XRTs are arranged on the Extensible Optical Bench (EOB) on the spacecraft in the manner shown in Fig. 6.1. The external dimensions of the 4 XRT-I's are the same (see Table 6.1, which also includes a comparison with the ASCA telescopes).

The angular resolutions of the XRTs range from $1'8''$ to $2'3''$, expressed in terms of half-power diameter, which is the diameter within which half of the focused X-rays are enclosed. The angular resolution does not significantly depend on the energy of the incident X-rays in the energy range of *Suzaku*, 0.2–12 keV. The effective areas are typically 440 cm^2 at 1.5 keV and 250 cm^2 at 8 keV. The focal length of the XRT-I is 4.75 m. Actual focal lengths of the individual XRT quadrants deviate from the design values by a few cm. The optical axes of the quadrants of each XRT are aligned to within $2'$ from the mechanical axis. The field of view for the XRT-I's is about $17'$ at 1.5 keV and $13'$ at 8 keV (see also Table 3.1).

6.1 Basic XRT Components

The *Suzaku* X-Ray Telescopes (XRTs) consist of closely nested thin-foil reflectors, reflecting X-ray at small grazing angles. An XRT is a cylindrical structure, having the following layered components: 1. a thermal shield at the entrance aperture to help maintain a uniform temperature, 2. a pre-collimator mounted on metal rings for stray light elimination,


 Figure 6.1: Layout of the XRTs on the *Suzaku* spacecraft.

	<i>Suzaku</i> XRT-I	ASCA
Number of telescopes	4	4
Focal length	4.75 m	3.5 m
Inner diameter	118 mm	120 mm
Outer diameter	399 mm	345 mm
Height	279 mm	220 mm
Mass per telescope	19.5 kg	9.8 kg
Number of nested shells	175	120
Reflectors per telescope	1400	960
Geometric area per telescope	873 cm ²	558 cm ²
Reflecting surface	gold	gold
Substrate material	aluminum	aluminum
Substrate thickness	155 μ m	127 μ m
Reflector slant height	101.6 mm	101.6 mm

Table 6.1: Telescope dimensions and parameters of XRT-I.



Figure 6.2: A *Suzaku* X-ray telescope.

3. a primary stage for the first X-ray reflection, 4. a secondary stage for the second X-ray reflection, 5. a base ring for structural integrity and interfacing with the EOB of the spacecraft. All these components, except the base rings, are constructed in 90° segments. Four of these quadrants are coupled together by interconnect-couplers and also by the top and base rings (Fig. 6.2). The telescope housings are made of aluminum for an optimal strength to mass ratio. Each reflector consists of a substrate also made of aluminum and an epoxy layer that couples the reflecting gold surface to the substrate.

Including the alignment bars, collimating pieces, screws and washers, couplers, retaining plates, housing panels and rings, each XRT-I consists of over 4112 mechanically separated parts. In total, nearly 7000 qualified reflectors were used and over 1 million cm^2 of gold surface was coated.

6.1.1 Reflectors

In shape, each reflector is a 90° segment of a section of a cone. The cone angle is designed to be the angle of on-axis incidence for the primary stage and 3 times that for the secondary

stage. They are 101.6 mm in slant length, with radii extending approximately from 60 mm at the inner part to 200 mm at the outer part. The reflectors are nominally $178\text{ }\mu\text{m}$ in thickness. All reflectors are positioned with grooved alignment bars, which hold the foils at their circular edges. There are 13 alignment bars at the face of each quadrant, separated by $\sim 6.4^\circ$.

To properly reflect and focus X-ray at grazing incidence, the precision of the reflector figure and the smoothness of the reflector surface are important aspects. Since polishing of thin reflectors is both impractical and expensive, reflectors in *Suzaku* XRTs acquire their surface smoothness by a replication technique and their shape by thermo-forming of aluminum. In the replication method, metallic gold is deposited on an extrusion glass mandrel (“replication mandrel”), the surface of which has sub-nanometer smoothness over a wide spatial frequency, and the substrate is subsequently bonded with the metallic film with a layer of epoxy. After the epoxy is hardened, the substrate-epoxy-gold film composite can be removed from the glass mandrel and the replica acquires the smoothness of the glass. The replica typically has $\sim 0.5\text{ nm}$ rms roughness at mm or smaller spatial scales, which is sufficient for excellent reflectivity at incident angles less than the critical angle. The *Suzaku* XRTs are designed with on-axis reflection at less than the critical angle, which is approximately inversely proportional to X-ray energy.

In the thermo-forming of the substrate, pre-cut, mechanically rolled aluminum foils are pressed onto a precisely shaped “forming mandrel”, which is not the same as the replication mandrel. The combination is then heated until the aluminum softens. The aluminum foils acquire the shape of the properly shaped mandrel after cooling and release of pressure. In the *Suzaku* XRTs, the conical approximation of the Wolter-I type geometry is used. This approximation fundamentally limits the angular resolution achievable. More significantly, the combination of the shape error in the replication mandrels and the imperfection in the thermo-forming process (to about $4\text{ }\mu\text{m}$ in the low frequency components of the shape error in the axial direction) limits the angular resolution to about $1'$.

6.1.2 Pre-Collimator

The pre-collimator, which blocks stray light that otherwise would enter the detector at a larger angle than intended, consists of concentrically nested aluminum foils, similar to those of the reflector substrates. They are shorter, 22 mm in length, and thinner, $120\text{ }\mu\text{m}$ in thickness. They are positioned in a fashion similar to that of the reflectors, by 13 grooved aluminum plates at each circular edge of the pieces. They are installed on top of their respective primary reflectors along the axial direction. Due to their smaller thickness, they do not significantly reduce the entrance aperture in that direction more than the reflectors already do. Pre-collimator foils do not have reflective surfaces (neither front nor back). The relevant dimensions are listed in Table 6.2.

	XRT-I
Number of collimators	4
Height	32 mm
Blade substrate	aluminum
Blade thickness	120 μm
Blade height	22 mm
Height from blade top to reflector top	30 mm
Number of nested shells	175
Blades per telescope	700
Mass per collimator	2.7 kg

Table 6.2: Design parameters for the pre-collimator.

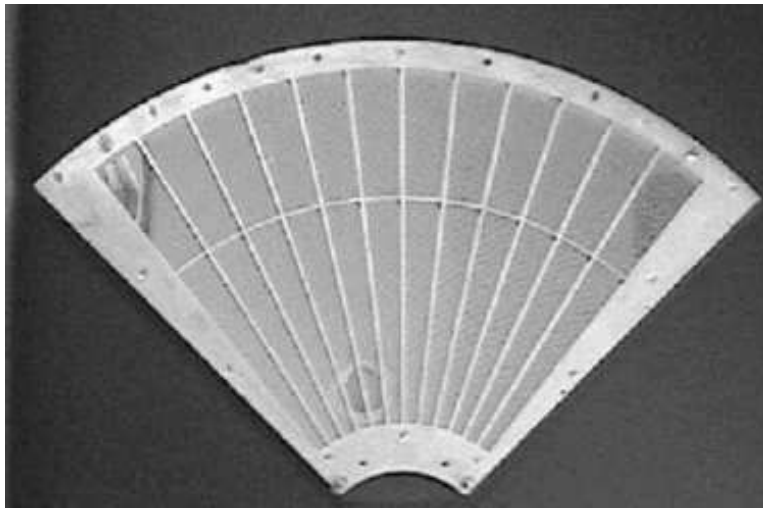


Figure 6.3: A thermal shield.

6.1.3 Thermal Shields

The *Suzaku* XRTs are designed to function in a thermal environment of $20 \pm 7.5^\circ\text{C}$. The reflectors, due to their composite nature and thus their mismatch in coefficients of thermal expansion, suffer from thermal distortion that degrades the angular resolution of the telescopes for temperatures outside this range. Thermal gradients also distort the telescope on a larger scale. Even though sun shields and other heating elements on the spacecraft help in maintaining a reasonable thermal environment, thermal shields are integrated on top of the pre-collimator stage to provide the needed thermal control.

6.2 In-Flight Performance

In this section we describe the in-flight performance and calibration of the *Suzaku* XRTs. There are no data to verify the in-flight performance of the XRT-S, therefore we hereafter concentrate on the four XRT-I modules (XRT-I0 through I3) which focus incident X-rays on the XIS detectors. Several updates of the XRT-related calibration were made in July 2008.

6.2.1 Focal Positions

A point-like source, MCG-6-30-15, was observed at the XIS aimpoint during 2005 August 17-18. Fig. 6.4 shows the focal position of the XRT-I_s, that the source is found at on the XISs, when the satellite points at it using the XIS aimpoint. The focal positions are located close to the detector center with a deviation of 0.3 mm from each other. This implies that the fields of view of the XISs coincide to within $\sim 0'.3$.

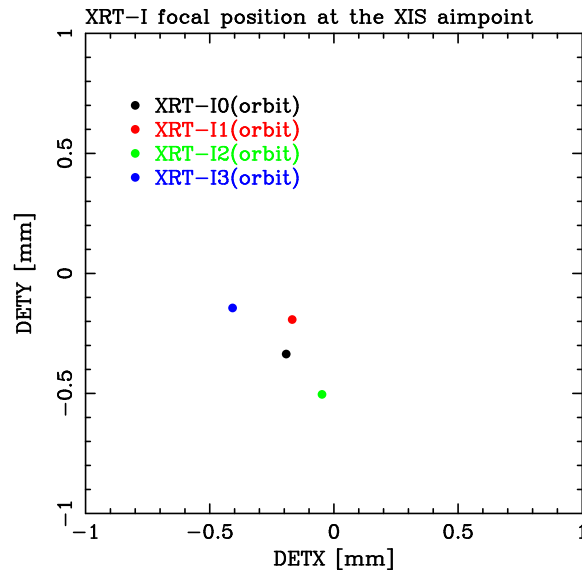


Figure 6.4: Focal positions on the XISs when the satellite points at MCG-6-30-15 using the XIS aimpoint.

6.2.2 Optical Axis

The maximum transmission of each telescope module is achieved when a target star is observed along the optical axis. The optical axes of the four XRT-I modules are, however, expected to scatter in an angular range of $\sim 1'$. Accordingly, we have to define the axis

to be used for real observations that provides a reasonable compromise among the four optical axes. We hereafter refer to this axis as the observation axis.

In order to determine the observation axis, we have first searched for the optical axis of each XRT-I module by observing the Crab nebula at various off-axis angles. The observations of the Crab nebula were carried out in 2005 and 2006. Hereafter all the off-axis angles are expressed in the detector coordinate system DETX/DETY (see <ftp://legacy.gsfc.nasa.gov/suzaku/doc/xis/suzakumemo-2006-39.pdf>).

By fitting a model comprising of a Gaussian plus a constant to the count rate data as a function of the off-axis angle, we have determined the optical axis of each XRT-I module. The result is shown in Fig. 6.5.

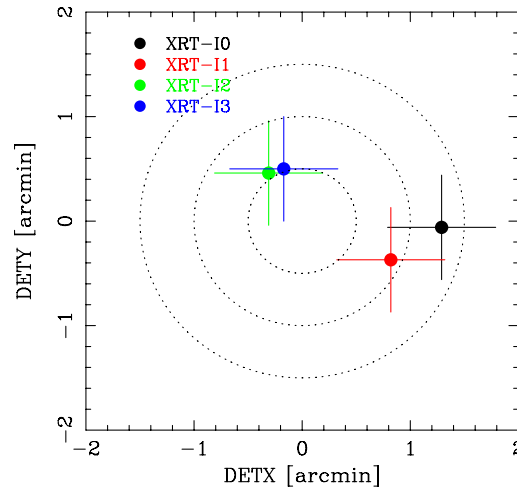


Figure 6.5: Locations of the optical axis of each XRT-I module in the focal plane determined from the observations of the Crab nebula in 2005 August–September. This figure implies that the image on each XIS detector becomes brightest when a target star is placed at the position of the corresponding cross. The dotted circles are drawn every $30''$ in radius from the XIS-default position (see text).

Since the optical axes moderately scatter around the origin, we have decided to adopt it as the default observation axis for XIS-oriented observations. Hereafter we refer to this axis as the XIS-default orientation, or equivalently, the XIS-default position. The optical axis of the XRT-I0 shows the largest deviation of $\sim 1.3'$ from the XIS-default position. Nevertheless, the efficiency of the XRT-I0 at the XIS-default position is more than 97%, even at 8–10 keV, the highest energy band (see Fig. 6.10). The optical axis of the HXD PIN detector, on the other hand, deviates from this default by $\sim 5'$ in the negative DETX direction (see for example, the instrument paper at <ftp://legacy.gsfc.nasa.gov/suzaku/doc/hxd/suzakumemo-2006-37.pdf>). Because of

this, the observation efficiency of the HXD PIN at the XIS-default orientation is reduced to $\sim 93\%$ of the on-axis value. We thus provide another default pointing position, the HXD-default position, for HXD-oriented observations, at $(-3'5, 0')$ in DETX/DETY coordinates. At the HXD-default position, the efficiency of the HXD PIN is nearly 100%, whereas that of the XIS is $\sim 88\%$ on average.

6.2.3 Effective Area

In-flight calibration of the effective area has been carried out with version 2.1 processed data of the Crab nebula both at the XIS- and HXD-default positions. The observations were carried out in 2005 September 15–16. The data were taken in the normal mode with the 0.1 s burst option in which the CCD is exposed during 0.1 s out of the full-frame read-out time of 8 s, in order to avoid the event pile-up and the telemetry saturation. The exposure time of 0.1 s is, however, comparable to the frame transfer time of 0.025 s. As a matter of fact, the Crab image is elongated in the frame-transfer direction due to so-called the out-of-time events, as shown in Fig. 6.6.

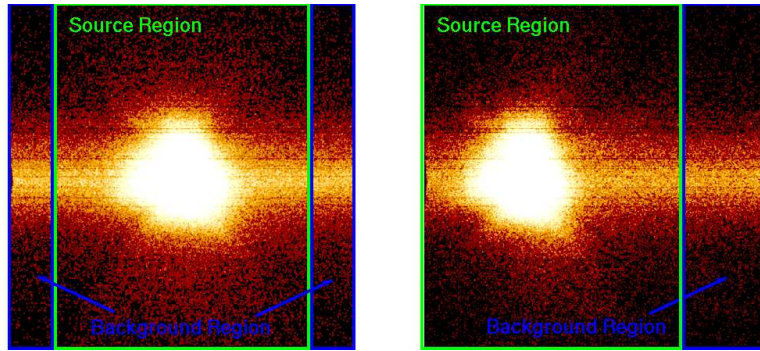


Figure 6.6: The source- and background-integration regions overlaid on the Crab images taken with XIS1 at the XIS-default position (left) and the HXD-default position (right) on 2005 September 15–16. The images are elongated in the frame-transfer direction due to the out-of-time events (see text). In order to cancel these events, the background regions with a size of 126 by 1024 pixels each are taken at the left and right ends of the chip for the XIS-default position, and a single region with a size of 252 by 1024 pixels is taken at the side far from the Crab image for the HXD-default position. The remaining source-integration region has a size of 768 by 1024 pixels, or $13'3 \times 17'8$. The background subtraction is carried out after area-size correction.

Accordingly, the background-integration regions with a size of 126 by 1024 pixels are taken at the left and right ends of the chip for the XIS-default position, perpendicularly

to the frame-transfer direction, as shown in the left panel of Fig. 6.6. For the observation at the HXD-default position, the image center is shifted from the XIS-default position in the direction perpendicular to the frame-transfer direction for XIS0 and XIS3. Hence we can adopt the same background-integration regions as those of the XIS-default position for these two XIS modules. For XIS1 and XIS2, on the other hand, the image shift occurs in the frame-transfer direction, as shown in the right panel of Fig. 6.6. We thus take a single background-integration region with a size of 252 by 1024 pixels at the far side from the Crab image for the HXD-default position of these two detectors. As a result, the remaining source-integration region has a size of 768 by 1024 pixels, or $13'.3 \times 17'.8$ for all the cases, which is wide enough to collect all the photons from the Crab nebula.

After subtracting the background, taking into account the sizes of the regions, we have fitted the spectra taken with the four XIS modules with a model composed of a power law undergoing photoelectric absorption using `xspec` Version 11.2. For the photoelectric absorption, we have adopted the model `phabs` with the cosmic metal abundances of Anders & Grevesse (1989, *Geochim. Cosmochim. Acta*, 53, 197). First, we let all parameters vary independently for all the XIS modules. The results are summarized for the XIS/HXD nominal positions separately in Table 6.3 and are shown in Fig. 6.7.

Table 6.3: Best-fit parameters of the power law model fits to the Crab spectra taken on 2005 September 15–16.

Sensor ID	N_{H}	Photon Index	Normalization	Flux	χ^2_{ν} (d.o.f.)
XIS-default position					
XIS0	0.311 ± 0.015	2.077 ± 0.017	$9.38^{+0.24}_{-0.23}$	2.086	1.02 (89)
XIS1	0.294 ± 0.014	2.085 ± 0.017	$9.73^{+0.23}_{-0.22}$	2.141	1.59 (89)
XIS2	0.282 ± 0.015	2.065 ± 0.017	$9.29^{+0.23}_{-0.22}$	2.134	1.34 (89)
XIS3	0.304 ± 0.015	2.082 ± 0.017	$9.33^{+0.24}_{-0.23}$	2.062	1.34 (89)
PIN	0.3 (fix)	2.101 ± 0.008	11.41 ± 0.26	2.464	0.74 (72)
HXD-default position					
XIS0	0.304 ± 0.018	2.079 ± 0.021	$9.13^{+0.27}_{-0.26}$	2.025	1.28 (89)
XIS1	0.295 ± 0.016	2.111 ± 0.021	$9.59^{+0.27}_{-0.26}$	2.030	0.86 (89)
XIS2	0.282 ± 0.016	2.070 ± 0.019	$9.54^{+0.26}_{-0.25}$	2.151	1.22 (89)
XIS3	$0.301^{+0.017}_{-0.016}$	2.085 ± 0.019	9.29 ± 0.25	2.043	1.19 (89)
PIN	0.3 (fix)	2.090 ± 0.009	10.93 ± 0.27	2.400	0.82 (72)

N_{H} : Hydrogen column density in 10^{22} cm^{-2} .

Normalization: Power-law normalization in photons $\text{cm}^{-2}\text{s}^{-1}\text{keV}^{-1}$ at 1 keV.

Flux: Energy flux in $10^{-8} \text{ cm}^{-2}\text{s}^{-1}$ in the 2–10 keV band.

For the fit, we have adopted the ARFs and RMFs generated using CALDB 2008-07-09. These ARFs are made for a point source, whereas the Crab nebula is slightly extended ($\sim 2'$). We thus have created ARFs by utilizing the ray-tracing simulator (Misaki et al. 2005, *Appl. Opt.*, 44, 916) with a *Chandra* image as input, and have

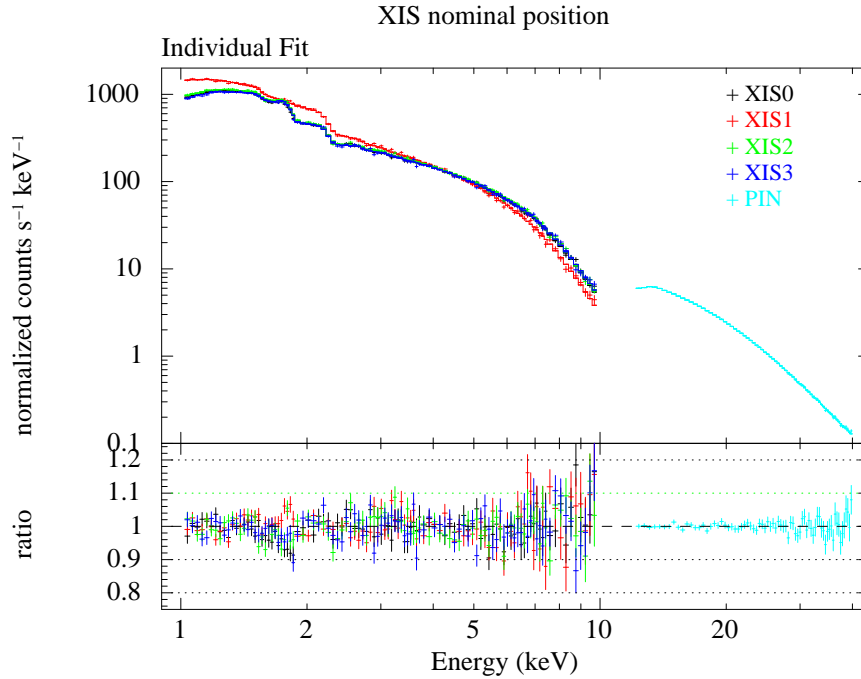


Figure 6.7: Power-law fit to the Crab spectra of all four XIS modules taken at the XIS-default position. All the parameters are allowed to vary independently for each XIS module. The fit is carried out in the 1.0–10.0 keV band, excluding the 1.5–2.0 keV interval where large systematic uncertainties associated with the Si K-edge remain. This energy range is retrieved after the fit.

confirmed that the difference of the effective area between these two sets of ARFs is less than 1%. We have neglected the energy channels below 1 keV, above 10 keV, and in the 1.5–2.0 keV band because of insufficient calibration related to uncertainties of the nature and amount of the contaminant on the OBF and to the Si edge structure (see <ftp://legacy.gsfc.nasa.gov/suzaku/doc/hxd/suzakumemo-2006-35.pdf>). Data in the 1.5–2.0 keV range are retrieved after the fit and shown in Fig. 6.7.

Toor & Seward (1974, AJ, 79, 995) compiled the results from a number of rocket and balloon measurements available at that time, and derived the photon index and the normalization of the power law of the Crab nebula to be 2.10 ± 0.03 and $9.7 \text{ photons cm}^{-2} \text{ s}^{-1} \text{ keV}^{-1}$ at 1 keV, respectively. Overlaying photoelectric absorption with $N_{\text{H}} = 3 \times 10^{21} \text{ cm}^{-2}$, we obtain the flux to be $2.1 \times 10^{-8} \text{ erg cm}^{-2} \text{ s}^{-1}$ in the 2–10 keV band. The best-fit parameters of all the XIS modules at the XIS- and HXD-default positions are close to these standard values.

Since the best-fit parameters of the four XIS modules are close to the standard values,

we have attempted to constrain the photon index to be the same for all the detectors. The best-fit parameters are summarized in Table 6.4.

Table 6.4: Best-fit parameters of the contemporaneous power-law fits to the Crab spectra taken in 2005 September 15–16.

Sensor ID	N_H	Photon Index	Normalization	Flux	χ^2_ν (d.o.f.)
XIS-default position					
XIS0	0.321 ± 0.009	2.090 ± 0.006	9.55 ± 0.10	2.080	1.24 (432)
XIS1	0.298 ± 0.008		9.79 ± 0.10	2.14	
XIS2	0.302 ± 0.008		9.72 ± 0.10	2.13	
XIS3	0.311 ± 0.009		9.43 ± 0.10	2.06	
PIN	0.3 (fix)		11.06 ± 0.11	2.42	
HXD-default position					
XIS0	0.307 ± 0.011	2.086 ± 0.007	$9.19^{+0.12}_{-0.11}$	2.019	1.13 (432)
XIS1	0.277 ± 0.009		9.28 ± 0.11	2.11	
XIS2	0.298 ± 0.010		9.74 ± 0.11	2.21	
XIS3	0.300 ± 0.010		9.28 ± 0.15	2.11	
PIN	0.3 (fix)		10.80 ± 0.01	2.45	

N_H : Hydrogen column density in 10^{22} cm^{-2} .

Normalization : Power-law normalization in photons $\text{cm}^{-2} \text{s}^{-1} \text{keV}^{-1}$ at 1 keV.

Flux : Energy flux in $10^{-8} \text{ cm}^{-2} \text{s}^{-1}$ in the 2–10 keV band.

The hydrogen column density $(0.28\text{--}0.32) \times 10^{22} \text{ cm}^{-2}$ and the photon index 2.09 ± 0.01 are consistent with the standard values.

6.2.4 Vignetting

The vignetting curves calculated by the ray-tracing simulator are compared with the observed intensities of the Crab nebula at various off-axis angles in Figs. 6.8–6.10.

We have utilized the data of the Crab nebula taken during 2005 August and 2006 August. In the figures, we have drawn the vignetting curves for the energy bands 2–10 keV, 3–6 keV and 8–10 keV. To obtain this, we first assume the spectral parameters of the Crab nebula to be a power law with $N_H = 0.33 \times 10^{22} \text{ cm}^{-2}$, photon index=2.09, and normalization=9.845 photons $\text{cm}^{-2} \text{s}^{-1} \text{keV}^{-1}$ at 1 keV. These values are the averages of the four detectors at the XIS-default position (Table 6.4). We then calculate the count rate of the Crab nebula on the entire CCD field of view in 0.5 steps in both the DETX and DETY directions using the ray-tracing simulator. Note that the abrupt drop of the model curves at $\sim 8'$ is due to the source approaching the detector edge. On the other hand, the data points provide the real count rates in the corresponding energy bands within an aperture of $13.3'$ by $17.8'$. Note that the aperture adopted for the observed data

can collect more than 99% of the photons from the Crab nebula, and hence the difference of the integration regions between the simulation and the observation does not matter. Finally, we re-normalize both the simulated curves and the data so that the count rate of the simulated curves at the origin becomes equal to unity.

These figures roughly show that the effective area is calibrated within $\sim 5\%$ over the XIS field of view, except for the 8–10 keV band of XIS1. The excess of these XIS1 data points at the XIS-default position has already been seen in Fig. 6.7 (see also Table 6.3).

6.2.5 Angular Resolution

As shown in Serlemitsos et al. (2007), verification of the imaging capability of the XRTs has been made with the data of SS Cyg in quiescence taken on 2005 November 2 01:02UT–23:39UT. The total exposure time was 41.3 ks. SS Cyg is selected for this purpose because it is a point source and moderately bright (3.6, 5.9, 3.7, and 3.5 counts s^{-1} for XIS0 through XIS3), and hence, it is not necessary to care about pile-up even at the image core. In Fig. 6.11, we give the images of all the XRT-I modules thus obtained. The HPD is obtained to be $1'8$, $2'3$, $2'0$, and $2'0$ for XRT-I0, 1, 2, and 3, respectively.

In Fig. 6.11, we also show corresponding images produced by the updated “new” simulator `xissim` (version 2008-04-05). The simulator has been tuned for each quadrant. Therefore, the simulated images look different from quadrant to quadrant. More local or spiky structures seen in the observed images, however, are not reproduced.

In Fig. 6.12, we show Point Spread Functions (PSFs) using the data shown in Fig. 6.11 before smoothing. Note that the core shape within $0'2$ is not tuned at all. The core broadening is mainly due to the attitude error of the satellite control (Uchiyama et al. 2007). In Fig. 6.13, we show encircled energy functions (EEFs). The reproducibility of the EEF is important when extracting spectra from a circular region with a given radius. In the new simulator, the EEF of the simulations coincides with that of the observed data to within 4% for radii from $1'$ to $6'$.

6.2.6 Stray Light

Studies of the stray light were carried out with Crab nebula off-axis pointings during 2005 August 22 – September 16 for a range of off-axis angles. An example of a stray light image is shown in the right panel of Fig. 6.14.

This image is taken with the XIS3 in the 2.5–5.5 keV band with the Crab nebula offset at $(-20', 0')$ in (DETX, DETY). The left and central panels show simulated stray light images without and with the pre-collimator, respectively, of a monochromatic point source of 4.5 keV being located at the same off-axis angle. The ghost image seen in the left half of the field of view is due to “secondary reflection”. Although “secondary reflection” cannot completely be diminished at the off-axis angle of $20'$, the center of the field of view is

nearly free of stray light. The semi-circular bright region in the middle panel, starting at $(\text{DETX}, \text{DETY}) = (-8''.9, +6''.5)$, running through $\sim(0', 0')$, where the image becomes fainter, and ending up at $(-8'.9, -6'.5)$, originates from the innermost secondary reflector, because the space between the innermost reflector and the inner wall of the telescope housing is much larger than the reflector-reflector separation. This semi-circular bright region is only marginally visible in the real Crab nebula image in the right panel. Another remarkable difference between the simulation and the real observation is the location of the brightest area; in the simulation, the left end of the image ($\text{DETX} \lesssim -7'.5$, $|\text{DETY}| \lesssim 3'$) is relatively dark whereas the corresponding part is brightest in the Crab nebula image. These differences originate from relative alignments among the primary and secondary reflectors, and the blades of the pre-collimator, which are to be calibrated by referring to the data of the stray light observations in the near future.

Overall, in-flight stray light observations of the Crab were carried out with off-axis angles of $20'$ (4 pointings), $50'$ (4 pointing) and $120'$ (4 pointing) in 2005 August and September. Figure 6.15 shows the measured and simulated angular responses of the XRT-I at 1.5 and 4.5 keV up to 2° . The effective area is normalized to 1 at the on-axis position. The integration area corresponds to the detector size of the XIS ($17'.8 \times 17'.8$). The plots are necessary to plan observations of diffuse sources or faint emissions near bright sources, such as outskirts of cluster of galaxies, diffuse objects in the Galactic plane, SN 1987A, etc.. The four solid lines in the plots correspond to raytracing simulations for the different detectors, while the crosses are the normalized effective area using the Crab pointings. For example, the effective area of the stray light at 1.5 keV is $\sim 10^{-3}$ at off-axis angles smaller than $70'$ and $< 10^{-3}$ at off-axis angles larger than $70'$. The measured stray light flux is in agreement with that of the simulations to within an order of magnitude. The solution of the solid lines is incorporated into the `xissim` and the `xissimarfigen` tools using CALDB 2008-06-02.

For feasibility studies of XIS data analyses of faint objects near bright sources, proposers are encouraged to simulate observations using `xissim` in order to determine whether the stray light flux might dominate that of the faint object or not. Proposers who do observe a target heavily suffering from stray light contamination need to handle the data with special care regarding calibration errors. Faint objects in the Galactic center and plane often suffer from stray light contamination from bright X-ray stars, and the flux of the outskirts of galaxy clusters, widely extended over the detector field of view, is sometimes dominated by stray light from the bright core.

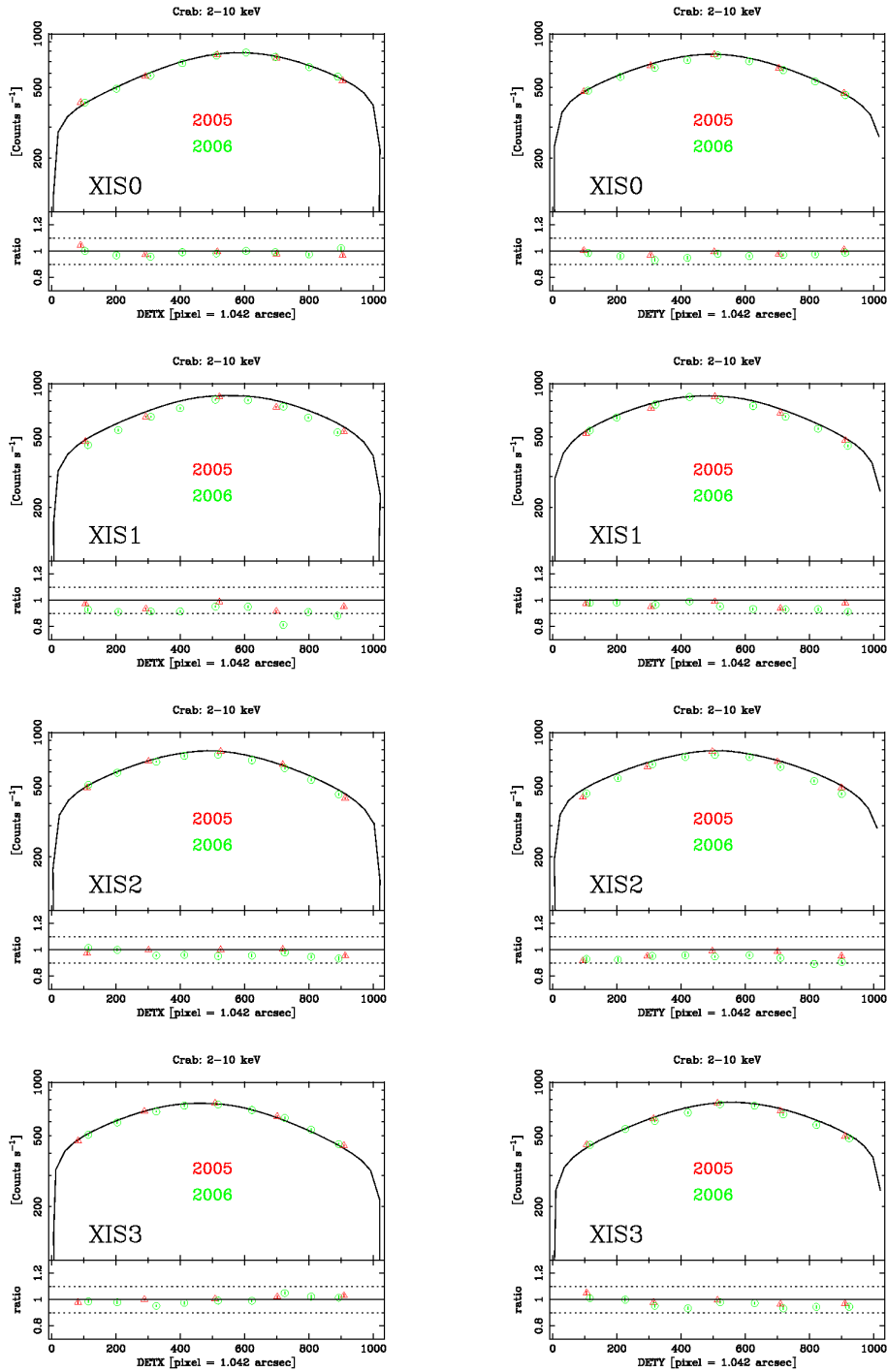


Figure 6.8: Count rates of the Crab pointings offset in DETX (left) and DETY (right) in the 2–10 keV band. Red and green symbols correspond to the data during 2005 and 2006, respectively. The solid line corresponds to the output of the ray-tracing simulator `xissim`. The bottom panels show the ratios of the data to the simulator output.

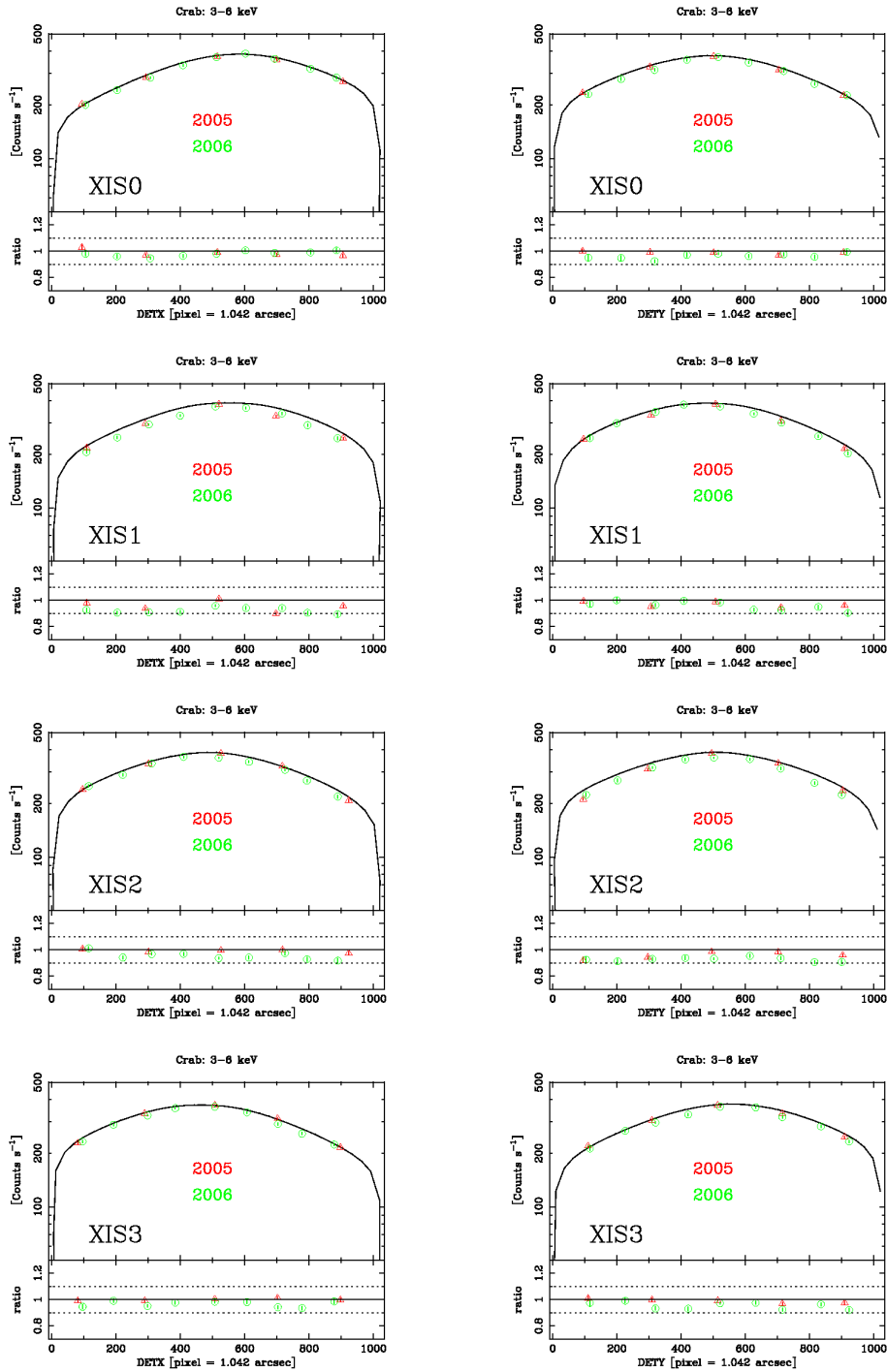


Figure 6.9: The same as Fig.6.8 but in the 3-6 keV band.

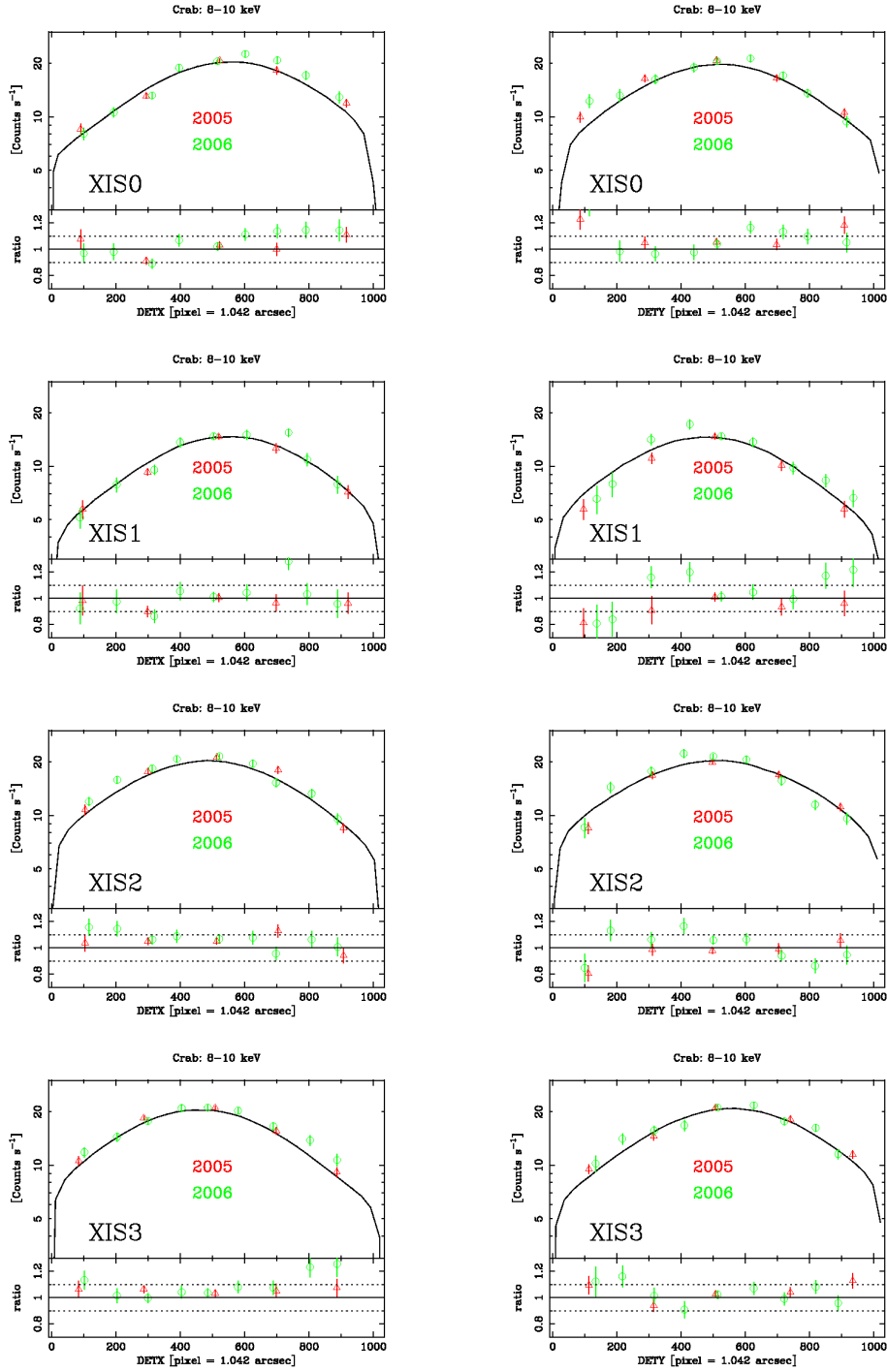


Figure 6.10: The same as Fig.6.8 but in the 8–10 keV band.

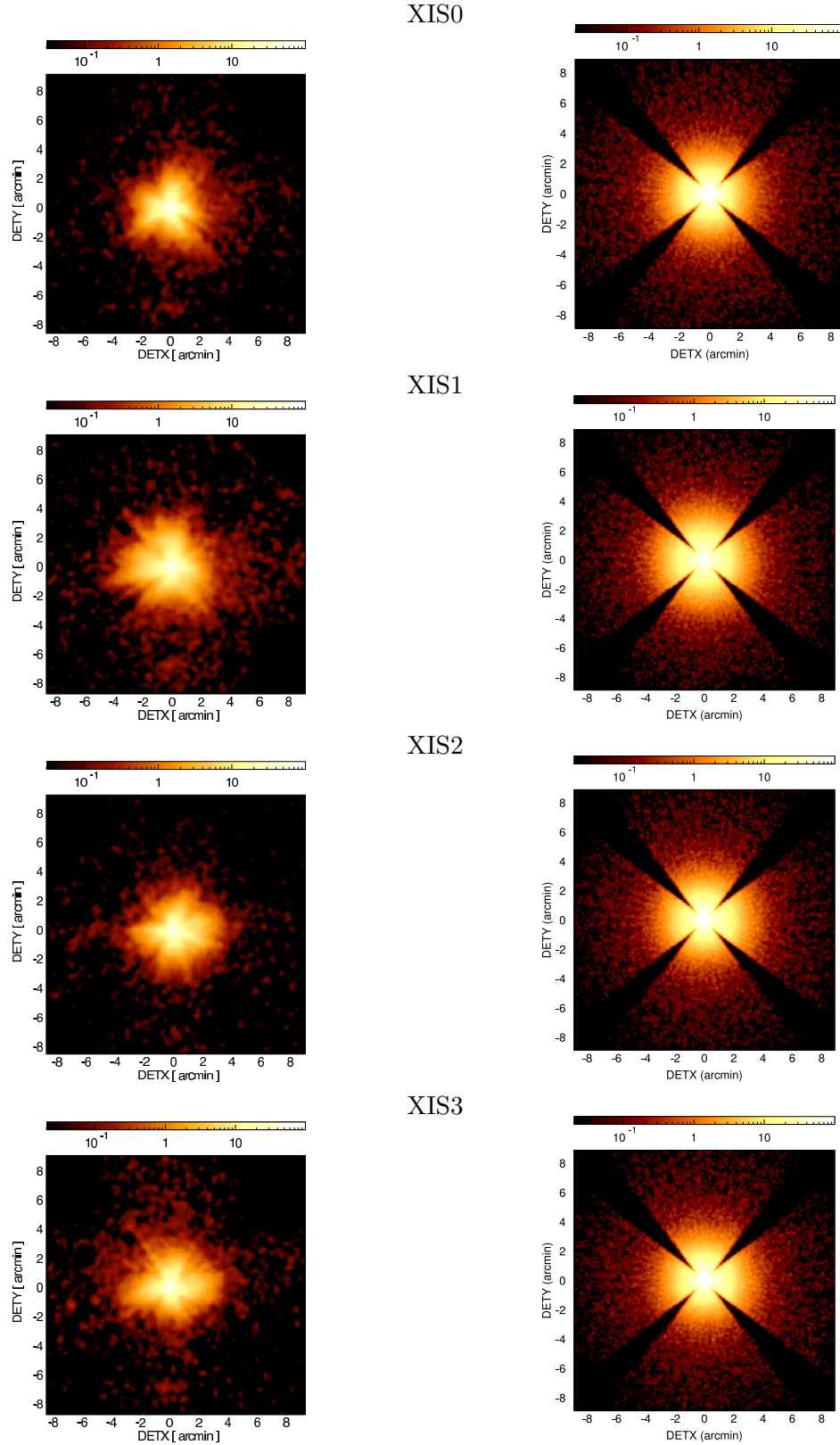


Figure 6.11: Images of the four XRT-I modules in the focal plane: SS Cyg (left) and simulation (right). All the images are binned to 2×2 pixels and then smoothed with a Gaussian with a sigma of 3 pixels, where the pixel size is $24 \mu\text{m}$. The Fe55 events were removed from the SS Cyg image.

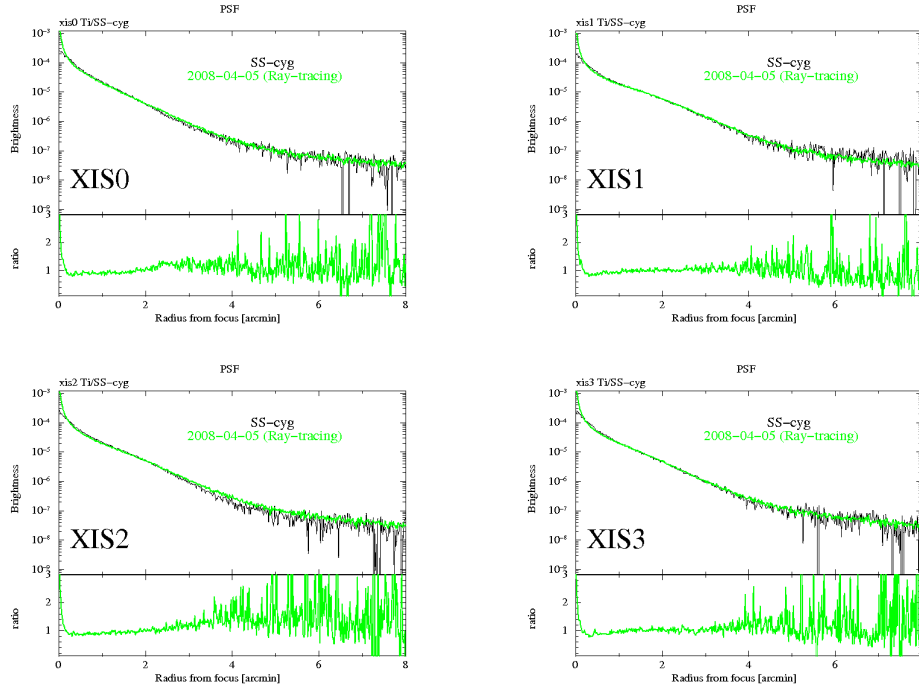


Figure 6.12: PSF of the four XRT-I images. The lower panels show the ratio between the observed and simulated data.

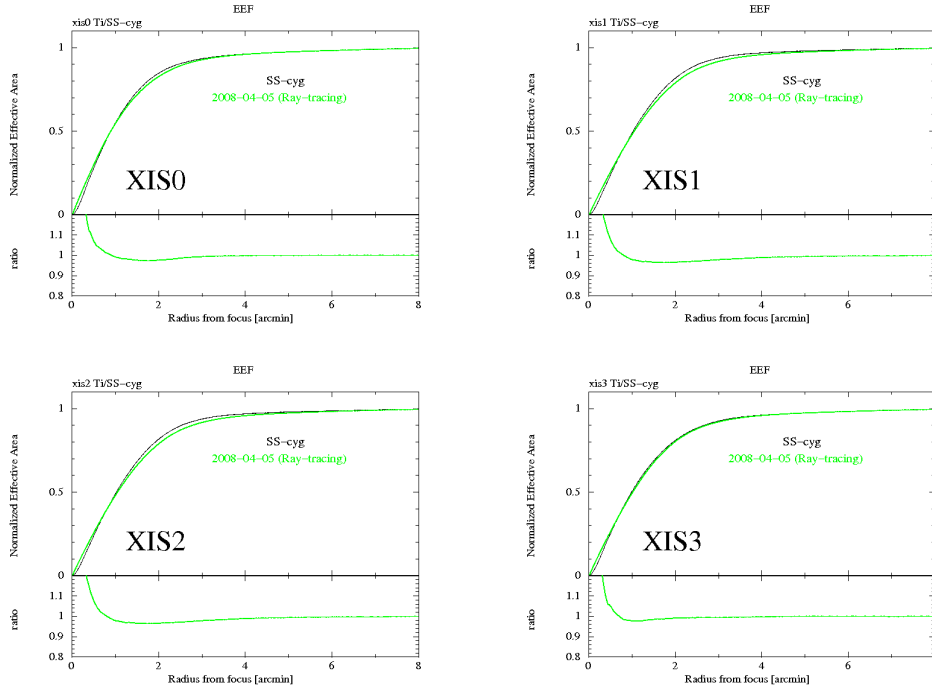


Figure 6.13: EEF of the four XRT-I images. The EEF is normalized to unity at the edge of the CCD chip (a square of $17'.8$ on the side). The lower panels show the ratio between the observed and simulated data.

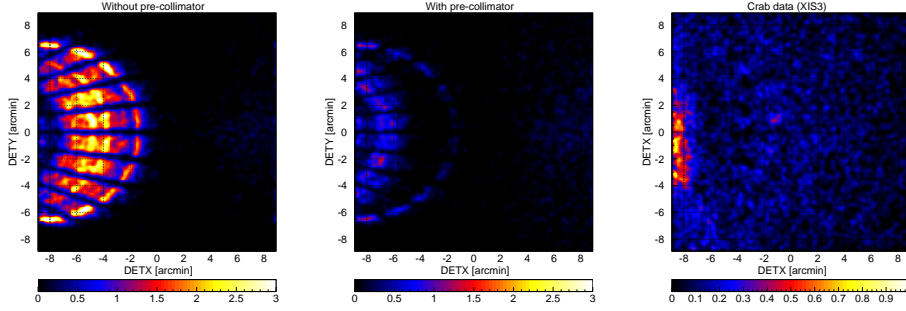


Figure 6.14: Focal plane images formed by stray light. The left and middle panels show simulated images of a monochromatic point-like source of 4.51 keV located at $(-20', 0')$ in (DETX, DETY) for the cases of without and with the pre-collimator, respectively. The radial dark lanes are the shades of the alignment bars. The right panel is the in-flight stray image of the Crab nebula in the 2.5–5.5 keV energy band located at the same off-axis angle. The unit of the color scale of this panel is counts per 16 pixels over the entire exposure time of 8428.8 s. The count rate from the whole image is 0.78 ± 0.01 counts s^{-1} including background. Note that the intensity of the Crab nebula measured with XIS3 at the XIS-default position is 458 ± 3 counts s^{-1} in the same 2.5–5.5 keV band. All the images are binned to 2×2 pixels and then smoothed with a Gaussian with a sigma of 2 pixels, where the pixel size is $24 \mu m$.

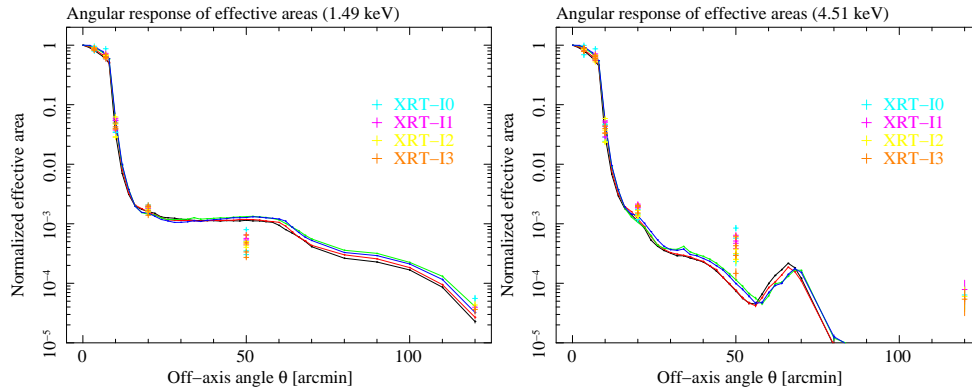


Figure 6.15: Angular responses of the XRT-I at 1.5 (left) and 4.5 keV (right) up to 2° . The effective area is normalized to 1 at the on-axis position. The integration area is corresponding to the detector size of the XISs ($17'8 \times 17'8$). The four solid lines in the plots correspond to different detector IDs. The crosses are the normalized effective area using the Crab pointings.

Chapter 7

X-Ray Imaging Spectrometer (XIS)

7.1 XIS Overview

The X-ray Imaging Spectrometer (XIS)¹ is composed of four units of X-ray cameras (Fig. 7.1). These employ X-ray sensitive silicon charge-coupled devices (CCDs) similarly to those used in the *ASCA* SIS, *Chandra* ACIS, *XMM-Newton* EPIC, and *Swift* XRT. In the photon counting mode, X-ray CCD detectors have imaging-spectroscopic capability. In each pixel of a CCD array, an incident X-ray photon is converted into a charge cloud with a total charge proportional to the energy of the absorbed X-ray. The charge is then shifted from one pixel to the next toward the gate of an output transistor by applying a time-varying electrical potential. This results in a voltage level (often referred to as “pulse height”) proportional to the energy of the X-ray photon.

The four sensors are named XIS0, 1, 2 and 3. The CCDs are each placed at the focal plane of a dedicated X-Ray Telescope. The four X-Ray Telescope modules are called XRT-I0, XRT-I1, XRT-I2, and XRT-I3.

Each CCD camera has a single CCD chip with an array of 1024×1024 pixels, covering an $18' \times 18'$ region. Each pixel is $24 \mu\text{m} \times 24 \mu\text{m}$, and the size of the CCD is $25 \text{ mm} \times 25 \text{ mm}$. One of the sensors (XIS1) uses a back-side illuminated (BI) CCD, while the other three use a front-side illuminated (FI) CCD. The XIS was developed and has been maintained jointly by Japan and the United States, with participating organizations including MIT, ISAS, Kyoto University, Osaka University, Rikkyo University, Ehime University, Miyazaki University, Kogakuin University, and Nagoya University.

¹The XIS quick reference (http://www.astro.isas.jaxa.jp/~tsujimot/pg_xis.pdf) gives a concise summary of the instrument with a particular focus on aiding observation planning.

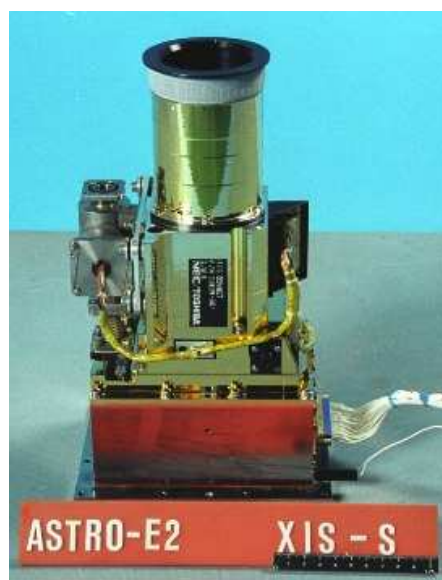


Figure 7.1: A photograph of one of the four XIS sensors before installation onboard *Suzaku*.

The XIS has been operated successfully since the launch in July 2005. The detector performance changes both continuously and discontinuously. One of the causes for discontinuous changes is the unavoidable occurrence of micro-meteorite hits in orbit. Such an event in November 2006 made the entire XIS2 dysfunctional. Another one in June 2009 caused a part of the XIS0 to be dysfunctional. Yet another one in December 2009 hit the XIS1, but its scientific impact has been evaluated to be minimal. Section 7.12 discusses the anomalies caused by these events. Users need to be aware of possible discontinuous changes through web resources and *Suzaku* memos.

A CCD has a gate structure on one of the surfaces to transfer the charge packets to the readout gate. The surface of the chip with the gate structure is called the “front side”. A front-side illuminated CCD (FI CCD) detects X-ray photons that pass through its gate structures, i.e., from the front side. Because of the additional photo-electric absorption at the gate structure, the low-energy quantum detection efficiency (QDE) of the FI CCD is rather limited. Conversely, a back-side illuminated CCD (BI CCD) receives photons from “back,” or the side without the gate structures. For this purpose, the undepleted layer of the CCD is completely removed in the BI CCD, and a thin layer to enhance the electron collection efficiency is added in the back surface. A BI CCD retains a high QDE even in a sub-keV energy band because of the absence of the gate structure on the photon-detection side. However, a BI CCD tends to have a slightly thinner depletion layer, and the QDE is therefore slightly lower in the high energy band. The decision to use only one BI CCD and three FI CCDs was made because of the slight additional risk involved in the new BI technology and the need to balance the overall efficiency for low- and high-energy photons.

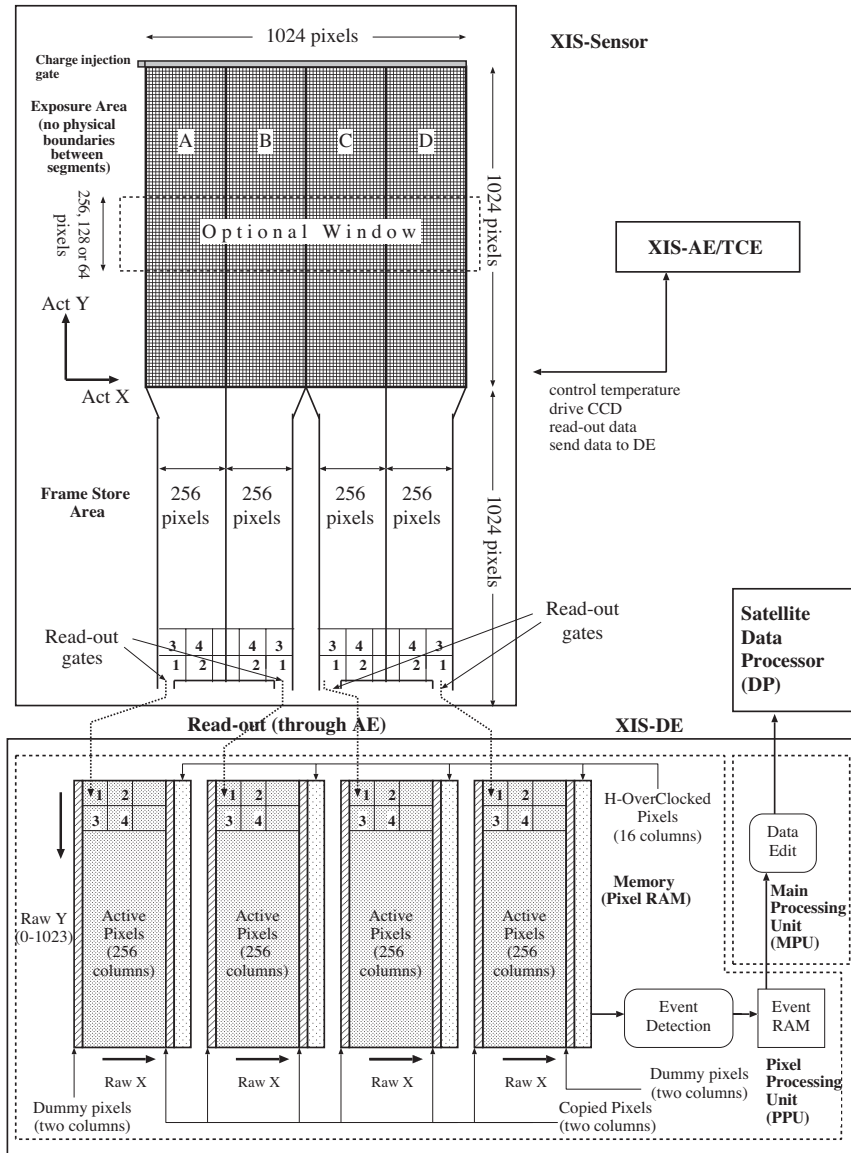


Figure 7.2: Schematic view of the XIS system. Each XIS consists of a single CCD chip with 1024×1024 X-ray sensitive cells, each $24 \mu\text{m}$ square. *Suzaku* has four CCD sensors (XIS0 to 3), two AE/TCUs (AE/TCE01 and AE/TCE23), two PPUs (PPU01 and PPU23), and one MPU. AE/TCU01 and PPU01 service XIS0 and XIS1, while AE/TCE23 and PPU23 service XIS2 and XIS3. Three of the XIS CCDs are front-illuminated (FI) and one (XIS1) is back-illuminated (BI).

Fig. 7.2 provides a schematic view of the XIS system. The Analog Electronics (AE)

drive the CCD and processes its data. Charge clouds produced in the exposure area in the CCD are transferred to the Frame Store Area (FSA) after the exposure according to the clocks supplied by the AE. The AE reads out data stored in the FSA sequentially, amplifies the data, and performs the analog-to-digital conversion. The AE outputs the digital data into the memory named Pixel RAM in the Pixel Processing Units (PPU). Subsequent data processing is done by accessing the Pixel RAM. To minimize the thermal noise, the sensors need to be kept at $\sim -90^\circ\text{C}$ during observations. This is accomplished by thermo-electric coolers (TECs), controlled by TEC Control Electronics, or TCE. The AE and TCE are located in the same housing, and together, they are called the AE/TCE. *Suzaku* has two AE/TCEs. AE/TCE01 is used for XIS0 and 1, and AE/TCE23 is used for XIS2 and 3. The digital electronics system for the XIS consists of two PPUs and one Main Processing Unit (MPU); PPU01 is associated with AE/TCE01, and PPU23 is associated with AE/TCE23. The PPUs access the raw CCD data in the Pixel RAM, carry out event detection, and send event data to the MPU. The MPU edits and packets the event data, and sends them to the satellite's main digital processor.

To reduce contamination of the X-ray signal by optical and UV light, each XIS has an Optical Blocking Filter (OBF) located in front of it. The OBF is made of polyimide with a thickness of 1000 \AA , coated with a total of 1200 \AA of aluminum (400 \AA on one side and 800 \AA on the other side). To facilitate the in-flight calibration of the XISs, each CCD sensor has two ^{55}Fe calibration sources². These sources are located on the side wall of the housing and are collimated in order to illuminate two corners of the CCDs. They can easily be seen in two corners of each CCD. A small number of these X-rays scatter onto the entire CCD.

The XIS had unexpectedly large contamination on the OBF from some material in the satellite. This reduced the low-energy efficiency of the XIS significantly. We monitor the contamination thickness by observing the calibration targets (e.g., 1E0102–72, RX J1856.5–3754) regularly. This effect is included in the response matrices. Details of the contamination are explained in section 7.7.

It is known that the CCD performance gradually degrades in space due to the radiation damage. This is because charge traps are produced by cosmic rays and are accumulated in the CCD. One of the unique features of the XIS is the capability to inject small amounts of charge to the pixels. The charge injection is quite useful to fill the charge traps periodically, and to make them almost harmless. This method is called the spaced-row charge injection (SCI), and the SCI has been adopted as a standard method since AO-2 to cope with the increase of the radiation damage (Uchiyama et al. 2009). The charge injection capability is also used to measure the charge transfer efficiency (CTE) of each CCD column in the case of the no-SCI mode (Nakajima et al. 2008; Ozawa et al. 2009). Details of the charge injection are explained in section 7.6.

²There is one more ^{55}Fe calibration source installed on the door. This source was used only during initial operations before the door opened, and is no more available.

7.2 CCD Pixels & Coordinates

A single XIS CCD chip consists of four segments (marked A, B, C and D in Fig. 7.2) and correspondingly has four separate readout nodes. Pixel data collected in each segment are read out from the corresponding readout node and sent to the Pixel RAM. In the Pixel RAM, pixels are given RAW X and RAW Y coordinates for each segment in the order of the readout, such that RAW X values are from 0 to 255 and RAW Y values are from 0 to 1023. These pixels in the Pixel RAM are named *active pixels*.

In the same segment, pixels closer to the read-out node are read-out faster and stored in the Pixel RAM faster. Hence, the order of the pixel read-out is the same for segments A and C, and for segments B and D, but different between these two segment pairs, because of the different locations of the readout nodes. In Fig. 7.2, numbers 1, 2, 3 and 4 marked on each segment and the Pixel RAM indicate the order of the pixel read-out and the storage in the Pixel RAM.

In addition to the active pixels, the Pixel RAM stores the *copied pixels*, *dummy pixels* and *H-over-clocked pixels* (Fig. 7.2). At the borders between two segments, two columns of pixels are copied from each segment to the other. Thus these are named copied pixels. Two columns of empty dummy pixels are attached to the segments A and D. In addition, 16 columns of H-over-clocked pixels are attached to each segment.

Actual pixel locations on the chip are calculated from the RAW XY coordinates and the segment ID during ground processing. The coordinates describing the actual pixel location on the chip are named ACT X and ACT Y coordinates (Fig. 7.2). It is important to note that the RAW XY to ACT XY conversion depends on the on-board data processing mode (see section 7.4).

7.3 Pulse Height Determination & Hot Pixel Rejection

When a CCD pixel absorbs an X-ray photon, the X-ray is converted to an electric charge, which in turn produces a voltage at the analog output of the CCD. This voltage (“pulse height”) is proportional to the energy of the incident X-ray. In order to determine the true pulse height corresponding to the input X-ray energy, it is necessary to subtract the *dark levels* and correct possible *optical light leaks*.

Dark levels are non-zero pixel pulse heights caused by leakage currents in the CCD. In addition, optical and UV light might enter the sensor due to imperfect shielding (“light leak”), producing pulse heights that are not related to X-rays. The analysis of the ASCA SIS data, which utilized the X-ray CCD in photon-counting mode for the first time, showed that the dark levels were different from pixel to pixel, and the distribution of the dark level did not necessarily follow a Gaussian function. On the other hand, light leaks are considered to be rather uniform over the CCD.

For the *Suzaku* XIS, the dark levels and the light leaks are calculated separately in the normal mode. The dark levels are defined for each pixel and are expected to be constant for a given observation. The PPU calculates the dark levels in the Dark Initial mode (one of the special diagnostic modes of the XIS); those are stored in the Dark Level RAM. The average dark level is determined for each pixel, and if the dark level is higher than the hot-pixel threshold, this pixel is labeled as a *hot pixel*. The dark levels can be updated by the Dark Update mode, and sent to the telemetry by the Dark Frame mode. The analysis of the *ASCA* data showed that the dark levels tend to change mostly during the SAA passage of the satellite. The Dark Update mode may be employed several times a day after the SAA passage.

Hot pixels are pixels which always output pulse heights larger than the hot-pixel threshold even without input signals. Hot pixels are not usable for observations, and their outputs have to be disregarded during scientific analysis. The XIS detects hot pixels on-board by the Dark Initial/Update mode, and their positions are registered in the Dark Level RAM. Thus, hot pixels can be recognized on-board, and they are excluded from the event detection processes. It is also possible to specify the hot pixels manually. However, some pixels output pulse heights larger than the threshold intermittently. Such pixels are called flickering pixels. It is difficult to identify and remove the flickering pixels on board. They are inevitably output to the telemetry and need to be removed in scientific analyses, for example by using the FTTOOLS `sisclean`. Flickering pixels sometimes cluster around specific columns, which makes them relatively easy to identify.

The light leaks are calculated on board with the pulse height data after subtraction of the dark levels. A truncated average is calculated for 256×114 pixels (this size was 64×64 before January 18, 2006) in every exposure and its running average produces the light leak. In spite of the name, light leaks do not represent in reality optical/UV light leaks to the CCD. They mostly represent fluctuation of the CCD output correlated to the variations of the satellite bus voltage. The XIS has little optical/UV light leak, which is negligible unless the bright earth comes close to the XIS field of view.

The dark levels and the light leaks are merged in the Parallel-sum (P-Sum) mode, so the Dark Update mode is not available in the P-Sum mode. The dark levels, which are defined for each pixel as the case of the normal mode, are updated every exposure. It may be considered that the light leak is defined for each pixel in the P-Sum mode.

7.4 On-Board Event Analysis

The main purpose of the on-board processing of the CCD data is to reduce the total amount of data transmitted to the ground. For this purpose, the PPU searches for a characteristic pattern of the charge distribution (called an event) in the pre-processed (post-dark level and light leak subtraction) frame data. When an X-ray photon is absorbed in a pixel, the photo-ionized electrons can spread into at most four adjacent pixels.

An event is recognized when a pixel has a pulse height which is between the lower and the upper event thresholds and is larger than those of eight adjacent pixels (e.g., it is the peak value in the 3×3 pixel grid). In the P-Sum mode, only the horizontally adjacent pixels are considered. The copied and the dummy pixels ensure that the event search is enabled on the pixels at the edges of each segment. The RAW XY coordinates of the central pixel are considered the location of the event. Pulse-height data for the adjacent 5×5 square pixels (or three horizontal pixels in the P-Sum mode) are sent to the Event RAM as well as the pixel location.

The MPU reads the Event RAM and edits the data to the telemetry format. The amount of information sent to the telemetry depends on the editing mode of the XIS. All the editing modes (in the normal mode, see section 7.5) are designed to send the pulse heights of at least four pixels of an event to the telemetry, because the charge cloud produced by an X-ray photon can spread into at most four pixels. Information of the surrounding pixels may or may not be output to the telemetry depending on the editing mode. The 5×5 mode outputs the most detailed information to the telemetry, i.e., all 25 pulse-heights from the 5×5 pixels containing the event. The size of the telemetry data per event is reduced by a factor of two in the 3×3 mode, and another factor of two in the 2×2 mode. Details of the pulse height information sent to the telemetry are described in the next section.

7.5 Data Processing Modes

There are two different kinds of on-board data processing modes. The *Clock modes* describe how the CCD clocks are driven, and determine the exposure time, the exposure region, and the time resolution. The Clock modes are determined by a program (“micro-code”) loaded into the AE. The *Editing modes* specify how detected events are edited, and determine the format of the XIS data telemetry. The Editing modes are determined by the digital electronics.

In principle, each XIS sensor can be operated with different mode combinations. However, we expect that most observations will use all three sensors³ in the Normal 5×5 or 3×3 mode (without the Burst or Window options). Other modes are useful for bright sources (when pile-up or telemetry limitations are a concern) or if a higher time resolution (< 8 s) is required.

7.5.1 Clock Modes

There are two kinds of Clock modes in the XIS, the Normal and the Parallel-Sum (P-sum) mode. Furthermore, two options (the Window and the Burst options) may be used in

³XIS2 is currently out of use.

Table 7.1: Effective area and exposure time for different Burst and Window options.

Option	Effective area (nominal: 1024×1024 pixels)	Exposure time (in 8 s period)
None	1024×1024 pixels	$8 \text{ s} \times 1$ exposures
Burst	1024×1024 pixels	$(8 - t) \text{ s} \times 1$ exposures
Window	256×1024 pixels	$2 \text{ s} \times 4$ exposures
	128×1024 pixels	$1 \text{ s} \times 8$ exposures
Burst & Window	256×1024 pixels	$(2 - t) \text{ s} \times 4$ exposures

Note: t is a dead time in the Burst option.

combination with the Normal mode. However, see section 7.5.3 for restrictions using the Parallel-Sum mode.

- **Normal Mode:** If neither *Window* nor *Burst* option (see below) is specified, the exposure time is eight seconds, and all the pixels on the CCD are read out every eight seconds. This can be combined with either of the 5×5 , 3×3 , and 2×2 Editing modes.
- **Parallel-Sum Mode:** The pixel data from multiple rows are summed in the Y-direction on the CCD, and the sum is put in the Pixel RAM as a single row. The number of rows to add is commandable, but only 128-row summation is supported at present. The Parallel-Sum mode can be used only with the Timing Editing mode, and the Y coordinate is used to determine the event arrival time. As a result, no spatial resolution is available in the Y-direction. The time resolution of the Parallel-Sum mode is $8 \text{ s}/1024 \sim 7.8 \text{ ms}$.

7.5.2 Window & Burst Options

Table 7.1 indicates how the effective area and exposure time are modified by the Burst and the Window options.

In the Normal Clock mode, the *Window* and the *Burst* options can modify the effective area and exposure time, respectively. The two options are independent, and may be used simultaneously. These options cannot be used with the P-Sum Clock mode.

- **Burst Option:** All pixels are read out every eight seconds (if the Window option is not specified), but the exposure time can be reduced by introducing a dead time; X-ray events detected during the first $t \text{ s}$ are discarded, and the exposure time is $8 - t \text{ s}$. This option may be used to avoid photon pile-up when observing a bright source.

- **Window Option:** This option allows shorter exposure times by reading out only a portion of the CCD more frequently. Only a part of the chip within the Y-direction range specified by the commandable Window is used for exposure (Fig. 7.2). The Window width in the Y-direction is 256 pixels around the aim point. When the Window width is 256 pixels (1/4 Window), the exposure time becomes a quarter of that without the Window option (i.e., 2 s), and the Pixel RAM is filled with the data from four successive exposures.

The Window width can be 128 pixels (1/8 Window). However, a significant fraction of the source photons may be lost due to the tail of the XRT point spread function. Furthermore, the fractional loss may be modulated by the attitude fluctuation of the satellite, which is synchronized with the orbital motion of the satellite. Thus the XIS team do not recommend the 1/8 Window option.

One of the disadvantages of the Window option is that the X-rays from the calibration sources ^{55}Fe are out of the window. This makes it difficult to check the gain and the energy resolution of the XIS.

We show in Fig. 7.3 the time sequence of exposure, frame-store transfer, CCD read-out, and storage to the Pixel RAM (in PPU) in the normal mode with or without the Burst/Window option.

7.5.3 Editing Modes

Editing modes may be divided into two categories, observation modes and diagnostics modes. We describe here mainly the observation modes. General users usually do not need to analyze the data of the diagnostic modes. Among the observation modes, three modes (5×5 , 3×3 , and 2×2) are usable in the Normal Clock mode, and only the Timing mode can be specified in the P-Sum mode.

Please note that guest observers cannot specify the Editing mode for their observations; the Suzaku operation team selects the Editing mode by considering the counting rate and the telemetry limit.

Observation Modes

- **5×5 mode:** All the pulse heights of the 25 pixels centered at the event center are sent to the telemetry. This is used with the Normal Clock mode.
- **3×3 mode:** Pulse heights of the 9 pixels centered at the event center are sent to the telemetry with the 1-bit information (whether the pulse height is larger than the Split Threshold Outer or not) for the surrounding 16 pixels. This is used with the Normal Clock mode.

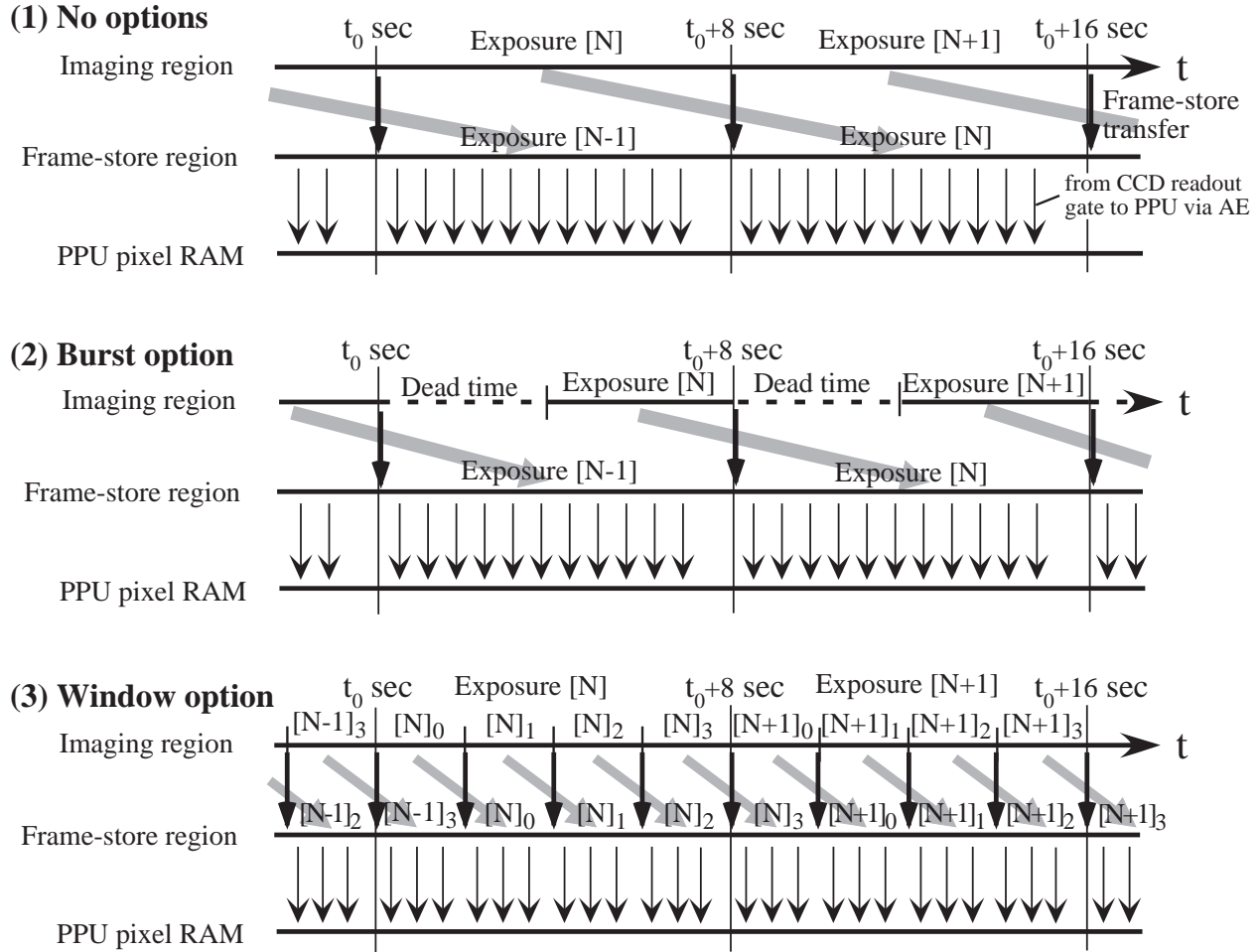


Figure 7.3: Time sequence of the exposure, frame-store transfer, CCD readout, and data transfer to the Pixel RAM in PPU is shown (1) in the Normal mode with no options, (2) in the Normal mode with the Burst option, and (3) in the Normal mode with the Window option. In this example, the 1/4 Window option is assumed.

- **2 × 2 mode:** Pulse heights of the 2 × 2 square pixels are sent to the telemetry. The 2 × 2 pixels are selected to include the event center, the second highest pixel in the cross centered at the event center, and the 3rd (or 4th) highest pixel in the cross. The 1-bit information (whether the pulse height is larger than the Split Threshold Outer or not) of the 8-attached pixels is also output to the telemetry. This is used with the Normal Clock mode.
- **Timing mode:** Total pulse heights and grades of the events are output to the

telemetry. The pulse heights of at most three pixels in the X-direction are summed to give the total pulse height if they are over the Inner Split Threshold. The position and the number of pixels exceeding the threshold determine the *grades*. This is used only with the P-Sum Clock mode. The Window and the Burst Options are not available in the Timing mode.

We show in Fig. 7.4 the pixel pattern whose pulse height or 1-bit information is sent to the telemetry. We do not assign grades to an event on board in the Normal Clock mode. This means that a dark frame error, if present, can be corrected accurately during the ground processing even in the 2×2 mode. The definition of the grades in the P-Sum mode is shown in Fig. 7.5.

No significant difference has been found so far between the 5×5 and 3×3 modes. However, the 2×2 mode is slightly different from the 3×3 or 5×5 mode. The difference is produced during the CTE correction in the ground processing. Because the pulse height information is limited in the 2×2 mode, some of the CTE corrections cannot be applied to the 2×2 mode data. This causes a slight difference in the gain of the 2×2 mode data. As of August 2009, the gain difference has been measured, and the XIS software (`xispi`) takes the difference into consideration. However, the gain adjustment is optimized at the XIS nominal position and a slight gain difference of about 5 eV at 6 keV can be seen at off-axis positions. The 2×2 mode is employed only when a bright source is observed (see tables 7.7 and 7.8). Those who plan to observe a bright source should be aware of these systematics in the 2×2 mode. The 2×2 mode is not used in the BI CCD (XIS1), because a relatively small CTE in the BI CCD produces significant calibration difference from the 5×5 and the 3×3 modes.

Note on the Timing Mode

From AO-5 on, the Timing mode can be used for a restricted number of observations. The total exposure of the Timing mode observations will less than 5% of the overall time allocation. However, the calibration accuracy of the Timing mode remains worse than that of the Normal mode (compare sections 7.11.2 and 7.11.3), and there are some operational restrictions. Therefore, those who consider using the Timing mode should demonstrate the feasibility of their observations under the operational restrictions and the poorer calibration accuracy described below.

The Timing mode is available only for the XIS3. There are comparably large numbers of hot/flickering pixels in the BI CCD, which are difficult to remove completely on board. The remaining hot/flickering pixels are found to fill the telemetry easily, since a single hot pixel can produce 1024 events in 8 s in the Timing mode. Due to this telemetry occupation by hot/flickering pixels, we cannot use the Timing mode for the BI CCD. Note that this does not happen in the Normal mode. The FI CCDs have only a small number of hot/flickering pixels, although some of them need to be removed during the data analysis. In addition, we found that we need to regularly reset the dark level to retain its stability (\sim once per

96 min). This means that we cannot take very long continuous data. This may not become a practical restriction, because the data acquisition becomes intermittent anyway due to SAA passages and earth occultation of the target.

Since only one dimensional information is available in the Timing mode, the distinction between X-ray and non-X-ray events becomes inaccurate. This means that the Timing mode has a significantly higher non-X-ray background than the Normal mode. Preliminary analyses showed that the non-X-ray background in the Timing mode is one or two orders of magnitude larger than in the Normal mode. Because the available data are limited, its detailed behavior, e.g., dependence on the cut-off rigidity, is not known.

The in-flight calibration of the Timing mode is on-going and is expected to improve in the near future. However, it will not reach that of the Normal mode, because (1) the Spaced-row Charge Injection (SCI) is not available on board and (2) the CTI correction is difficult in the ground processing. The updated calibration information of the Timing mode will be released as part of the CALDB, as an analysis recipe, and so on. Because the calibration of the Timing mode is evolving, we give here only a rough description of it based on the currently available results. Those who consider to use the Timing mode (or to analyze the Timing mode data) are advised to visit the Suzaku web for the latest calibration information.

Unavailability of the SCI or the CTI correction means that the energy scale and resolution are significantly different from those of the Normal mode (compare sections 7.11.2 and 7.11.3). A preliminary analysis showed that the gain was lower than the nominal value by $\sim 10\%$ and the energy resolution was degraded to $\sim 5\%$ at 5.9 keV in early 2009. The former may be corrected if appropriate calibration information becomes available, but the latter not. In addition, the effective area of the CCDs may change in the Timing mode: even a small number of hot pixels produces a relatively large dead area in the CCD, which reduces the effective area. This reduction could be time dependent, because some of the hot pixels often disappear and reappear. It should be noted that the accuracy of the ARF file may also be degraded, because we need to use a rectangular extraction region for the Timing mode. The nominal time resolution in the Timing mode is 7.8 ms, but this depends on the image size of the X-ray source. If the X-ray image is much larger than 128 pixels (~ 2 arcmin) along the Y-address, the time resolution may become worse than 7.8 ms. Because the Y-address represents the photon arrival time in the Timing mode, the image extension (in the Y-direction) works as a low-pass filter. This means that, even for a point source, some signal is leaked to the adjacent time bins due to the tail of the XRT PSF. Therefore, the frequency response is somewhat reduced near the Nyquist frequency of the nominal time resolution of 7.8 ms.

Diagnostic Modes

Besides the observation modes explained above, the XIS instrument has several diagnostic modes, the Frame mode, the Dark Initial mode, the Dark Update mode, and the

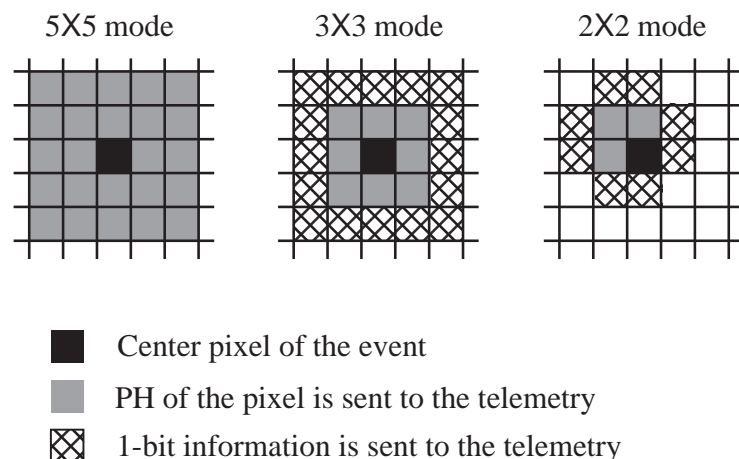


Figure 7.4: Information sent to the telemetry is shown for 5×5 , 3×3 , and 2×2 modes. 1-bit information means whether or not the PH of the pixel exceeds the outer split threshold. In 2×2 mode, the central 4 pixels are selected to include the second and the third (or fourth) highest pixels among the 5 pixels in a cross centered at the event center.

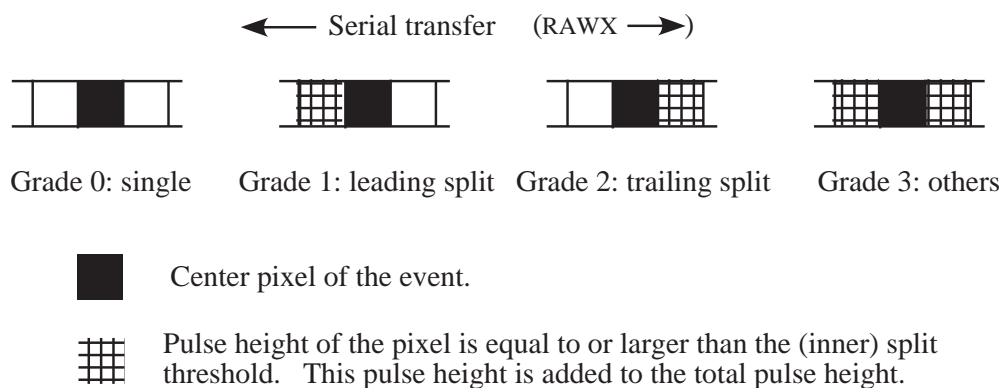


Figure 7.5: Definition of the grades in the P-Sum/Timing mode. Total pulse height and the grade of the event are output to the telemetry. Note that the grades are defined referring to the direction of the serial transfer, so the central pixel of the grade 1 event has the *larger* RAW-X value than the second pixel, while the opposite is true for the grade 2 event.

Dark Frame mode. The Frame mode simply dumps the raw CCD data to the telemetry. This mode may be useful for the health check of the CCD. Other modes are used primarily in determining/checking the dark levels. The Dark Init mode is employed when the Burst/Window options are changed. The Dark Update mode is used just after the SAA passage to update the hot pixel list on board. It is unlikely that those would be used by

guest observers.

7.5.4 Discriminators

Three kinds of discriminators, the area, the grade and the class discriminators, can be applied during the on-board processing. The grade discriminator is available only in the Timing mode. The class discriminator was implemented after the launch of *Suzaku* and was used since January, 2006. In most cases, guest observers need not to change the default setting of these discriminators.

The class discriminator classifies the events into two classes, “X-rays” and “others,” and outputs only the “X-ray” class to the telemetry when it is enabled. This class discriminator is always enabled to reduce the telemetry usage of non-X-ray events. The “other” class is close to, but slightly different from the ASCA grade 7. When the XIS points to a blank sky, more than 90% of the detected events are particle events (mostly the ASCA grade 7). If we reject these particle events on board, we can make a substantial saving in the telemetry usage. This is especially useful when the data rate is medium or low. The class discriminator realizes such a function in a simple manner. When all the eight pixels surrounding the event center exceed the Inner Split Threshold, the event is classified as the “other” class, and the rest of the events as the “X-ray” class. With such a simple method, we can reject more than three quarters of the particle events. The class discriminator works only for the 5×5 and 3×3 modes. It is not available in the 2×2 mode and the timing mode.

The area discriminator is used when we want to reject some (or most) of the frame data from the event extraction. The discriminator works on the Pixel RAM. When the discriminator is enabled, a part of the Pixel RAM is not used for the event extraction. This may be useful when a bright source is present in the XIS field of view other than the target source. If we set the discrimination area to include only the bright source, we can avoid outputting unnecessary events to the telemetry. Only a single, rectangular area can be specified in a segment for discrimination. Either the inside or the outside of the area can be rejected from the event extraction. Note that the area discriminator works on the Pixel RAM, not on the physical area of the CCD. This is important when we apply the discriminator with the Window option.

The grade discriminator is only used in the timing mode. Any combination of the four grades can be selected to discriminate the grade for telemetry output.

Suzaku does not have the level discriminator, which was used in the ASCA SIS. The same function can be realized, however, by changing the event threshold.

7.6 Spaced-Row Charge Injection

The performance of the CCDs gradually degrades in the space environment due to radiation damage by cosmic-ray particles. The Spaced-row Charge Injection (SCI) is used to restore the performance of the CCDs. The Charge Transfer Efficiency (CTE) is restored by the SCI, and the energy resolution is improved. The SCI has been used by default since October 2006, whenever possible.

7.6.1 Principle

The performance of the XIS is gradually degrading since the launch of *Suzaku* due to the radiation damage. The energy resolution in Sept. 2006 measured by the on-board ^{55}Fe calibration source was about 200 eV (FWHM) at 5.9 keV, while it was $\sim 130\text{--}135$ eV just after the launch.

In principle, a precision charge injection capability can mitigate the effects of in-flight radiation damage (Bautz et al. 2004). A sufficient quantity of charge injected periodically during the array readout process will tend to fill radiation-induced traps. These filled traps do not capture X-ray signal charge, and the degradation of the CTE can be mitigated. Because the traps need to be filled quite often, we inject charge every 54 rows in every exposure. The charge injected rows are not usable to detect X-ray photons and become dead areas.

The SCI has been used as a standard observation method since October 2006. Details on the calibration of the SCI-on observations can be found in Uchiyama et al. (2009).

7.6.2 Supported Modes

The SCI is applicable only for the Normal mode. It is not supported for the Timing mode. Some of the Burst, Window, and Window+Burst options are also supported. The supported observation modes are listed in Table 7.2. Those who want to know the supported modes in detail should consult the latest microcode file (e.g., `ae_xis_ucodelst_20090317.fits`) in the *Suzaku* CALDB. The “UCODE_LIST_SCI” extension of the file is devoted to the SCI and the “COMMENT” column is useful.

7.6.3 Data Impact

Here we summarize how the SCI affects the data compared to when no SCI is used. There are several demerits associated with the SCI. Guest observers should be aware of these characteristics of the SCI data.

1. The energy resolution will improve from $\sim 200\text{--}220$ eV (FWHM) to ~ 150 eV (FI) and

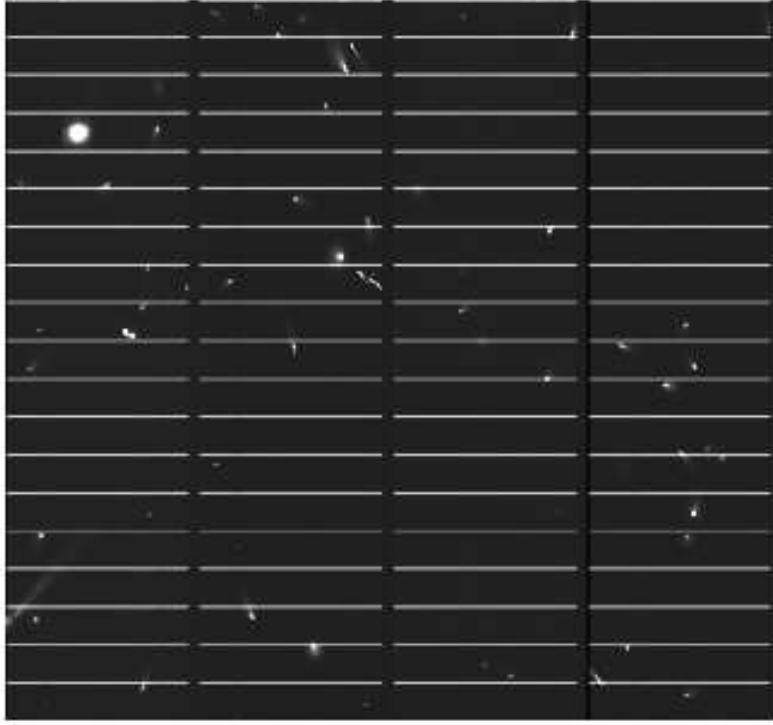


Figure 7.6: Frame mode data of XIS2 taken with Spaced-row Charge Injection (SCI). The bright lines at every 54th row correspond to the charge injected rows. These rows are disconnected because the over-clocked regions are also displayed at the segment boundaries.

Table 7.2: Supported clock mode and option with the SCI.

Window option	none					1/4 win					1/8 win
Burst option	none	2.0s	0.73s	0.5s	0.1s	none	1.0s	0.5s	0.3s	0.135s	none
XIS0	○	○	N/A	N/A	△	○	○	○	△	△	△
XIS1	○	○	○	○	△	○	○	○	△	△	△
XIS3	○	○	N/A	N/A	△	○	○	○	△	△	△

○: Normal operation.

△: Special operation. Not recommended by the XIS team.

Note: The P-sum mode is only available for XIS3, without SCI.

~220 eV (BI) in the iron K band as of July, 2009.

- Dead rows are produced every 54th row. The width of the dead area is 3 rows (the charge-injected rows and their preceding/trailing rows). The dead rows are fixed in RAW X, RAW Y coordinates and are common to all the sensors. This means that the

dead area is 5.6% of the image. Because the width of the dead area is much smaller than the point-spread-function of the XRT and the satellite attitude fluctuates, we believe that these dead areas do not hamper the image analysis.

3. The number of out-of-time events will increase. It takes about 25 ms to transfer the image area data to the frame-store area when no SCI is implemented. This increases to 156 ms when the SCI is used. This means that the fraction of the out-of-time events increases from 0.3% to 2.0%.
4. The number of hot pixels slightly increases with the SCI. This may introduce a slight increase of the dead area due to the hot pixels, but the increase is negligible compared to the dead area due to the injected charge itself.

7.7 Low Energy Efficiency Degradation

The good low energy response is an important unique feature of the XIS. However, the effective area below 2 keV has been decreasing with time after launch. The degradation is characterized by additional absorption of carbon-dominated material. The thickness of this extra absorber is different for each sensor, but becomes maximal at the center of the XIS CCD and decreases toward the edge of the field of view. Although the origin of the extra absorber has not yet been identified, it is most likely some contaminant accumulating on the surface of the XIS Optical Blocking Filters (OBF), which is one of the coldest parts inside the satellite.

In order to examine this efficiency degradation, we have observed soft and stable X-ray sources, such as, 1E0102–72, RX J1856.5–3754, and the Cygnus loop, repeatedly. Atmospheric fluorescent lines of nitrogen and oxygen are also useful to evaluate the spatial dependence of the contaminant thickness over the CCD. The analysis of these data leads to our current knowledge of the extra absorber (or the contaminant on the OBF), as summarized below.

1. The extra absorber is mainly made of carbon. The absorber also contains oxygen, but its contribution is less than 1/5 of that of carbon by number.
2. Fig. 7.7 shows the evolution of the extra absorber thickness as a function of time after the XIS door was opened. The evolution is different between the sensors; the evolution of XIS3 seems to gradually slow down and is almost saturated 200–300 days after the XIS door was opened, while the contaminant on XIS0 is still increasing in 2010. The solid curves are the best-fit empirical functions to the data. Note that the absorber thickness in this plot is measured at the center of the FOV, where the absorber thickness is maximal.

3. The spatial distribution of the absorber thickness for XIS1 (BI-CCD) is shown in Fig. 7.8 as a function of the distance from the center of the FOV. The extra absorber is thinner near the edge of the FOV. This radial profile and its time evolution are approximated with a simple analytic function (see Koyama et al. 2007).

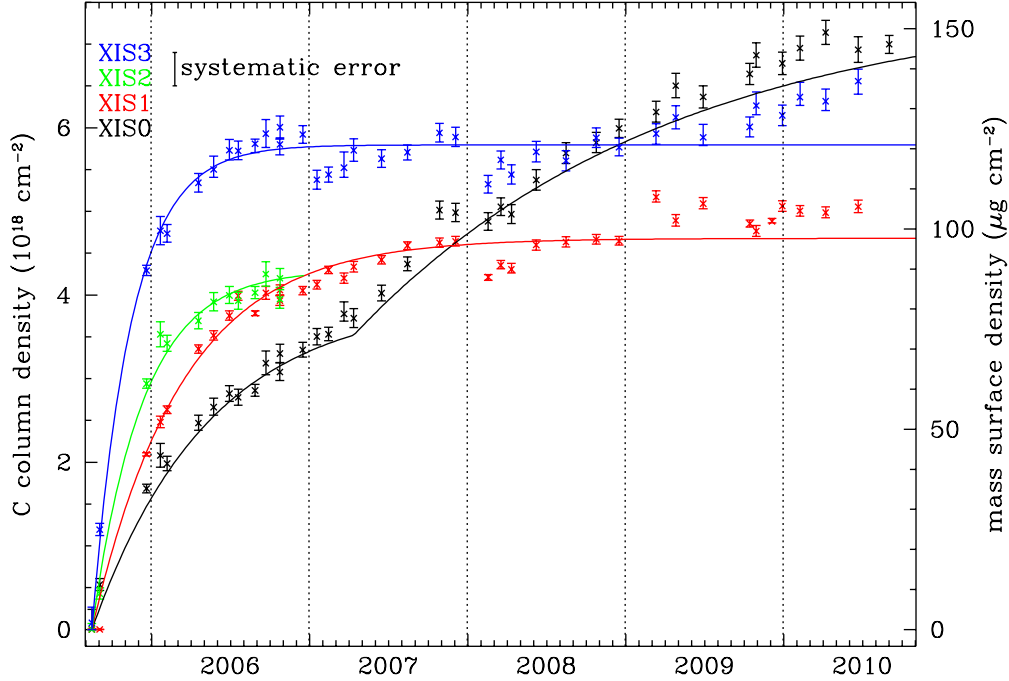


Figure 7.7: An empirical model for the on-axis contamination evolution, assuming DEHP ($\text{C}_{24}\text{H}_{38}\text{O}_4$, or $\text{C}/\text{O} = 6$ by number) as contaminant. Crosses indicate the C column density of the contaminant derived from the E0102–72 observations. Solid lines indicate the best fit empirical model to the time evolution of the contamination for each sensor.

These results, the empirical models of the contamination thickness in particular, are implemented in the *Suzaku* analysis software. The instrument team discourages the use of XSPEC models to describe this extra absorption (such as `xisabs`, `xiscoabs`, `xiscoabh`, `xispcoab`) but recommends the use of a modified ARF file in which the absorption is taken into account. Such an ARF file can be generated with the *Suzaku* FT00L `xissimarfgn`. A detailed description can be found in Ishisaki et al. (2007), and on the *Suzaku* web site. For diffuse sources, one needs to make an ARF with `xissimarfgn` considering the extension of the source.

The calibration of the efficiency degradation due to the extra-absorption is still in progress. For example, relative contribution of oxygen to carbon has not yet been deter-

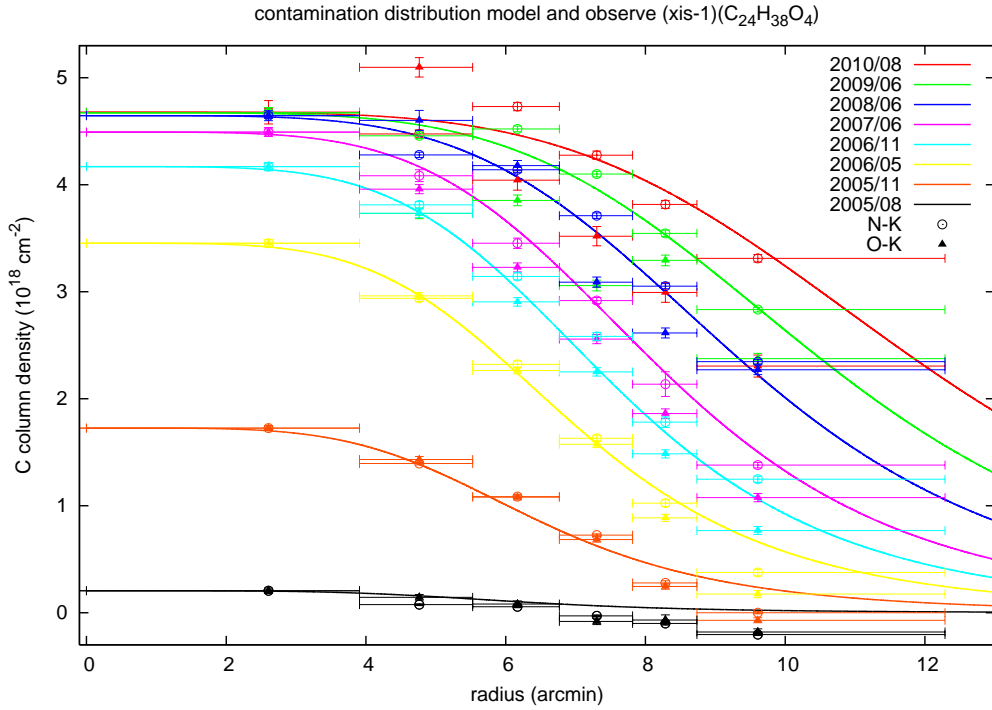


Figure 7.8: Temporal evolution of the radial profile of the contamination thickness derived from N and O fluorescent lines from the day earth (i.e., Sun-lit Earth) atmosphere. Open circles and filled triangles represent the data points determined by the N and O fluorescence lines, respectively. The best fit model is also shown in the figure. Note that, for the on-axis column densities, the results in Fig. 7.7 are used.

mined accurately. At present, we adopt the ratio of 1/6 in the above models, but there are indications that the ratio is different for each sensor or changing in time. We also know that for some sources an effective area decrease is evident above 2 keV (typically 5%), where our current absorption models with carbon and oxygen predict little effect. Further study of this issue might be required. Furthermore, the radial profile of the extra absorber has been studied in detail only for XIS1 (BI-CCD), but not in detail for the other sensors.

The future development of the efficiency degradation is difficult to predict. However, the extrapolation of the current evolution curves (Fig. 7.7) will be appropriate for AO-6 proposals. For AO-6 proposers we provide an ARF in which the amount of efficiency degradation as expected for October 2011 is taken into account. These ARF files have been generated with `xissimarfgen`. The ARFs for diffuse sources should be generated with `xissimarfgen` by proposers.

7.8 Non-X-Ray Background

All *Suzaku* XISs have low backgrounds, due to a combination of *Suzaku*'s orbit and the instrumental design. The large effective area at the Fe K line band (comparable to the *XMM-Newton* PN) combined with this low background makes *Suzaku* a powerful tool for investigating high energy sources. In the XIS, the background originates from the cosmic X-ray background (CXB) combined with charged particles (the non-X-ray background, or NXB). Currently, flickering pixels are a negligible component of the background. When observing the dark Earth (i.e., the NXB), the background rate in the 0.4–12 keV band is 0.1–0.2 counts/s in the FI CCDs and 0.3–0.6 counts/s in the BI CCD. Note that these are the fluxes after the grade selection is applied with only the ASCA grades 0, 2, 3, 4, and 6 being selected. Fig. 7.9 shows the NXB spectra for each sensor.

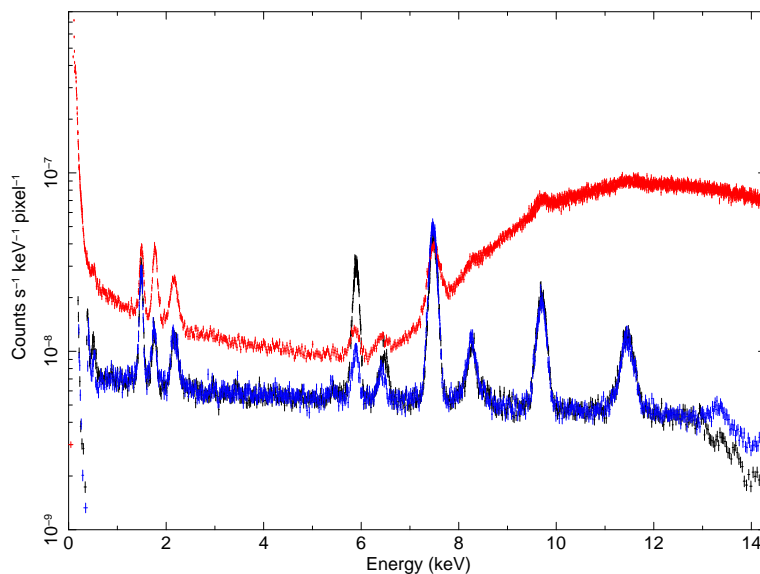


Figure 7.9: Non-X-ray background (NXB) rate for XIS0 (black), XIS1 (red), and XIS3 (blue). The spectra are constructed from night Earth observations from the SCI start to May 2010.

There are also fluorescence features arising from the calibration sources as well as material in the XIS and XRTs. The Mn lines are due to scattered X-rays from the calibration sources. As shown in Table 7.3 they are almost negligible except for XIS0. The other lines are fluorescent lines from the material used for the sensor. Table 7.3 shows the current best estimates for the strength of these emission features, along with their 90% confidence errors.

The NXB is not uniform over the chip. Its flux tends to be slightly higher at larger ACTY as shown in Fig. 7.10. This is because some fraction of NXB is produced in the

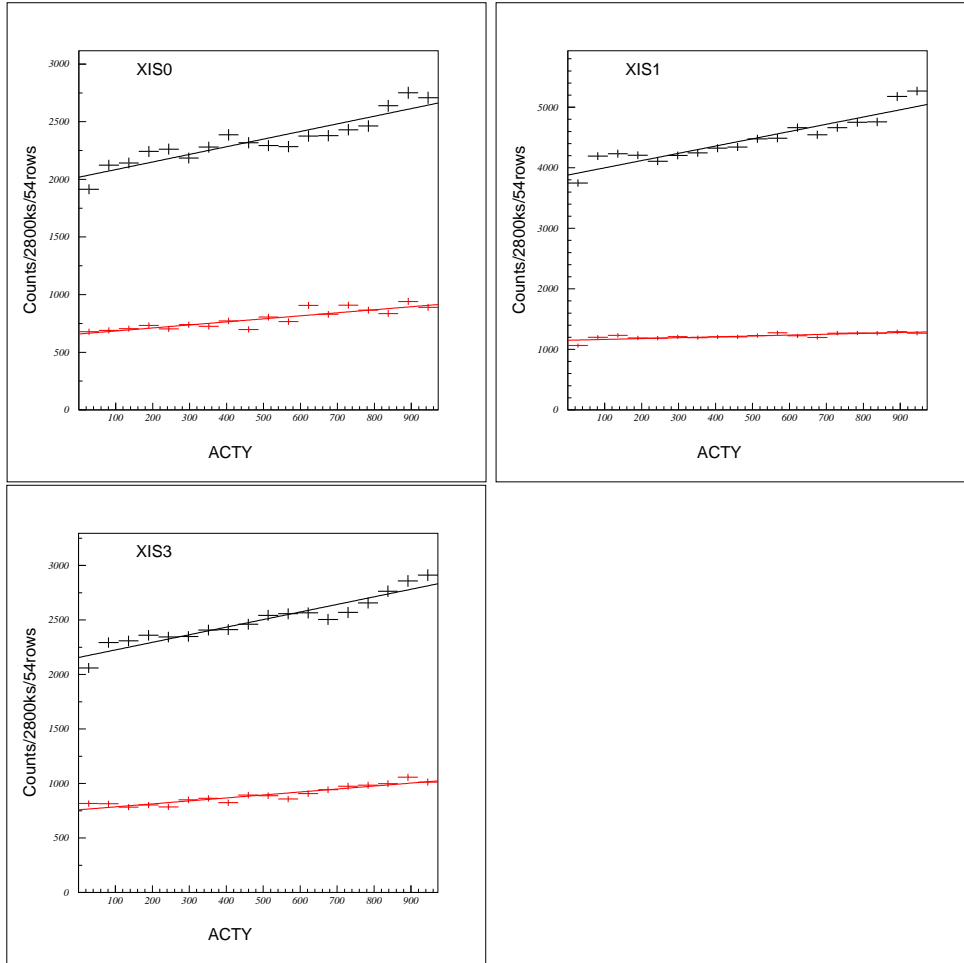


Figure 7.10: ACTY dependence of the NXB for XIS0, XIS1, and XIS3. Black lines indicate the continuum component (2.5–5.5 keV), while the red lines indicate the Ni $K\alpha$ line component (7.2–7.8 keV). The NXB flux tends to be higher at larger ACTY, because some fraction of the NXB is produced in the frame store region.

frame-store region. The fraction may be different between the fluorescent lines and the continuum. This causes slight difference in the ACTY dependence of the NXB.

The total flux of the NXB depends on the cut-off rigidity (COR) as shown in Fig. 7.11. This is expected as the NXB is produced by the charged particles, the flux of which is higher at lower COR. This means that, when we use the NXB database to subtract the background, we need to select the NXB for an appropriate range of COR values, which matches with the COR distribution of the on-source observation. For this purpose, the XIS FT00LS `xisnxbgen` can be used.

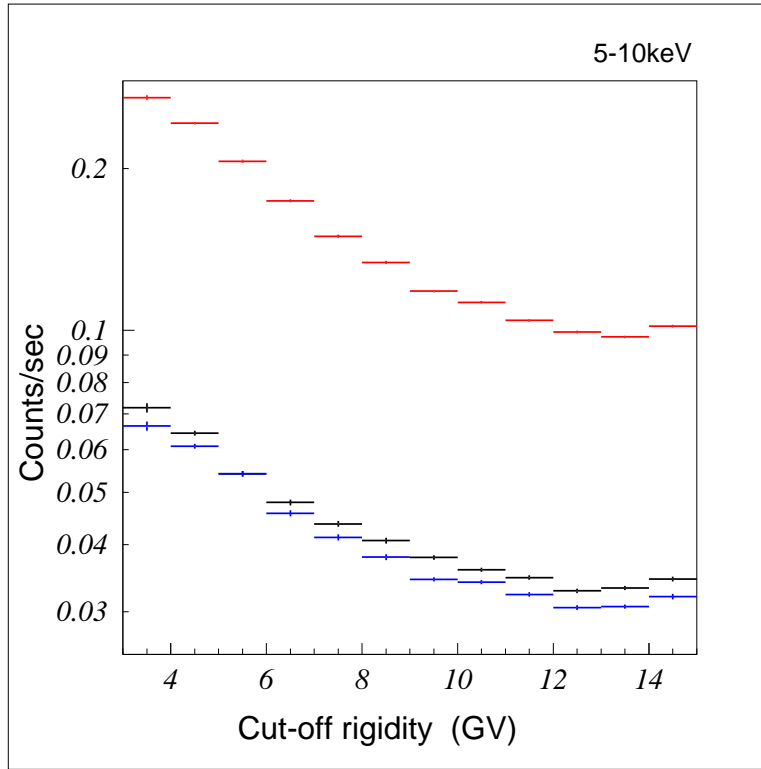


Figure 7.11: Cut-off rigidity dependence of the NXB (average intensity for 5–10 keV) for each sensor. The NXB flux varies by a factor of ~ 2 depending on the cut-off rigidity.

The count rate of the PIN upper discriminator (PIN-UD) in the HXD also correlates with the flux of the XIS NXB. Recent studies show the PIN-UD provides a slightly better reproducibility of the XIS NXB. The reproducibility of the NXB in the 5–12 keV band is evaluated to be 3–4% of the NXB, when we use the PIN-UD as the NXB sorting parameter (Tawa et al. 2008).

When we estimate the telemetry occupation of the background, we need to consider not only the X-ray grades (the ASCA grade 0, 2, 3, 4, 6) but also the non-X-ray grades (the ASCA grade 1, 5, 7). Although the class discriminator removes a large fraction of the non-X-ray background, we still have a non-negligible flux of the background. The background rate on the FI chips (including all the grades) is normally less than 10 counts/s and that of the BI CCD is less than 20 counts/s. These values represent the 90% upper limits of variations in the background count rates when the class discriminator is applied. These background rates are important when evaluating the possibility of the telemetry saturation at the low data rates (see section 7.9.4).

Table 7.3: Major XIS Background Emission Lines (Tawa et al. 2008).

Line	Energy [keV]	XIS0 [10^{-9} cps/pix]	XIS1 [10^{-9} cps/pix]	XIS2 [10^{-9} cps/pix]	XIS3 [10^{-9} cps/pix]
Al $K\alpha$	1.486	1.45 ± 0.11	1.84 ± 0.14	1.41 ± 0.10	1.41 ± 0.10
Si $K\alpha$	1.740	0.479 ± 0.081	2.27 ± 0.15	0.476 ± 0.080	0.497 ± 0.082
Au $M\alpha$	2.123	0.63 ± 0.093	1.10 ± 0.13	0.776 ± 0.097	0.619 ± 0.092
Mn $K\alpha$	5.895	6.92 ± 0.19	0.43 ± 0.14	1.19 ± 0.13	0.76 ± 0.11
Mn $K\beta$	6.490	1.10 ± 0.11	0.26 ± 0.13	0.40 ± 0.11	0.253 ± 0.094
Ni $K\alpha$	7.470	7.12 ± 0.19	7.06 ± 0.37	8.01 ± 0.20	7.50 ± 0.20
Ni $K\beta$	8.265	0.96 ± 0.10	0.75 ± 0.22	1.16 ± 0.11	1.18 ± 0.11
Au $L\alpha$	9.671	3.42 ± 0.15	4.15 ± 0.49	3.45 ± 0.15	3.30 ± 0.15
Au $L\beta$	11.51	2.04 ± 0.14	1.93 ± 0.48	1.97 ± 0.14	1.83 ± 0.14

The count rates are obtained from the whole CCD chip excluding regions irradiated by the calibration source. Errors are at the 90% confidence level.

7.9 XIS Observations

7.9.1 Photon Pile-Up

The XIS is essentially a position-sensitive integrating instrument, with a nominal interval of 8 s between readouts. If during the integration time more than one photon strikes the same CCD pixel, or one of its immediate neighbors, these cannot be correctly detected as independent photons; this is the phenomenon of photon pile-up. Here, the modest angular resolution of the *Suzaku* XRT is an advantage. However, photon pile-up could be a problem when observing bright sources.

If pile-up occurs, both image and spectral data are distorted. The energy spectrum tends to become harder for the following reason. In most cases, the soft photon flux is much larger than the hard photon flux. This means that, when pile-up occurs, soft photons tend to pile up rather than the hard photons. When soft photons pile up, they may be either discarded as a non-X-ray event or regarded as a single hard photon. This results in a flux decrease in the soft band and a flux increase in the hard band, which results in the spectral hardening. Because the decrease of the soft photons overwhelms the increase of the hard photons, the pile-up tends to decrease the total photon flux. In an extreme case, all events may be discarded as non-X-ray events at the image center, and the local photon flux becomes effectively zero. This means that a point source image would have a hole at the center. This is the simplest method to detect photon pile-up.

The impact of pile-up on the energy spectrum is different from source to source. For

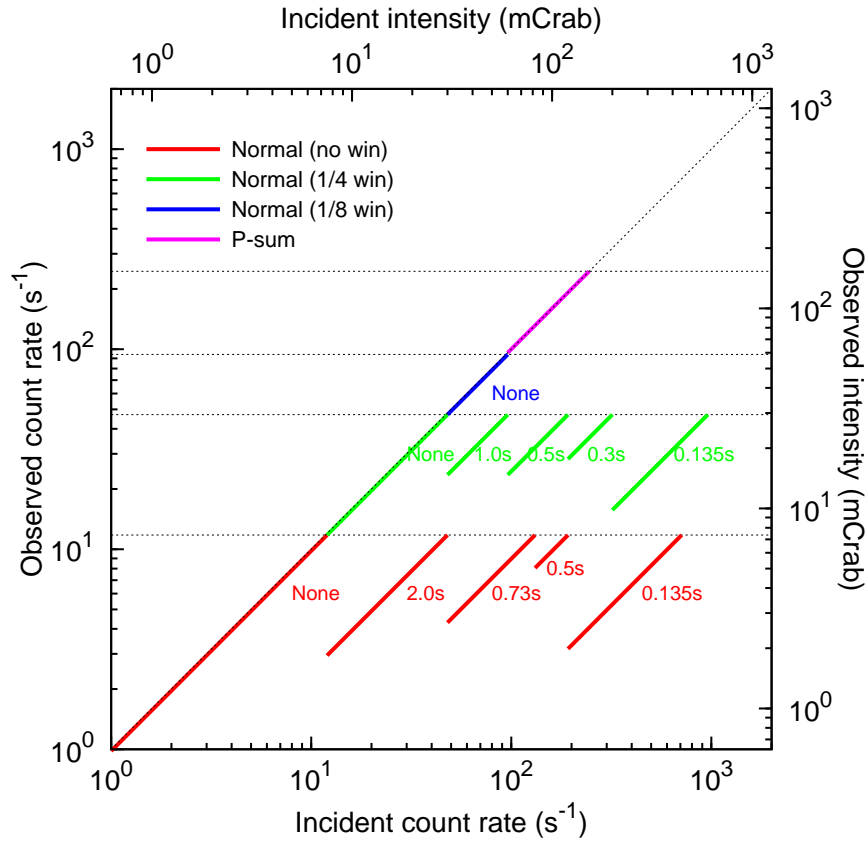


Figure 7.12: Incident vs observed count rates of a point source for the FI sensor. The color thick lines show the range that we can observe without the pile-up.

example, if one tries to look for a weak hard tail in the energy spectrum from a soft source, photon pile-up has to be strictly removed as it can easily mimic the hard tail. On the other hand, a heavily absorbed source with a hard spectrum may be rather insensitive to photon pile-up. Therefore guest observers should be aware of the impact of pile-up on their scientific goals, if they plan to observe bright objects.

Pile-up could be a problem when observing a bright point source but it's usually not if the object extended more than the point spread function of the XRT. However, photon pile-up can be avoided by selecting a Clock mode with some options in many cases. A detailed estimation is given below, but the results can be summarized as follows: In practice, point sources with < 12 counts/s can be observed in the Normal mode without any options (Full Window). If point sources have counting rates larger than 12 counts/s, guest observers should first consider to observe the targets at the HXD nominal position rather than the

Table 7.4: Total count rate which causes the indicated fraction of pile-up at the annulus of the PSF.

Radius [pix] ¹	Pile-up fraction		
	3%	20%	50%
~5	13.4	30.0	45.9
5~10	17.6	43.3	67.7
10~15	25.6	64.3	101
15~20	33.8	85.4	134
20~25	42.6	108	171
25~30	55.8	142	224
30~35	70.6	180	285
35~40	88.2	226	356
40~45	100	256	404
45~50	119	304	480
50~55	141	362	571

Note: in units of counts/s.

¹1 pixel = 1.04 arcsec.

XIS nominal position; the change of the aim point would decrease the counting rates by 10%. If changing the aim point is not enough, guest observers should think of window and/or the burst options. Unfortunately, point sources with >710 counts/s cannot be observed by the XIS without pile-up. Fig. 7.12 shows the range of the incident counting rate that we can observe without pile-up.

A detailed calculation of photon pile-up is given in Table 7.4. In this table, we summarize the estimated count rates at which the pile-up fraction in an annulus reaches 3, 20, and 50%. For example, for a source with the expected count rate of ~ 50 counts/s, > 50% of the events within ~ 5 pixels of the image center are piled up. On the other hand, the pile-up fraction is restrained to below 20% outside the circle of 15 pixels in radius. Note that the attitude fluctuation of the satellite does not mitigate the photon pile-up, because the attitude drift is negligible within the exposure of 8 s.

Recently, it was found that the fraction of the ASCA grade 1 event shows a good correlation with the pile-up fraction. Guest observers can check the significance of the pile-up in their data by studying the fraction of the ASCA grade 1 event. For more details, see the document on the Suzaku web page⁴.

When pile-up occurs, the effects need to be removed in the course of the data analysis. The most simple method is to remove the image center from the event extraction region. This means that the events are extracted from an annular region to calculate the energy spectra. In this case, an appropriate ARF file needs to be calculated depending on the

⁴http://www.astro.isas.jaxa.jp/suzaku/analysis/xis/HowToCheckPileup_v1.pdf

inner and outer radius of the annulus.

7.9.2 Out-Of-Time Events

X-ray photons detected during the frame-store transfer do not correspond to the true image, but instead appear as a streak or blur in the readout direction. These events are called out-of-time events, and they are an intrinsic feature of the CCD detectors. Similar streaks are seen from bright sources observed with *Chandra* and *XMM-Newton*. The out-of-time events produce a tail in the image, which can be an obstacle to detecting a low surface brightness feature in an image around a bright source. Thus the out-of-time events reduce the dynamic range of the detector. Since the XIS spends 25 ms (without the SCI) or 156 ms (with the SCI) in the frame-store transfer, about 0.3% ($= 0.025/8 \times 100$, without the SCI) and 2.0% (with the SCI) of all events will be out-of-time events. However, because the orientation of the CCD chip is different among the sensors, one can in principle distinguish a true feature of low surface brightness and the artifact due to the out-of-time events by comparing the images from two sensors or more.

7.9.3 Day Earth Contamination

When the XIS field of view is close to the day Earth (i.e., Sun-lit Earth), fluorescent lines from the atmosphere contaminate the low-energy part of the XIS data, especially in the BI chip. Most prominent is the oxygen line, but the nitrogen line may also be noticed. These lines are mostly removed when we apply the standard data screening criteria (XIS FOV is at least 20 degrees away from the day Earth) during the ground processing. However, the flux of the atmospheric fluorescent lines is more or less variable and could become rather large depending on the solar activity.

A small amount of contamination could remain after the standard data screening. Even in this case, the lines may be removed if we subtract background extracted in the same XIS field of view. If background data from other observations or the background database are used, the background subtraction may not completely eliminate the atmospheric lines. In this case, the data screening criterion, i.e., 20 degrees from the day earth, may need to be changed.

7.9.4 Telemetry Limit

If a large number of events is detected in a frame, only a part of the events is output to the telemetry. The data which cannot be output to the telemetry are discarded. This phenomenon is called telemetry saturation.

The current telemetry allocation among the XRS/XIS/HXD detectors is summarized in Table 7.5. Although the XRS is not functioning, a small amount of telemetry is allocated to

monitor its HK data. The ratio depends on the data rate and may be changed in the future. Due to staffing constraints, the available telemetry is slightly lower over the weekend. The “High” telemetry rate is always 144 kbits/s, but the “Medium” rate is 60 kbits/s during the week and 25 kbits/s over the weekend. Therefore, the mission operation team tries not to allocate observation time of bright sources on the weekend.

Table 7.5: Telemetry allocation (kbit/s).

Data rate	Weekday (XRS/XIS/HXD)	Weekend (XRS/XIS/HXD)
Superhigh	10/144/66	—
High	10/144/66	—
Medium	1/60/40	1/25/40
Low	1/15/10	1/1/10

Since the on-board XIS data are processed in units of eight seconds in accordance with the standard exposure time, the available telemetry per sensor is 44236 bytes for the “High” data rate, 18432 bytes for the “Medium (weekday)” data rate, and 7680 bytes for the “Medium (weekend)” data rate. Here we assume a distribution of telemetry allocation among the 4 sensors as XIS0:XIS1:XIS2:XIS3 = 3:3:1:3. We restricted the telemetry output of the XIS2 after the onset of the XIS2 trouble. The HK data and the frame header occupy a constant fraction of the telemetry, and the rest is allocated to the X-ray events.

In Table 7.6 the typical size of an event is shown for each Editing mode. Because the event is slightly compressed on board, the event sizes listed in the table should be regarded as representative values. The event compression efficiency depends on the grades of the events, i.e., on the spectral shape of the source.

Table 7.7 shows the maximum counting rates limited by the telemetry of the XIS. When the Suzaku operation team plans XIS observations, they should take into account the background rate (~ 10 counts/s for FI, ~ 20 counts/s for BI). Furthermore, the frame header and the HK data are also transferred to the telemetry. Therefore the operation team should take a margin of ~ 10 – 20% in the telemetry; the estimated total counting rate should be less than ~ 80 – 90% of the telemetry limits.

Table 7.6: Typical event size after compression [byte].

Edit mode	Minimum	Maximum	Average
5×5	28	52	40
3×3	15	23	19
2×2	8	11	9
Timing	4	4	4

Table 7.7: Maximum counting rates for avoiding telemetry saturation [counts/s/XIS].

Data rate	5×5	3×3	FI 2×2 & BI 3×3		timing
	(FI, BI)	(FI, BI)	(FI)	(BI)	(FI)
Superhigh	138	291	410	388	1382
High	138	291	410	388	1382
Medium (weekday)	58	121	171	162	576
Medium (weekend)	24	51	71	67	240
Low (weekday)	14	30	43	40	144
Low (weekend)	1	2	3	3	10

Note (1): The telemetry distribution among the four sensors was changed from equal distribution after the onset of the XIS2 trouble. Here XIS0:XIS1:XIS2:XIS3 = 3:3:1:3 is assumed, which has been used as nominal distribution since Dec. 20, 2006. However, when the FI sensors are operated in the 2×2 mode and the BI sensor is operated in the 3×3 mode, the PPU ratio of XIS0:XIS1:XIS2:XIS3 = 1:1:2:1 is used.

Note (2): Normal Clocking mode and no options are assumed.

Note (3): These values are absolute limits. When the Suzaku operation team plan XIS observations, they should take into account the background rate (~ 10 counts/s for FI, ~ 20 counts/s for BI). Furthermore, they should take a margin of ~ 10 – 20% in the telemetry; the estimated total counting rate should be less than ~ 80 – 90% of the telemetry limits.

7.10 Clock/Editing Mode Selection

Guest observers can select the XIS Clock mode and the options by considering the scientific goals, the counting rates of their targets, and photon pile-up. For diffuse sources which are more extended than the angular resolution of the XRT, photon pile-up is usually not a concern.

According to the XIS Clock mode and the options specified by the guest observers, the Suzaku operation team selects the Editing mode by considering the telemetry limit. In the case of extended objects where we do not need to care about pile-up, the operation team can consult Table 7.7 to decide the Editing mode.

We summarize the maximum counting rate for avoiding pile-up when observing a point source in Table 7.8. Here we adopt 12 cts/s as the pile-up limit according to Fig. 7.12. However, as explained previously, the appropriate pile-up limit depends on the spectral shape of the source and the science goal of the observations. If pile-up needs to be avoided completely, one should consider using the Window option even if the source count rate is ~ 12 counts/s. For a source brighter than ~ 700 counts/s, it may be difficult to avoid photon pile-up and/or telemetry saturation. Guest observers who plan to observe very bright sources should consult with the *Suzaku* personnel at ISAS/JAXA or the NASA *Suzaku* GOF for the optimal observation mode.

Table 7.8: Maximum incident counting rate (Max CR) for avoiding pile-up, observational efficiency (Loss rate), and maximum observed counting rate (Max obs CR).

No window option				
Burst option (s)	Frame exp (s)	Max CR (cts/s)	Loss rate	Max obs CR (cts/s)
none	8.000	12.000	0.019	11.770
2.000	2.000	48.000	0.755	11.770
1.000		N/A		
0.730	0.730	131.507	0.910	11.770
0.500	0.500	192.000	0.939	11.770
0.300		N/A		
0.135	0.135	711.111	0.983	11.770
1/4 window option				
Burst option (s)	Frame exp (s)	Max CR (cts/s)	Loss rate	Max obs CR (cts/s)
none	2.000	48.000	0.072	44.527
2.000		N/A		
1.000	1.000	96.000	0.536	44.527
0.730		N/A		
0.500	0.500	192.000	0.768	44.527
0.300	0.300	320.000	0.861	44.527
0.135	0.135	711.111	0.937	44.527
1/8 window option				
Burst option (s)	Frame exp (s)	Max CR (cts/s)	Loss rate	Max obs CR (cts/s)
none	1.000	96.000	0.135	83.045
2.000		N/A		
1.000		N/A		
0.730		N/A		
0.500		N/A		
0.300		N/A		
0.135		N/A		

Note (1): Assuming a point-source observation with the Normal clocking mode.

Note (2): Loss rate includes the effect of the time for transferring the imaging area to the frame-store area (156 ms) in the SCI.

Note (3): Max obs CR includes the effect of the Loss rate.

7.11 In-Flight XIS Calibration

In this section, we summarize the current status of the XIS flight calibration. Because the calibration information is updated frequently, it is expected that the description in this section may become obsolete quite soon. The latest calibration information can be found on the *Suzaku* web pages. The XIS team has mainly been calibrating the 5×5 , 3×3 , and 2×2 data in the Normal mode, because those are the most frequently used modes. As of August 2009, the calibrations for the Window option have been conducted. However, the calibration of the Timing mode remains very preliminary. Since the introduction of the SCI changes the XIS performance considerably, the XIS team is also working on the recalibration of the SCI data.

In the following, we describe the current status of the on-board calibration. The calibration items are as follows: (1) charge transfer efficiency (CTE), (2) energy scale, (3) energy resolution, (4) pulse height distribution function, (5) quantum efficiency in the low X-ray energy band (contamination), and (6) quantum efficiency in the high X-ray energy band.

7.11.1 Charge Transfer Efficiency & Energy Scale

The CTE is decreasing since the launch of *Suzaku* due to irradiation by charged particles on-orbit. In other words, the charge transfer inefficiency (CTI), defined as $1 - \text{CTE}$, is increasing. We continuously measure the central energy and the FWHM of the main peak from the two ^{55}Fe calibration sources. These calibration sources illuminate the CCD segments A and D at the far corners from the read-out nodes. Fig. 7.13 shows the on-orbit time history of the apparent central energy of the main peak. The linear trend is due to charge loss caused by the gradual decrease of the CTE.

We measured the CTE with the observations of the Galactic Center region, the Perseus galaxy cluster, the Cygnus loop, and 1E0102–72 as well as the calibration source ^{55}Fe . Since these X-ray sources are extending over the FOV of the XIS and have strong emission lines, they are suitable for the calibration of the CTE as a function of distance from the read-out node. Fig. 7.14 shows the time history of the CTE-corrected central energy of Mn K α .

The SCI has been applied to observations by default since we verified its performance on August 2006, when the central energy of the ^{55}Fe calibration sources was improved almost to its theoretical value without any corrections.

The absolute energy uncertainty measured with the ^{55}Fe calibration sources is within $\pm 0.2\%$, and that for the energy band below 1 keV is within $\pm 5\text{eV}$, as measured with 1E0102–72. As of writing, the calibration around $\sim 2\text{keV}$, including the silicon edge, still shows some uncertainties. These are the main uncertainties in the energy scale calibration.

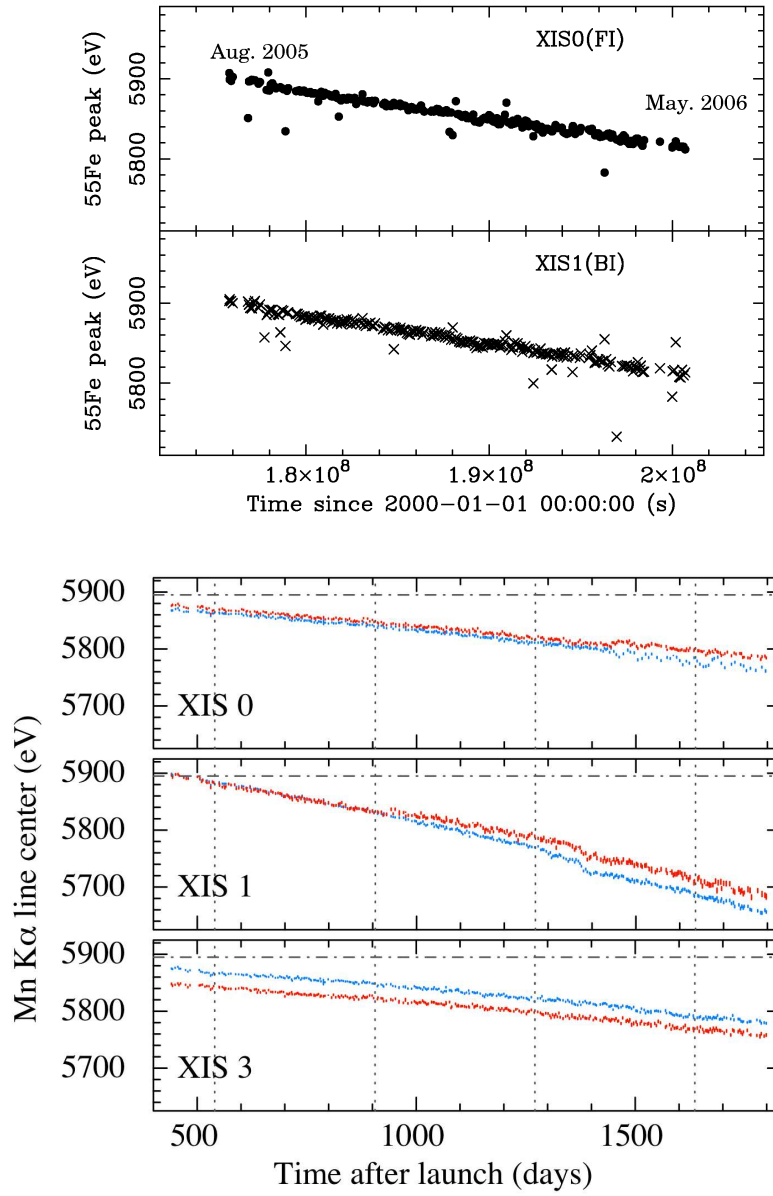


Figure 7.13: Time history of the central energy of the Mn K α line from the ^{55}Fe calibration sources without the CTE correction. The upper panels show the data before the SCI was turned on and the lower panels show those after. In the lower panels, blue and red symbols indicate segment A and D data, respectively.

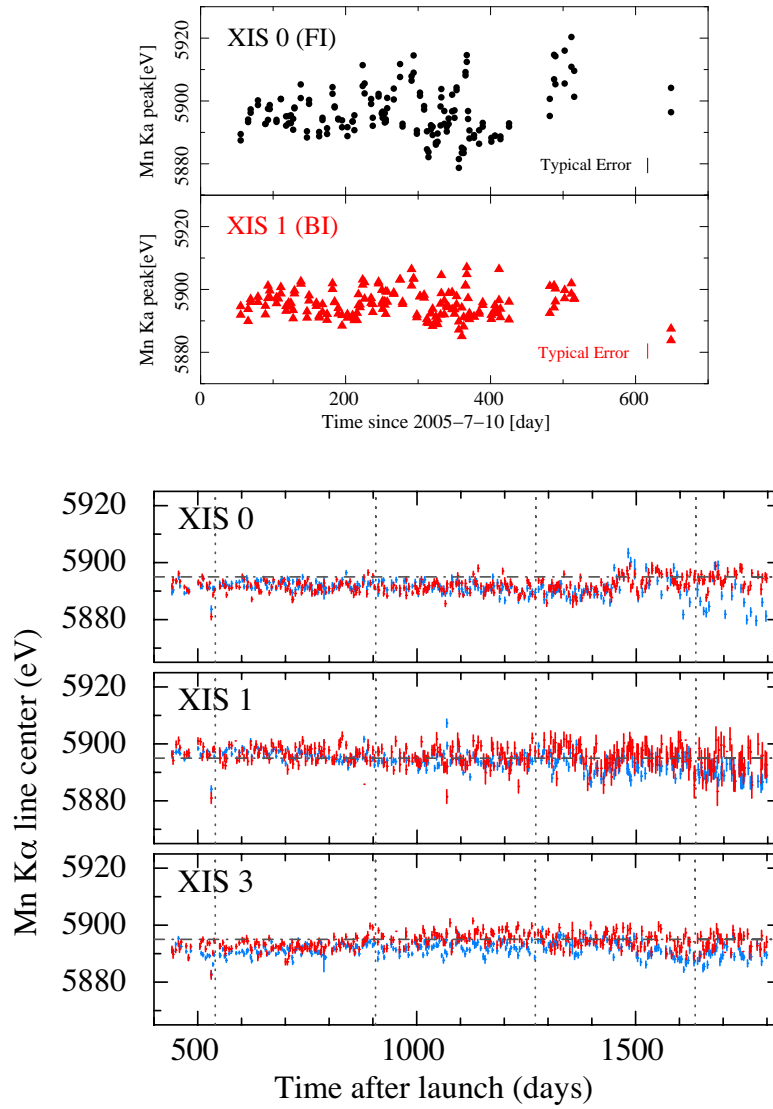


Figure 7.14: Time history of the CTE-corrected central energy of the Mn $K\alpha$ line from the ^{55}Fe calibration sources. The upper panels show the data before the SCI was turned on and the lower panels show those after. In the lower panels, blue and red symbols indicate segment A and D data, respectively.

7.11.2 Energy Resolution & Pulse Height Distribution Function (Full Window)

The calibration of the degradation of the energy resolution with time is done with the ^{55}Fe calibration source and the observations of E0102–72, and is verified with the data of

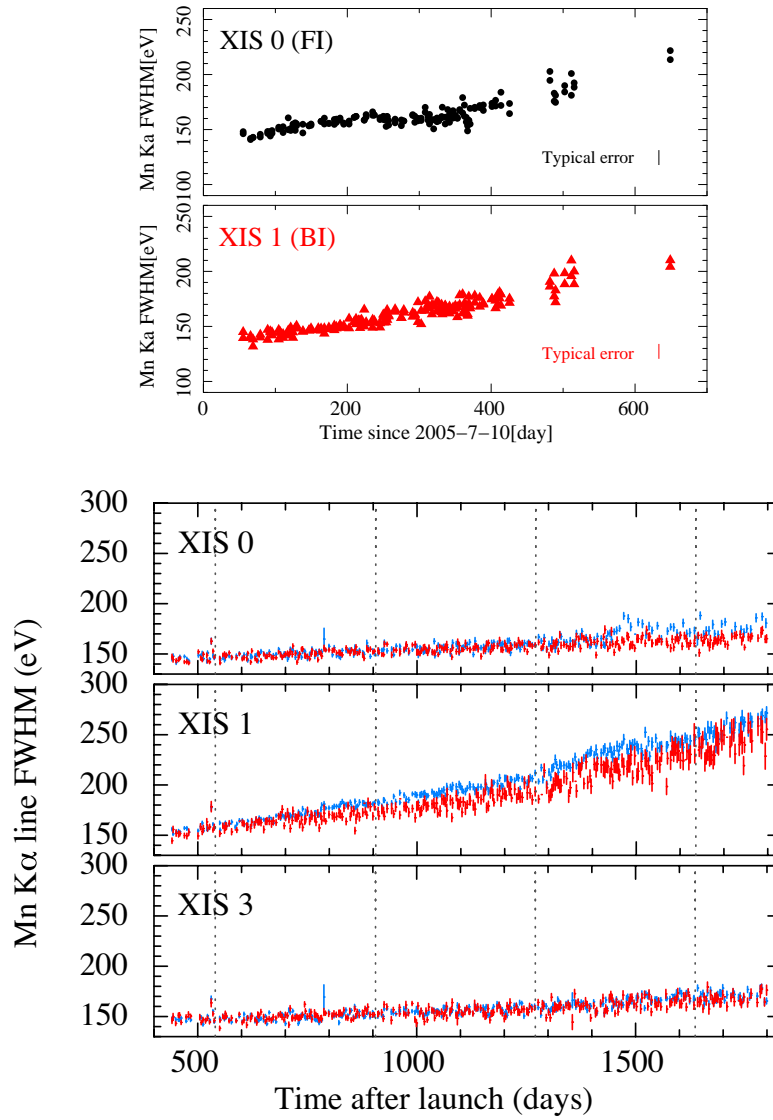


Figure 7.15: Time history of the energy resolution of Mn $K\alpha$ from the ^{55}Fe calibration sources after the CTE correction. The upper panels show the data before the SCI was turned on and the lower panel shows those after. In the lower panel, blue and red data symbols indicate segment A and D data, respectively.

the Galactic Center region and the Cygnus loop. Fig. 7.15 shows the time history of the energy resolution of the main peak of the Mn $K\alpha$ line from the calibration source. Fig. 7.16

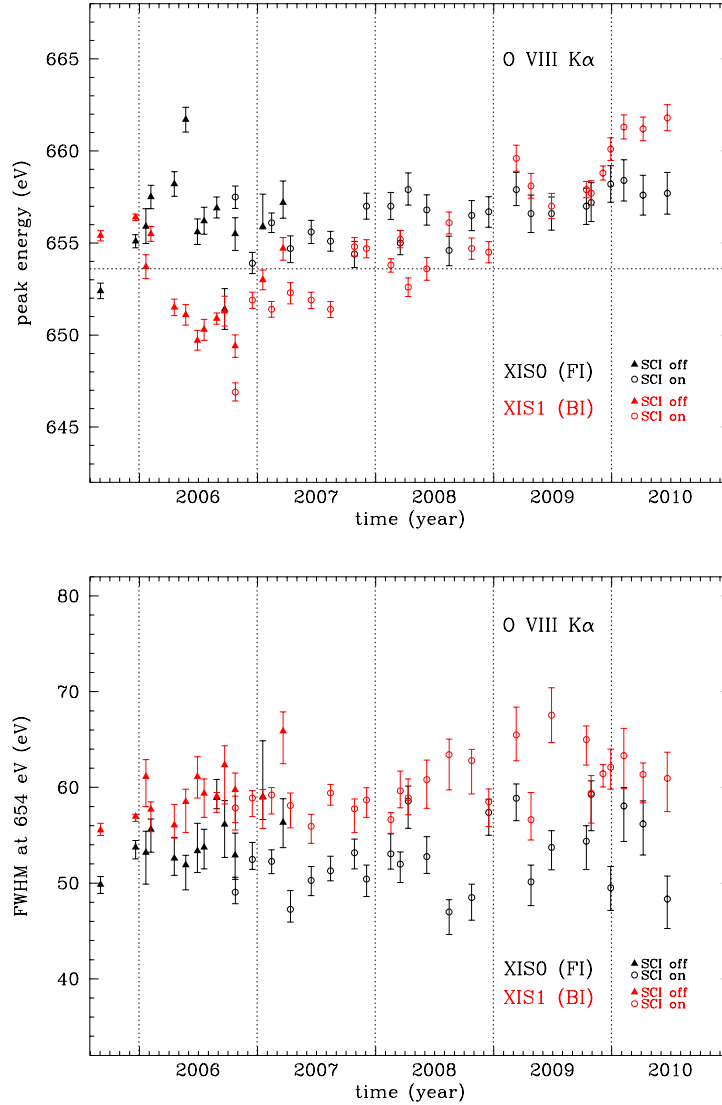


Figure 7.16: Time history of the center energy (upper panel) and width (lower panel) of the O VIII K α line (~ 0.65 keV) after the CTE correction for XIS0 (FI) and XIS1 (BI).

shows the time history of the width of the O VIII K α line (~ 0.65 keV) obtained from the 1E0102–72 data.

The evolution of the XIS energy resolution, $\Delta E(E_X, t)$, over time can be expressed by

the following formula,

$$\Delta E(E_X, t) = \sqrt{a(t) + b(t)E_X + c(t)E_X^2},$$

where E_X is the incident X-ray energy. The time variable parameters $a(t)$, $b(t)$ and $c(t)$ are determined from the ^{55}Fe and E0102–72 data mentioned above. The positional dependence of the energy resolution is negligibly small at present, compared to the accuracy of its determination.

Column-to-column variations of the CTE contribute much to the degradation of the energy resolution (Ozawa et al. 2009). In the case of the no-SCI mode, the CTE of each column has been measured using the checker flag charge injection (Nakajima et al. 2008; Ozawa et al. 2009). Thus, the CTE can be corrected for each column. However, the checker flag charge injection has not been conducted in the SCI mode, because the operation is too complicated. Segment-averaged CTE values are used in the SCI mode. The degradation of the energy resolution is taken into account by the RMF. Guest observers can create the appropriate RMF for their observations using `xisrmfgen`. The XIS team does not expect to change the pulse height distribution function (line profile response to monochromatic X-rays) on-orbit, except for the energy resolution. Results from pre-flight ground experiments are used in `xisrmfgen`.

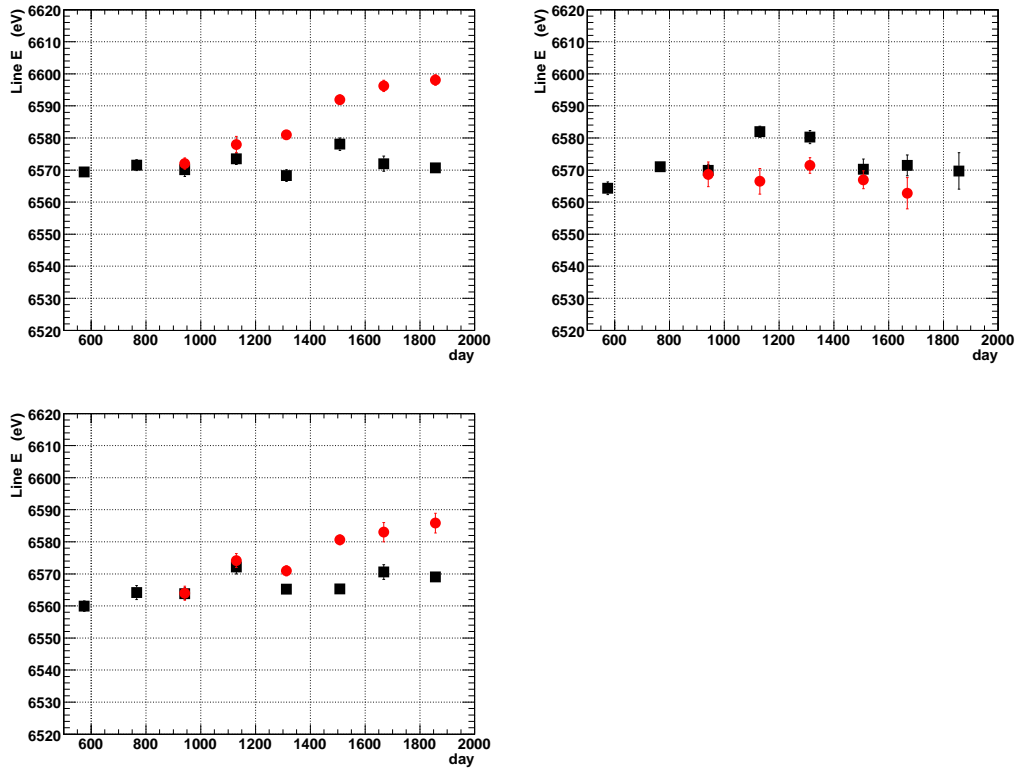


Figure 7.17: The gain uncertainty of the 1/4 window option is shown in comparison with the Normal mode without window option (top left: XIS0, top right: XIS1, bottom left: XIS3). Black and red indicate the Normal mode without and with the 1/4 window option, respectively, using a routine calibration observation of the Perseus cluster.

7.11.3 Energy Resolution & Pulse Height Distribution Function (Other)

The calibration uncertainties for window / burst option observations as well as the other clocking mode are potentially different from those for the Normal clocking mode, full window observations discussed above.

Window Option Figure 7.17 shows the gain uncertainty of the 1/4 window option shown as a comparison with the Normal mode without window option.

Burst Option Fig. 7.18 shows a spectral fit for data from the ^{55}Fe calibration source for a 2.0 s burst option observation using the RMF for the Normal mode. There is no structure in the residual, indicating that the response can be applied to burst mode observations.

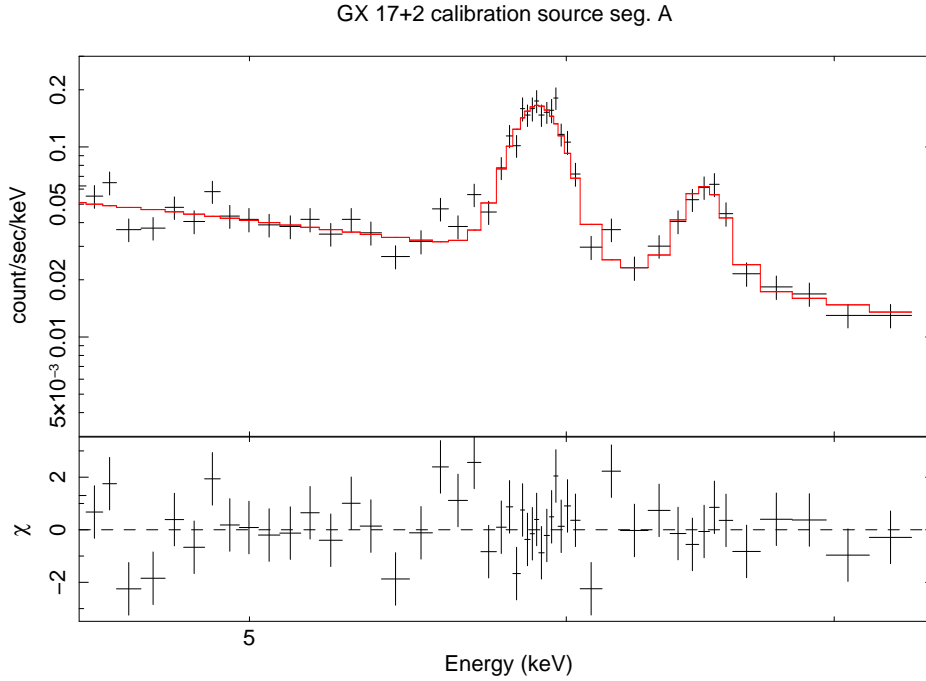


Figure 7.18: Mn I $K\alpha$ and $K\beta$ lines observed in a 2.0 s burst mode exposure of GX17+2. The spectrum is fitted with a continuum plus two Gaussian lines using the response generated for data taken with no burst option.

P-sum Mode The calibration of the P-sum mode is more challenging than that of the Normal mode with window and/or burst option. The change of spectroscopic performance is more rapid due to the lack of the availability of the SCI technique. Figure 7.19 shows the history of phenomenological gain of the P-sum mode data. Figure 7.20 shows the energy resolution for a representative line in the soft and the hard band. A recipe for the reduction of P-sum data is available at http://www.astro.isas.jaxa.jp/suzaku/analysis/xis/psum_recipe/Psum-recipe-20100724.pdf.

7.11.4 Quantum Efficiency

Contamination is the main issue for the calibration of the quantum efficiency in the low X-ray energy band. The status of the calibration is described in section 7.7. The calibration of the quantum efficiency above $\sim 1 - 2$ keV is mainly done with Crab nebula observations. The current status is given in chapter 6.

The stability of the relative flux normalization between the three XIS sensors is shown in Fig. 7.21. No significant time dependence is found. The relative normalization remains

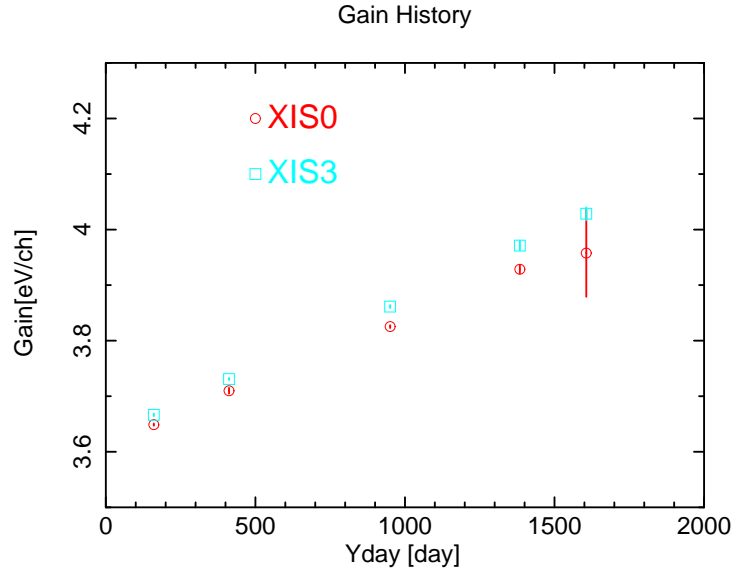


Figure 7.19: Time history of the P-sum mode gain.

Table 7.9: Relative flux normalization between different sensors.

Position	Ratio	Mean	Standard deviation
XIS-norm	XIS1/XIS0	1.026	0.016
	XIS3/XIS0	1.014	0.017
HXD-norm	XIS1/XIS0	1.004	0.019
	XIS3/XIS0	0.980	0.022

constant. The mean and standard deviation are summarized in Table 7.9, separately for the XIS and HXD nominal positions.

7.12 Putative Micro-Meteorite Hits

Over time, sudden anomalies occurred in XIS0, XIS1, and XIS2. The entire XIS2 was lost. A part of the XIS0 is lost, which is masked by area discrimination since then. XIS1 remains intact. Although the cause of the anomalies are not known, micro-meteorite impacts are suspected.

The XIS2 anomaly suddenly occurred on Nov. 9, 2006, 1:03 UT. About 2/3 of the image was flooded with a large amount of charge, which had leaked somewhere in the imaging region. When the anomaly occurred, the satellite was out of the SAA and the XIS sensors were conducting observations in the Normal mode (SCI on, without any options).

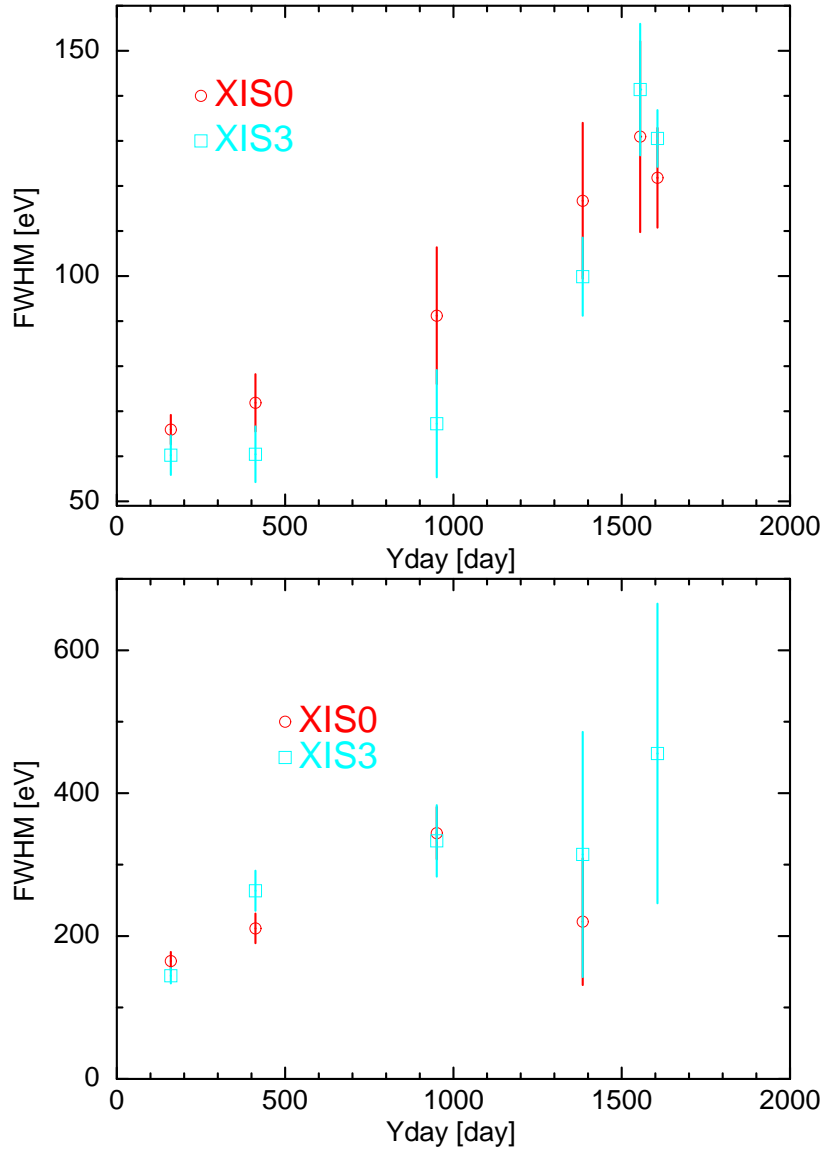


Figure 7.20: Time history of the P-sum mode energy resolution. The upper panel shows the change for the Ne IX $K\alpha$ line, whereas the lower panel shows the change for the Mn I $K\alpha$ line.

We carried out various tests to check the condition of XIS2, and found that (1) the four readout nodes of the CCD and the corresponding analog chains were all working fine, (2) the charge injection was not directly related to the anomaly, but may have helped to spread the leaked charge. When we changed the clock voltages in the imaging region,

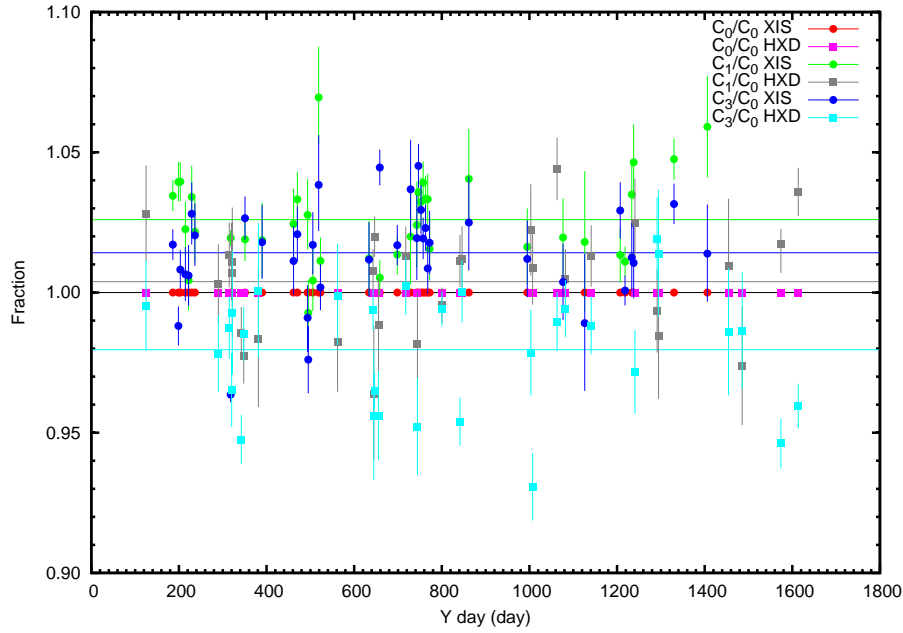


Figure 7.21: Relative flux normalization between different sensors. The ratio of the best-fit normalization values are compared between two sensors at the XIS and the HXD nominal positions. Observations of a power-law source in the Normal clocking mode were used. The best-fit constant values are indicated by solid lines.

the amount of leaked charge changed. This indicates a short between the electrodes and the buried channel. Possible mechanisms to cause the short include the micro-meteorite impact on the CCD, as seen, e.g., on *XMM-Newton* and *Swift*. Although there is no direct evidence to indicate the micro-meteorite impact, the phenomenon observed in XIS2 is not very different from that expected from the micro-meteorite impact. The low-earth orbit and the low-grazing-angle mirrors of *Suzaku* may have enhanced the probability of such an event.

We tried to reduce the leaked charge by changing the clock pattern and voltages in the imaging region. However, the attempt was not successful. Therefore it was decided to stop operating the sensor. It is unlikely that operation of the XIS2 will be resumed in the future.

For the anomalies of XIS0 and XIS1, detailed information can be found in the *Suzaku* memos available at <http://www.astro.isas.ac.jp/suzaku/doc/suzakumemo/>.

7.13 XIS References

1. Bautz, M. et al. 2004, Proc. of SPIE, 5501, p111 “Progress in x-ray CCD sensor performance for the Astro-E2 X-ray imaging spectrometer”
2. Ishisaki et al. 2007, PASJ, 59, S113
“Monte Carlo Simulator and Ancillary Response Generator of Suzaku XRT/XIS System for Spatially Extended Source Analysis”
3. Koyama, K. et al. 2007, PASJ, 59, S23
“X-Ray Imaging Spectrometer (XIS) on Board Suzaku”
4. Nakajima, H. et al. 2008, PASJ, 60, S1
“Performance of the Charge-Injection Capability of Suzaku XIS”
5. Ozawa, M. et al. 2009, PASJ, 61, S1
“Energy-Scale Calibration of the Suzaku X-Ray Imaging Spectrometer Using the Checker Flag Charge Injection Technique in Orbit”
6. Tawa, N. et al. 2008, PASJ, 60, S11
“Reproducibility of Non-X-Ray Background for the X-Ray Imaging Spectrometer aboard Suzaku”
7. Tsujimoto, M., et al. 2010, A&A, in press
“Cross-calibration of the X-ray Instruments onboard the Chandra, INTEGRAL, RXTE, Suzaku, Swift, and XMM-Newton Observatories using G21.5–0.9”
8. Uchiyama, H. et al. 2009, PASJ, 61, S9
“New CTI Correction Method for the Spaced-Row Charge Injection of the Suzaku X-Ray Imaging Spectrometer”

Chapter 8

Hard X-Ray Detector (HXD)



Figure 8.1: The Hard X-ray Detector before installation.

The Hard X-ray Detector (HXD, see Figure 8.1) is a non-imaging, collimated hard X-ray scintillating instrument sensitive in the ~ 10 keV to ~ 600 keV band. It has been developed jointly by the University of Tokyo, Aoyama Gakuin University, Hiroshima Uni-

versity, ISAS/JAXA, Kanazawa University, Osaka University, Saitama University, SLAC, and RIKEN. Its main purpose is to extend the bandpass of the *Suzaku* observatory to the highest feasible energies, thus allowing broad-band studies of celestial objects.

This AO-6 document is based on the latest calibration of the PIN and the GSO detectors as of October 2010 (HEASOFT 6.9 or later). The recommended procedure for feasibility simulations is basically unchanged, although new sets of response and background files have been provided.

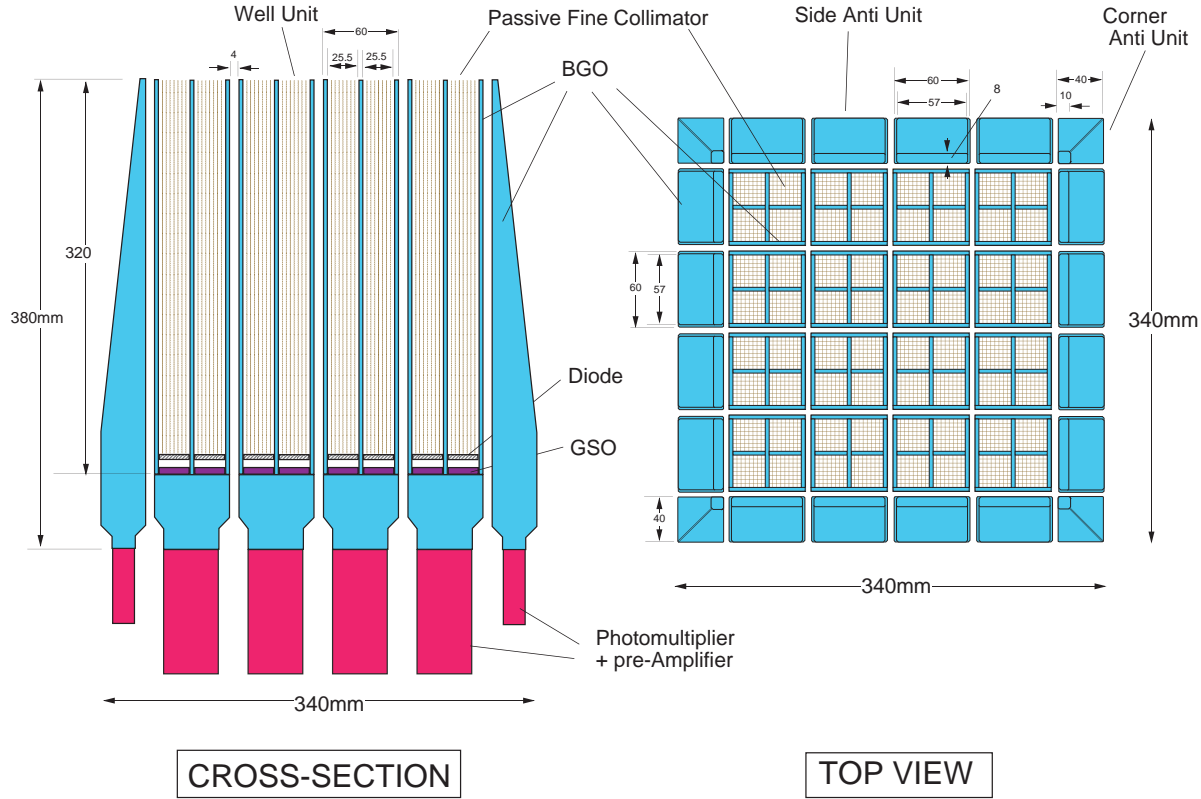


Figure 8.2: Schematic picture of the HXD instrument, which consists of two types of detectors: the PIN diodes located in the front of the GSO scintillator, and the scintillator itself.

The HXD sensor (HXD-S) is a compound-eye detector instrument, consisting of 16 main detectors (arranged as a 4×4 array) and the surrounding 20 crystal scintillators for active shielding. Each unit actually consists of two types of detectors: a GSO/BGO phoswich counter, and 2 mm-thick PIN silicon diodes located inside the well, but in front of the GSO scintillator. The PIN diodes are mainly sensitive below ~ 60 keV, while the GSO/BGO phoswich counter (scintillator) is sensitive above ~ 40 keV. The scintillator signals are read out by photomultiplier tubes (PMTs). A schematic drawing of the HXD

is given in Fig. 8.2. The HXD features an effective area of $\sim 160 \text{ cm}^2$ at 20 keV, and $\sim 260 \text{ cm}^2$ at 100 keV (Fig. 3.5). The energy resolution $\sim 4.5 \text{ keV}$ (FWHM) for the PIN diodes, and $7.6/\sqrt{E} \%$ (FWHM) for the scintillators, where E is energy in MeV. The HXD time resolution is $61 \mu\text{s}$.

8.1 GSO/BGO Counter Units

Each main detector unit is of a well-type design with active anti-coincidence shields. The shields and the coarse collimator itself are made of Bismuth Germanate (BGO, $\text{Bi}_4\text{Ge}_3\text{O}_{12}$) crystals, while the X-ray sensing material “inside the well” consists of Gadolinium Silicate (GSO, $\text{Gd}_2\text{SiO}_5(\text{Ce})$) crystals. The aspect ratio of the coarse collimators yields an acceptance angle for the GSO of 4.5° (FWHM). Each unit forms a 2×2 matrix, containing four $24 \text{ mm} \times 24 \text{ mm}$, 5 mm thick GSO crystals, each placed behind a PIN diode. BGO crystals are also placed underneath of the GSO sensors, and thus each well is a five-sided anti-coincidence system. The effective thickness of the BGO active shield is about 6 cm for any direction from the PIN and GSO, except for the pointing direction.

The reason for the choice of the two different crystals for the sensor and the shield is dictated by the large stopping ability of both, yet the very different rise/decay times, of $\sim 700 \text{ ns}$ for BGO, and $\sim 120 \text{ ns}$ for GSO, at a working temperature of -20°C . This allows for an easy discrimination of the shield vs. X-ray sensor signals, where a single PMT can discriminate between the two types of scintillators in which an event may have occurred. Any particle events or Compton events that are registered by both the BGO and GSO can be rejected by this phoswich technique, utilizing custom-made pulse-shaping LSI circuits.

In early 2010, a new GSO gain calibration with associated response files has been released. With this update, GSO data become usable down to 50 keV. See the *Suzaku* web pages for more details ¹. Note that proposers do not need to consider the details of the new responses, since the differences to the old ones are minor with respect to performing feasibility simulations (although not negligible in a real data analysis).

8.2 PIN-Si Diodes

The low energy response of the HXD is provided by 2 mm thick PIN silicon diodes, placed in front of each GSO crystal. The geometrical area of the diodes is $21.5 \times 21.5 \text{ mm}^2$, while the effective area is limited to $\sim 16.5 \times 16.5 \text{ mm}^2$ by the guard ring structure. The temperature of the PIN diodes is controlled to be $-15 \pm 3^\circ \text{C}$ to suppress electrical noise caused by the leakage current, and they are almost fully depleted by applying a bias voltage

¹http://heasarc.gsfc.nasa.gov/docs/suzaku/analysis/gso_newgain.html and <http://www.astro.isas.jaxa.jp/suzakku/analysis/hxd/gsoarf2/>

of 400~500 V². The PIN diodes absorb X-rays with energies below ~ 70 keV, but gradually become transparent at harder X-rays, which reach and are registered by the GSO detectors. The X-rays are photoelectrically absorbed in the PIN diodes, and the signal is amplified, converted to digital form, and read out by the associated electronics. The PIN diodes are of course also actively shielded from particle events by the BGO shields, as they are placed inside the deep BGO wells. In addition, in order to reduce contamination by the cosmic X-ray background, passive shields called “fine collimators” are inserted in the well-type BGO collimator above the PIN diodes. The fine collimator is made of $50\text{ }\mu\text{m}$ thick phosphor bronze sheets, arranged to form 8×8 square meshes, 3 mm wide and 300 mm long, each.

The lower threshold of the PIN diodes has gradually become higher due to the increase of leakage current by cosmic-ray damage. Updated response files are regularly provided by the HXD team, for well defined “epochs” in time. As of October 2010, calibration epoch 9 is the newest/current one.

8.3 HXD Field of View

The field of view of the HXD changes with incoming energy. Below ~ 100 keV the passive fine collimators define a $34' \times 34'$ FWHM square opening as shown in Figure 8.3. The narrow field of view compared to the *Beppo-SAX*-PDS and *RXTE*-HEXTE experiments is one of the key advantages of HXD observations. Above ~ 100 keV the fine collimators become transparent and the BGO active collimator defines a $4.5^\circ \times 4.5^\circ$ FWHM square opening. In summary, the full PIN energy range and the lower quarter of the GSO range have a field of view of $34'$, while the GSO events above ~ 100 keV have a wider field of view, up to 4.5° .

8.4 In-Orbit HXD Background

Although the HXD is a non-imaging instrument, its instantaneous background can be reproduced through modeling, without requiring separate off-source observations. The HXD has been designed to achieve an extremely low in-orbit background ($\sim 10^{-4}$ cps cm^{-2} keV^{-1}), based on a combination of novel techniques: (1) the five-sided tight BGO shielding as mentioned above, (2) the use of the 20 shielding counters made of thick BGO crystals which surround the 16 main GSO/BGO counters, (3) sophisticated on-board signal processing and on-board event selection, employing both high-speed parallel hardware circuits in the analog electronics, and CPU-based signal handling in the digital electronics, and (4) the

²The bias voltage of one out of four high-voltage units has been reduced to 400 V since 2006 May 29, due to the in-orbit damage of a PIN diode. On October 3, 2006, another bias was also set to 400 V. In total, half of the PIN diodes are operated with a 400 V bias, and the other half with 500 V. This affected the total effective area of the PIN diodes on a $\sim 6\%$ level, only.

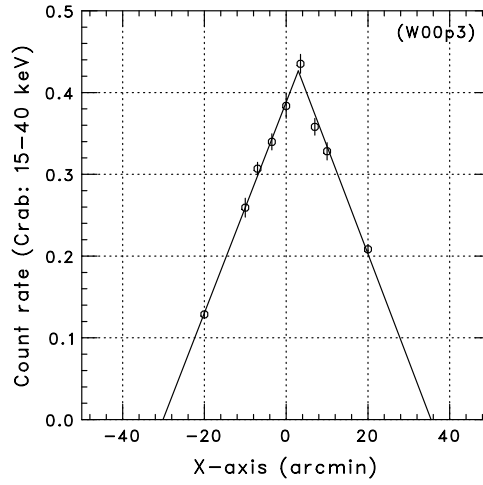


Figure 8.3: Angular response of a single fine-collimator along the satellite X-axis, obtained from offset observations of the Crab nebula.

careful choice of materials that do not become strongly activated under in-orbit particle bombardment. Finally, (5) the narrow field of view below ~ 100 keV defined by the fine collimator effectively reduces both the CXB contribution and the source confusion.

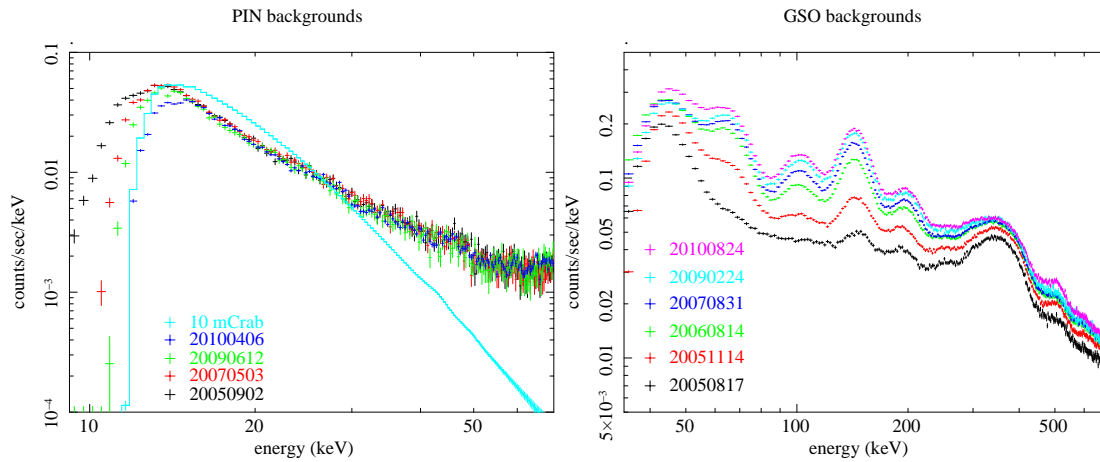


Figure 8.4: [Left] Comparison of average non X-ray background spectra of the PIN, obtained in various epochs. The Crab spectrum, scaled down by two orders of magnitude, is shown as well. [Right] Evolution of average GSO-NXB spectra.

The non X-ray background (NXB) of the PIN diodes, measured in orbit, is plotted in the left panel of Fig. 8.4. The average background count rate summed over the 64 PIN diodes is ~ 0.6 counts s^{-1} , which is roughly equal to an intensity of 10 mCrab. In addition,

almost no long-term growth has been observed in the PIN-NXB during the first three years of *Suzaku*, thanks to the small activation effect of silicon. In contrast, as shown in the right panel of Fig. 8.4, a significant long-term increase caused by in-orbit activation has been observed for the GSO-NXB, especially during the early phase of the mission. The background spectrum of the GSO contains several activation peaks, with intensities exponentially increasing with their half-lives. Since the longest half-life is about one year, the GSO-NXB level will have almost saturated in AO-6.

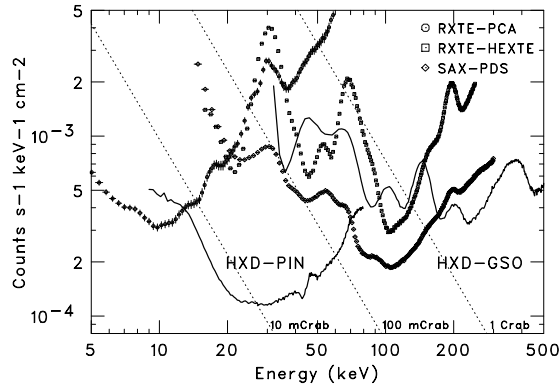


Figure 8.5: Comparison of the in-orbit detector background of the PIN/GSO as of AO-6, normalized by the individual effective areas, with that of the *RXTE*-PCA, *RXTE*-HEXTE, and *BeppoSAX*-PDS. Dotted lines indicate 1 Crab, 100 mCrab, and 10 mCrab intensities.

Figure 8.5 illustrates the comparison between detector backgrounds of several hard X-ray missions. The lowest background level per effective area is achieved by the HXD in an energy range of 12–70 and 150–500 keV. The in-orbit sensitivity of the experiment can be roughly estimated by comparing the background level with celestial source intensities indicated by dotted lines. Below 30 keV, the level is smaller than 10 mCrab, which means a sensitivity better than 0.3 mCrab can be obtained, if an accuracy of 3% is achieved in the background modeling.

Since the long-term variation of both PIN-NXB and GSO-NXB can be expected to be stable, the main uncertainties of the background come from temporal and spectral short-term variations. As shown in Fig. 8.6, the PIN-NXB displays significant short-term variability, with a peak-to-peak amplitude of a factor of 3, anti-correlated with the Cut-Off Rigidity (COR) over the orbit. Since the COR affects the flux of incoming primary cosmic-ray particles, most of the PIN-NXB is considered to originate in the secondary emission produced by interactions between cosmic-ray particles and materials surrounding the detector. When a selection criterion of $COR > 6$, a standard value used in the pipeline processing, is applied for the event extraction, the amplitude decreases to a factor of ~ 2 . During this temporal variation of the PIN-NXB, its spectral shape also changes slightly (larger deviations from the average are observed at a higher energy range, Kokubun et al.

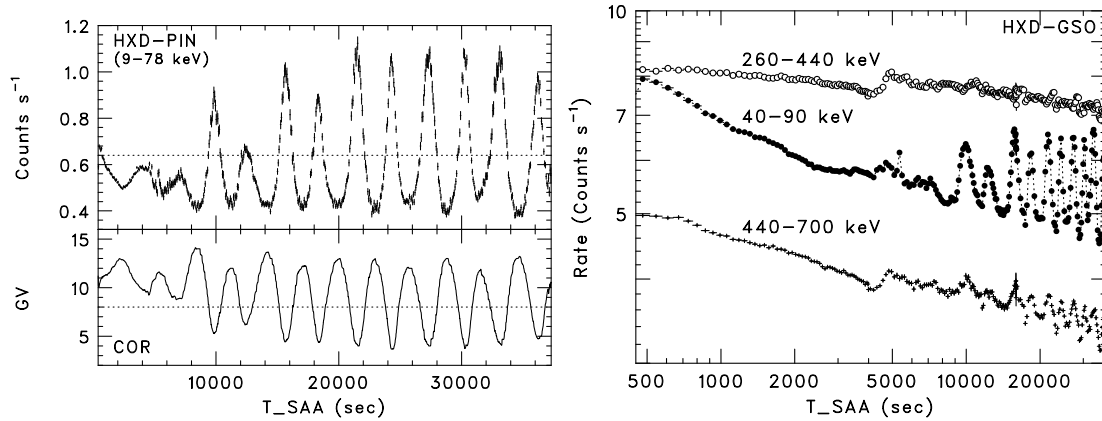


Figure 8.6: [Left] Light curve of the non X-ray background of the PIN, folded with the elapsed time after the SAA passage (*top*), and the average cut-off rigidity at the corresponding position (*bottom*). [Right] The same folded light curves for the GSO background, in the 40–90, 260–440, and 440–700 keV energy bands.

2007). In case of the GSO-NXB the temporal variation differs for different energy bands, as shown in the right panel of Fig 8.6. In the lowest energy range a rapid decline after the SAA passage is clearly observed, in addition to a similar anti-correlation with the COR. All these temporal and spectral behaviors have to be properly handled in the background modeling.

8.5 Background Modeling

As is the case for every non-imaging instrument (and in particular, for those sensitive in the hard X-ray range), the limiting factor for the sensitivity of the HXD is the reproducibility of the background estimation. Since this is the first space flight of an HXD-type detector, and the reproduction of the in-orbit background is not at all an easy task, the modeling accuracy evolves with the experience with in-orbit data. The latest status of the estimation procedures and their uncertainties will be regularly posted on the *Suzaku* web-sites listed in Appendix B. For the AO-6 proposal preparation methods, limitations, and reproducibilities (as a function of time-scale and energy range) of the current background modeling are briefly described below. Note that this document is based on “Suzaku-memo-2008-03” (Mizuno et al. 2008) and “Suzaku-memo-2008-01” (Fukazawa et al. 2008), which can be found at <http://www.astro.isas.jaxa.jp/suzaku/doc/suzakumemo>. We recommend that proposers properly take into account the expected uncertainties for their observation, based on the following information. Note that all uncertainties are reported at the 90% confidence level in this section.

8.5.1 PIN Background Model

Modeling Methods

Since there is a strong anti-correlation between the PIN-NXB and the COR, the background modeling of the PIN is primarily based on the count rate of high-energy charged particles, directly measured by the PIN diodes. Due to large energy deposits in the silicon, penetrations of cosmic-ray particles cause large signals in the corresponding PIN diodes. Hence they activate the Upper Discriminator (UD) in the analog electronics and are then recorded as PIN-UD monitor count in the HK data. The PIN-UD rate is considered to directly indicate the flux of primary cosmic-ray particles. The background count rate at any time can be generally estimated based on the corresponding PIN-UD rate.

In the actual modeling procedure of the so called “tuned-bgd”, the PIN-NXB rate is described by adding the raw PIN-UD rate and the integrated PIN-UD rate with a fixed decay time constant, to take into account the small effect of activation during SAA passages. In addition, several parameters such as GSO count rate, Earth elevation angle and cut-off rigidity, are included as input parameters.

The spectral shape of the PIN-NXB is assumed to depend on the COR and the elapsed time after the SAA passage. For each estimated rate it is extracted from a database of PIN-NXB spectra, which has been compiled from Earth occultation data.

Comparison With Sky Data

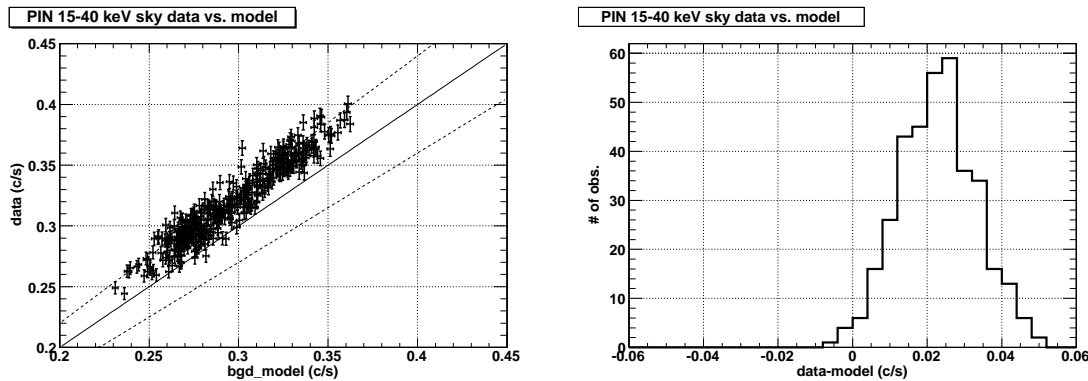


Figure 8.7: Comparison between the data and the NXB model count rate of sky observations with 10 ks integration time in the 15–40 keV band. Observations with no apparent hard X-ray objects in the XIS FOV were selected (see text for details of the data selection).

We first selected observations with no strong X-ray emission above 7 keV (less than 20% above the XIS-FI NXB in the entire XIS field-of-view) and compared the HXD-PIN

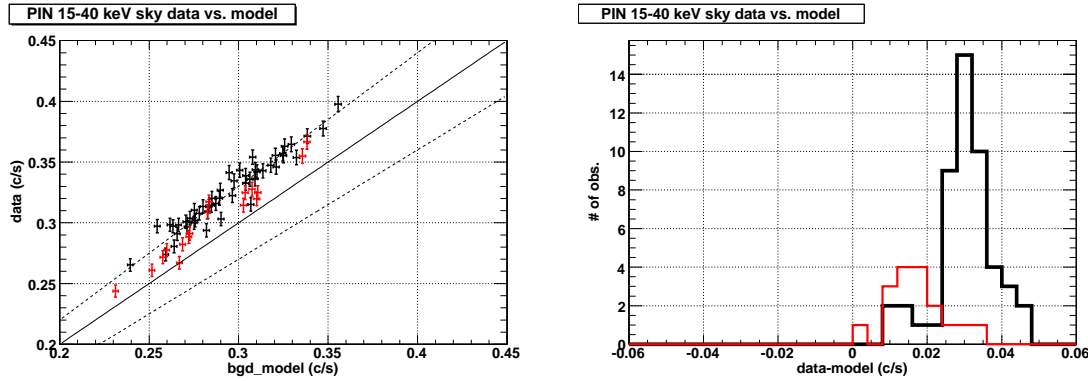


Figure 8.8: The same as Figure 8.7, but for observations of E0102-72 (black) and the Cygnus LOOP (red).

data and the NXB model count rate (10 ks exposure) in the 15–40 keV band, as shown in Figure 8.7. The 90% confidence region (including a statistical uncertainty of $\sim 3.3\%$) of the residual is 5.8% of the mean NXB count rate, which is larger than that obtained from the Earth occultation data ($\sim 3.8\%$ including 3.1% statistical uncertainty, see § 3.2 of “Suzaku-memo-2008-03”).

Figure 8.8 shows the same comparison of sky data and the NXB model for E0102–72 observations (the same sky region is observed regularly for XIS calibration purposes). Some observations do not satisfy the selection criteria using XIS due to sources or diffuse emission in the XIS field-of-view, but we used all E0102–72 observations in order to compare sky data and the NXB model for as big a data set as possible. We also plot the data and the NXB model for Cygnus LOOP multi-pointing observations (regions within a radius of 1.5 degrees were observed). We see a clear difference of the residual between the two sets of observations. Especially, the width of the residual for the E0102–72 data is much narrower than that seen in Fig. 8.7.

The 90% confidence region of the residual obtained from the E0102–72 observations is $\pm \sim 0.015 \text{ counts s}^{-1}$, or $\pm \sim 5\%$ of the mean NXB rate, including the statistical uncertainty of $\sim 3.3\%$. This is somewhat larger, but comparable to, the residual distribution of 3.8% (including the statistical uncertainty of 3.1%) obtained from Earth occultation data. After subtracting the statistical uncertainty, the residual systematic uncertainty of the E0102–72 observations is estimated to be 3.8%, for a typical 10 ks exposure. As described above, the E0102–72 data might suffer from contamination from sources within the field-of-view, and thus this confidence region should be regarded as a conservative estimate. For longer exposures the systematic uncertainty is expected to become a bit smaller, though the lack of long-exposure sample observations makes it difficult to verify this effect at the moment.

In order to check the NXB reproducibility for a sample of observations, we also investi-

gated the background subtraction for eight objects for which the source signal is expected to be negligible in the HXD-PIN. The spectra are summarized in Figure 8.9. The background-subtracted spectra and the CXB model of Boldt (1987)³ are displayed as blue and green histograms, respectively. No systematic difference between them is seen up to 60 keV.

From these arguments, it is clear that the *current* NXB model reproducibility at the 90% confidence level (excluding the statistical error) is better than 5%, and will be as good as 3% in most observations with exposures longer than 10 ks. When analyzing HXD data, the user should carefully estimate the reproducibility depending on the given observational conditions. For simplicity, we suggest to employ 3% as nominal value of the 15–40 keV PIN NXB reproducibility at the 90% confidence level for the preparation of AO-6 proposals (see, e.g., section 5.5.2).

8.5.2 GSO Background Model

Modeling Methods

The GSO background is higher than that of the PIN, and hence the background modeling accuracy is very important. The background model generation methods are similar to those applied for the PIN background.

Comparison With Dark Objects

We compared the NXB model with the on-source data of dark objects, for which the source signal is expected to be negligible in the HXD-GSO. Examples for the comparison of spectra for eight dark objects are summarized in Figure 8.10. Unlike for the PIN, the CXB is negligible in the GSO band. The overall spectral shape is similar between the data and the background model spectra, where the latter is solely based on a template derived from Earth occultation data. In most cases, the residuals amount to 1–1.5% of the data. For simplicity, we therefore suggest to employ 1.5% as nominal value of the GSO NXB reproducibility at the 90% confidence level for the preparation AO-6 proposals (see, e.g., section 5.5.2).

8.5.3 Theoretical Sensitivity

As a reference, Fig. 8.11 presents the theoretical sensitivity calculation results, that is, expected sensitivities defined by a certain systematic uncertainty of the background modeling, and those solely determined by the statistical uncertainty for a given exposure. In

³The spectral model is given by:
 $9.412 \times 10^{-3} \times (E/\text{keV})^{-1.29} \times \exp(-E/40 \text{ keV})$ [photons s⁻¹ cm⁻² keV⁻¹ FOV⁻¹]. For more details, see <http://heasarc.gsfc.nasa.gov/docs/suzaku/analysis/abc/node10.html>.

the plot, background reproducibility uncertainties of 3% and 1.5% are assumed as an example, for the PIN and the GSO, respectively. Since the actual statistical and systematic uncertainties that are to be expected for a proposed observation differ from case to case, they should be carefully verified using the data-NXB residual distribution plots.

8.6 Data Analysis Procedure

HXD data are accumulated on event by event basis. After on-board data selection, event data are further screened by the ground pipeline analysis process. By referring to the trigger and flag information (including the inter-unit anti-coincidence hit patterns), the pipeline assigns specific grades to the HXD events such as pure PIN events and pure GSO events. Detector responses and background files that match the particular (i.e., default) grade of events are provided by the HXD team. There are no user-specified parameters for the HXD.

8.7 Wide-Band All-Sky Monitor (WAM)

Tight active shielding of HXD results in a large array of guard counters surrounding the main detector parts. These anti-coincidence counters, made of ~ 4 cm thick BGO crystals, have a large effective area for sub-MeV to MeV gamma-rays. With limited angular ($\sim 5^\circ$) and energy ($\sim 30\%$ at 662 keV) resolution, they work as a Wide-band All-sky Monitor (WAM).

Analog signals from normally four counters on each side of an HXD sensor are summed up and a pulse height histogram is recorded every second. If a transient event such as a Gamma-Ray Burst (GRB) is detected, light curves with finer (31.25 ms) time resolution are also recorded in four energy bands. The energy coverage of the WAM extends from ~ 50 keV to ~ 5 MeV, and its effective area is ~ 800 cm² at 100 keV and 400 cm² at 1 MeV. These data are shared among the PI and the HXD team, i.e., the PI can use the full WAM data set. Since such transient events, especially GRBs, require immediate distribution to the community, the HXD team will make the analysis products, such as light curves and spectra, public as soon as possible at:

<http://www.astro.isas.jaxa.jp/suzaku/HXD-WAM/WAM-GRB>.

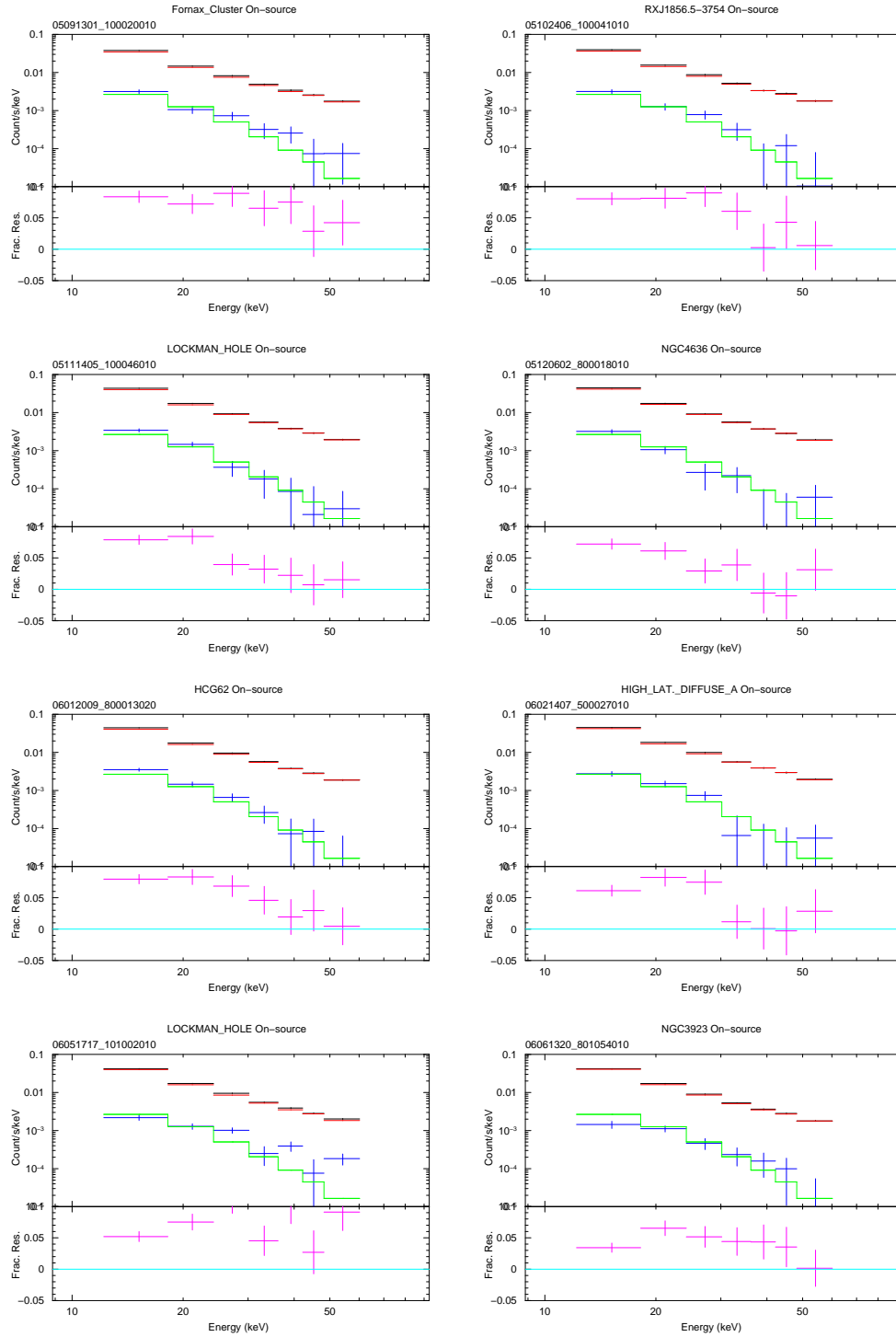


Figure 8.9: Comparison between the measured PIN spectra (black) and the PIN NXB model spectra (red) for observations of objects with no strong hard X-ray contribution. Their fractional residuals are given by purple crosses in the bottom panel of each figure. The blue and green histograms in the top panel indicate the background-subtracted spectrum and the typical CXB spectrum (Boldt 1987), respectively.

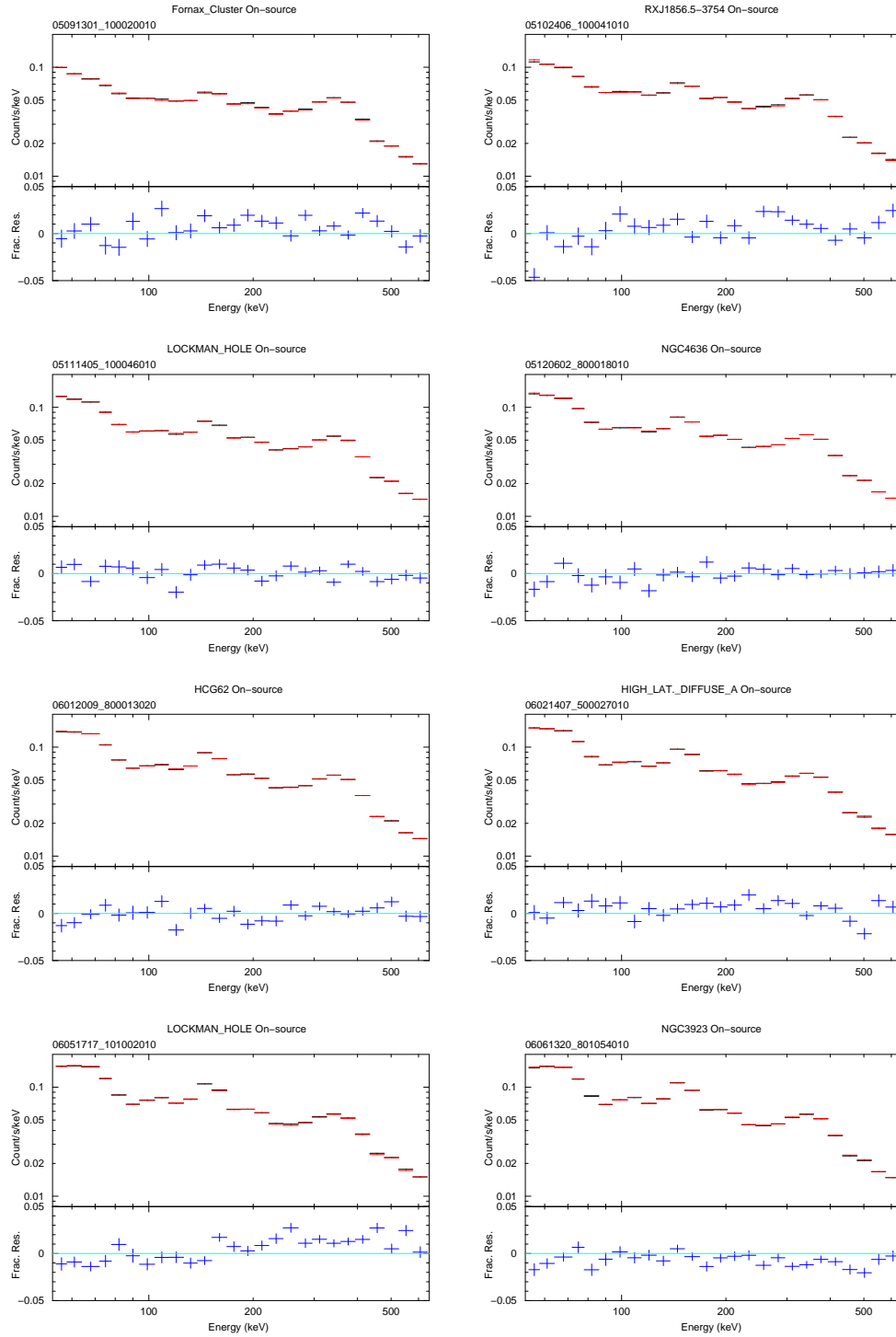


Figure 8.10: Comparison of the GSO spectra between the data (black) and BGD model (red) for observations of objects with no known strong hard X-rays. Their fractional residuals are given by blue crosses.

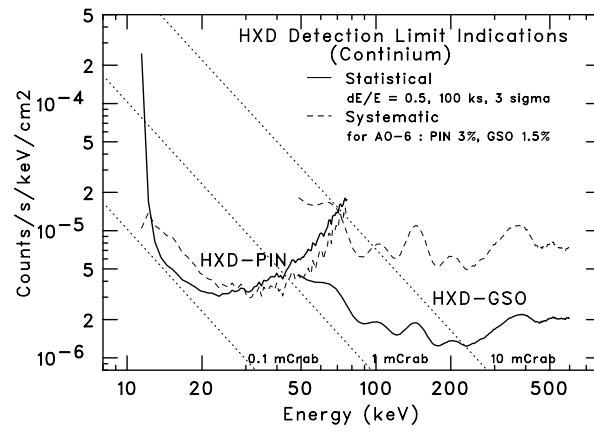


Figure 8.11: Calculated detection limits of the HXD, for continuum measurements. The solid lines denote the statistical 3σ limit for a 100ks exposure, while the dashed lines show the assumed systematic uncertainties of 3% and 1.5% for the PIN- and GSO-NXB modeling, respectively.

Appendix A

Acronyms

The following table lists acronyms used in this document.

Acronym	Definition
AAVSO	American Association of Variable Stars Observers
AE	Analog Electronics
AO	Announcement of Opportunity
AGN	Active Galactic Nuclei
ARF	Ancillary Response File
ARK	Astrophysics Research Knowledgebase
ASCA	Advanced Satellite for Cosmology and Astrophysics
ASM	All-Sky Monitor (on <i>RXTE</i>)
BGD	Background
BGO	Bismuth Germanate
BI	Back-Illuminated
CALDB	Calibration Database
CCD	Charge-Coupled Device
CI	Charge Ingestion
Co-I	Co-investigator
CPU	Central Processing Unit
CTE	Charge Transfer Efficiency
CTI	Charge Transfer Inefficiency
CXB	Cosmic X-ray Background
DDT	Director Discretionary Time
DE	Digital Electronics
Dec	Declination
DP	Data Processor
DSN	Deep Space Network
EA	Effective Area
EEF	Encircled Energy Function
EOB	Extensible Optical Bench
EPIC	European Photon Imaging Camera (on <i>XMM-Newton</i>)
ESA	European Space Agency
FI	Front-Illuminated
FWHM	Full-Width Half-Maximum
FITS	Flexible Image Transport System
FOV	Field Of View
FSA	Frame Store Area
FTOOLS	FITS Tools

Acronym	Definition
GO	Guest Observer
GOF	Guest Observer Facility
GRB	Gamma-Ray Burst
GSFC	Goddard Space Flight Center
GSO	Gadolinium Silicate
HEASARC	High Energy Astrophysics Science Archive Research Center
HESS	High Energy Stereoscopic System
HETG	High Energy Transmission Grating (on <i>Chandra</i>)
HEXTE	High Energy X-ray Timing Experiment (on <i>RXTE</i>)
HPD	Half-Power Diameter
HRI	High Resolution Imager (on <i>ROSAT</i>)
HV	High Voltage
HXD	Hard X-Ray Detector
ISAS	Institute of Space and Astronautical Science
INTEGRAL	INTErnational Gamma-Ray Astrophysics Laboratory
JAXA	Japan Aerospace Exploration Agency
LETG	Low Energy Transmission Grating (on <i>Chandra</i>)
LSI	Large Scale Integration
MIT	Massachusetts Institute of Technology
MPU	Main Processing Unit
NRA	NASA Research Announcement
NASA	National Aeronautics and Space Administration
NOI	Notice Of Intent
NSPIRES	NASA Solicitation and Proposal Integrated Review and Evaluation System
NXB	Non-X-ray Background
OBF	Optical Blocking Filter
PDS	Phoswich Detector System (on <i>Beppo-SAX</i>)
PH	Pulse Height
PIN	Positive Intrinsic Negative
PI	Principal Investigator
PI	Pulse Invariant
PIMMS	Portable Interactive Multi-Mission Simulator
PM	Photo-Multiplier
PPU	Pixel Processing Unit
PSF	Point Spread Function
PSPC	Position-Sensitive Proportional Counter (on <i>ROSAT</i>)
P-Sum	Parallel-Sum
QDE	Quantum Detection Efficiency
RA	Right Ascension
RAM	Random Access Memory
RDD	Residual Dark-current Distribution
RGS	Reflection Grating Spectrometer (on <i>XMM-Newton</i>)
RFA	Research Focus Area
RMF	Redistribution Matrix File
ROSAT	RÖntgen SATellite
RPS	Remote Proposal Submission
RXTE	Rossi X-ray Timing Explorer
SAA	South Atlantic Anomaly

Acronym	Definition
SAX	Satellite per Astronomia X
S/C	Spacecraft
SGR	Soft Gamma-ray Repeater
SLAC	Stanford Linear Accelerator Center
SMC	Small Magellanic Cloud
SN	SuperNova
SWG	Science Working Group
TBD	To Be Determined
TCE	TEC Control Electronics
TCU	Thermal Control Unit
TEC	Thermo-Electric Cooler
TOO	Target Of Opportunity
US	United States
USC	Uchinoura Space Center
UV	Ultra Violet
VHS	Very High State
VSNET	Variable Star NETwork
WAM	Wide-band All-sky Monitor
XIS	X-Ray Imaging Spectrometer
XRB	X-ray Binary
XRS	X-Ray Spectrometer
XRT	X-Ray Telescope
XRT-I	X-Ray Telescope for one of the four XIS detectors

Appendix B

Important Web/E-Mail Addresses

Primary *Suzaku* Sites

Japan: <http://www.astro.isas.jaxa.jp/suzaku/>

US : <http://suzaku.gsfc.nasa.gov/>

ESA: <http://www.rssd.esa.int/suzaku>

Suzaku GOF:

<http://suzaku.gsfc.nasa.gov/>

The “Proposal & Tools” button is of particular note.

Tools:

Viewing	http://heasarc.gsfc.nasa.gov/Tools/Viewing.html
PIMMS	http://heasarc.gsfc.nasa.gov/docs/software/tools/pimms.html
MAKI	http://heasarc.gsfc.nasa.gov/Tools/maki/maki.html
XSPEC	http://heasarc.gsfc.nasa.gov/docs/xanadu/xspec/index.html
WebPIMMS	http://heasarc.gsfc.nasa.gov/Tools/w3pimms.html
WebSPEC	http://heasarc.gsfc.nasa.gov/webspec/webspec.html

Questions:

The US GOF can be reached using the web form available at the bottom of every page within the *Suzaku* GOF site.

Technical Description

Japan: <http://www.astro.isas.jaxa.jp/suzaku/research/proposal/ao4/>

US: http://suzaku.gsfc.nasa.gov/docs/suzaku/prop_tools/suzaku_td/

ESA: <http://www.rssd.esa.int/index.php?project=ASTROE2&page=A0Docs>

US (ftp): ftp://legacy.gsfc.nasa.gov/suzaku/nra_info/suzaku_td.ps.gz

RPS (for Japanese proposals)

<http://rps.astro.isas.jaxa.jp/cgi-bin/RPS/SUZAKU/RPS.pl>

RPS (for US proposals)

<http://heasarc.gsfc.nasa.gov/ark/suzaku/>

RPS (for ESA proposals)

<http://www.rssd.esa.int/RPS/SUZAKU/RPS.pl>

(Or email rps@rssd.esa.int)